Development of a New RF Accelerating Cavity Loaded with Magnetic Alloy Cores Cooled by a Chemically Inert Liquid for Stabilizing and Enhancing the Performance of J-PARC Ring Accelerator

Yuichi Morita
Department of Physics, Graduate School of Science
The University of Tokyo

Abstract

J-PARC (Japan Proton Accelerator Research Complex) is a proton accelerator constructed in Tokai-mura, Ibaraki, Japan. J-PARC was designed to produce the world's most intensive proton beam and provide it to advanced research facilities for the wide range of field. T2K (from Tokai to Kamioka) is one of the most important experiment. It is a long baseline neutrino experiment. It requires 5×10^{21}POT in approximately 5 years which corresponds to 0.75[MW]. To produce proton beam of this intensity, the repetition rate of the accelerator is planed to be increased. This method requires the accelerating gradient to be enhanced, so that the accelerating cavity will be put in the hard environment to accelerate a large beam current in a long term. A powerful and stable accelerating cavity is indispensable. The presently installed cavities are loaded with cores made of "FINEMET". FINEMET is a magnetic alloy which is produced by Hitachi Metals, Ltd.. A stable operation of the presently installed cavities in Rapid-Cycling Synchrotron (RCS) has not established yet, because they have a problem that the FINEMET cores are damaged while the cavities are in operation. We are developing a new accelerating cavity which can realize the stable and powerful operation. We simulated the thermal stress in the core, and performed a test of compressing samples of the core. The cause of the damage was identified as a buckling which was caused by the thermal stress in the core. We showed the core without impregnation is favorable to prevent the buckling. The development of the new cavity is based on these results. The cores for the new cavity have unique structures. They are not impregnated and each core is radially separated into three. Fluorinert is used as the coolant. Fluorinert is a chemically inert liquid, so that it is suited for cooling FINEMET cores which is subject to corrosion. Fluorinert flows in the flow channel which is formed on the surfaces of the radially separated cores. The flow channel makes Fluorinert turbulent, so that a high cooling efficiency is realized. We designed RF structure of the cavity and the flow channel with FEM (Finite Element Method) simulators. We assembled a prototype of the new cavity, and prepared the test facility. This is the first case to use three dimensional FEM simulators for developing a cavity loaded with magnetic alloy cores. We measured the resonance frequency, the shunt impedance and the Q factor of the prototype cavity and verified they satisfied the requirements of RCS. The temperature on the surface of the small core was measured with the thermo paint. The value was consistent to that was obtained from the simulation. The effective heat transfer coefficient was obtained by measuring the time constant of the temperature decrement of Fluorinert, and the value was consistent to that was obtained from the simulation in 20% . The heat transfer coefficient on the surface of the small core was obtained with the simulation. The value is consistent to that was calculated with the empirical equation. The value surpassed that of presently installed cavity over 60[L/min]. We supplied the power to the prototype cavity up to 10[kW], and it worked stably. This is the first development of the cavity loaded with magnetic alloy cores, which is able to be operated stably with the large input power of 10[kW] per core. Adopting this new cavity is the most realistic way to stabilize and enhance the performance of the J-PARC ring accelerators.

Contents

Chapter 1

Introduction

When a proton collides to a target, a variety of secondary particles such as kaon, pion, neutron, antiproton are produced. Secondary particles are useful for material and life sciences, and the characteristics of themselves are also investigated. To activate advanced researches using secondary particles, the world's most intensive proton beam accelerator facility was built at Tokai-mura, Ibaraki, Japan. The accelerator named J-PARC (Japan Proton Accelerator Research Complex) was built as a joint project between KEK and JAEA. Many kinds of research field, such as, nuclear and particle physics, materials science, life science are carried out there.

1.1 Physics goals and requirements to the accelerator system

On behalf of the experiments, T2K (from Tokai to Kamioka) is introduced in this section. T2K is a long baseline neutrino oscillation experiment. ν_μ which is generated at J-PARC flies to the detector (Kamiokande) in Kamioka, Gifu. The main goal of T2K is the discovery of $\nu_\mu \to \nu_e$ oscillation. This oscillation is the unique mode which has not discovered yet, and is expected to show the notice for CP violation measurements which will be performed in the future. The relation between integrated beam power and $\sin^2 2\theta_{13}$ is shown in Figure **1.1**. $\nu_\mu \to \nu_e$ oscillation is expected to be discovered when $\sin^2 2\theta_{13}$ is larger than 0.018[1]. This condition corresponds to over 3750[kW$\times 10^7$s]. It takes five years to reach this value if the beam power is 0.75[MW] and the accelerator is operated for 10^7 seconds per year. Therefore, the enhancement of beam is crucial.

1.2 Research background arises from the aspect of the accelerating cavity

J-PARC accelerator has been designed to provide the world's most intensive proton beam. Main components are listed below.

- Ion source

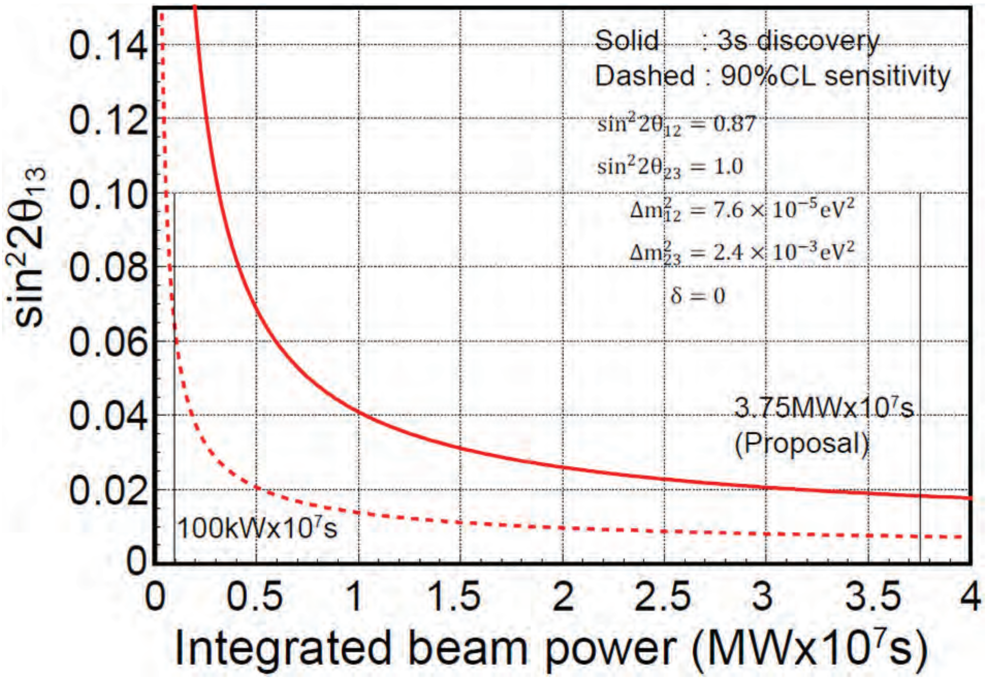

Figure 1.1: The relation between integrated beam power and $\sin^2 2\theta_{13}$[1]

- Linac
- RCS (Rapid-Cycling Synchrotron)
- MR (Main Ring)

The ion source produces negative hydrogens. The linac is a linear accelerator which accelerates negative hydrogen beam up to 181 MeV. RCS is a ring accelerator which accelerates a proton beam up to 3 GeV. MR is a ring accelerator which accelerates the proton beam up to 30 GeV. A bird's view of the J-PARC accelerator is shown in Figure **1.2**.

The two rings are constructed for the experiments which needs a few GeV range beam and those needs a few tens GeV range beam. The total length of Linac is approximately 330 m, the circumference of RCS and MR are approximately 350 m, 1.6 km respectively. The accelerator is at 15 m underground.

J-PARC is able to produce better results than other accelerator facilities, because of its unprecedented intensity of proton beam. The high beam energy and the large beam current provide high production efficiency of secondary particles. Research projects require that J-PARC accelerator supplies beam of kW order in both regions of GeV energy and a tens of GeV energy. The synchrotrons of J-PARC is consisted with two rings.

We developed a new type of an accelerating cavity for RCS. The development of this cavity is introduced in this thesis. The background of the development is shown below.

- Accelerating cavities which are installed in both synchrotrons are loaded with FINEMET cores. As mentioned in the latter section, FINEMET is a metallic alloy whose satu-

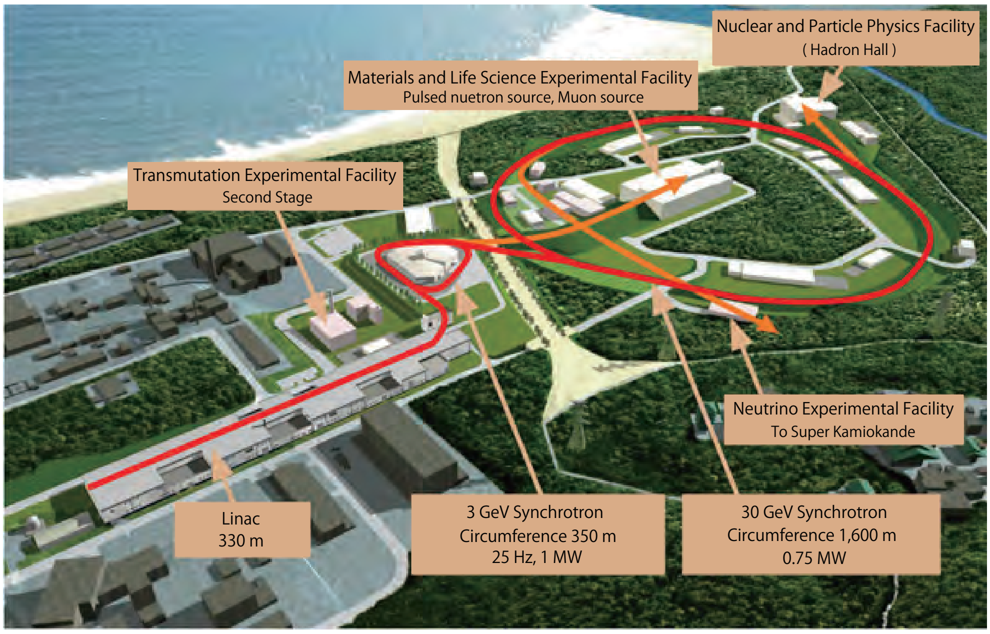

Figure 1.2: A bird's view of the J-PARC accelerator[2]

ration magnetic-flux-density and Curie temperature are enough high, and this characteristic supports the high accelerating gradient with a high input power. However, presently installed RCS accelerating cavities have not been operated stably, because of the decrements of their impedances caused by damages on the cores.

- FINEMET is a Fe-based material, so that it is subject to corrosion. They are water proofed to avoid touching water which is used as the coolant. However, the corrosion is still concerned for long term operation. This concern is common in both RCS and MR.

For the first issue, we simulated the thermal stress in the RCS core and compressed samples of the core. Comparing the results of the simulation and the compression test, we identified the damage as a buckling caused by the thermal stress in the core. Details are shown in the next chapter.

For the second issue, Fluorinert is selected as a coolant for the new cavity. Fluorinert is a liquid which is chemically inert, so that no corrosion is expected.

We developed a prototype cavity. The core for this cavity is not impregnated with epoxy resin to avoid the buckling, and is radially separated into three. These treatments help the core not to be damaged by the thermal stress. Fluorinert flows in the flow channel which is formed on the surface of the core, and is expected to be turbulent. Details are given in Chapter 4.

1.3 Outline of the thesis

In chapter 2, details of the J-PARC accelerators are introduced. In chapter 3, the study for identifying the cause of the buckling on the cores is shown. Chapter 4 describes the development of the new RF accelerating cavity loaded with FINEMET cores cooled by Fluorinert. The results of the RF test of the prototype cavity are shown in Chapter 5. Chapter 6 is the summary of performance of the prototype cavity and shows Discussion. Finally, the thesis is concluded in Chapter 7.

Chapter 2

Accelerator complex at J-PARC

This chapter introduces the accelerators in J-PARC. The layout of the accelerator complex is shown in Figure **2.1**. It is consisted with three accelerators.

- 181 MeV Linac
- 3 GeV Rapid-Cycling Synchrotron (RCS)
- 30 GeV synchrotron (MR)

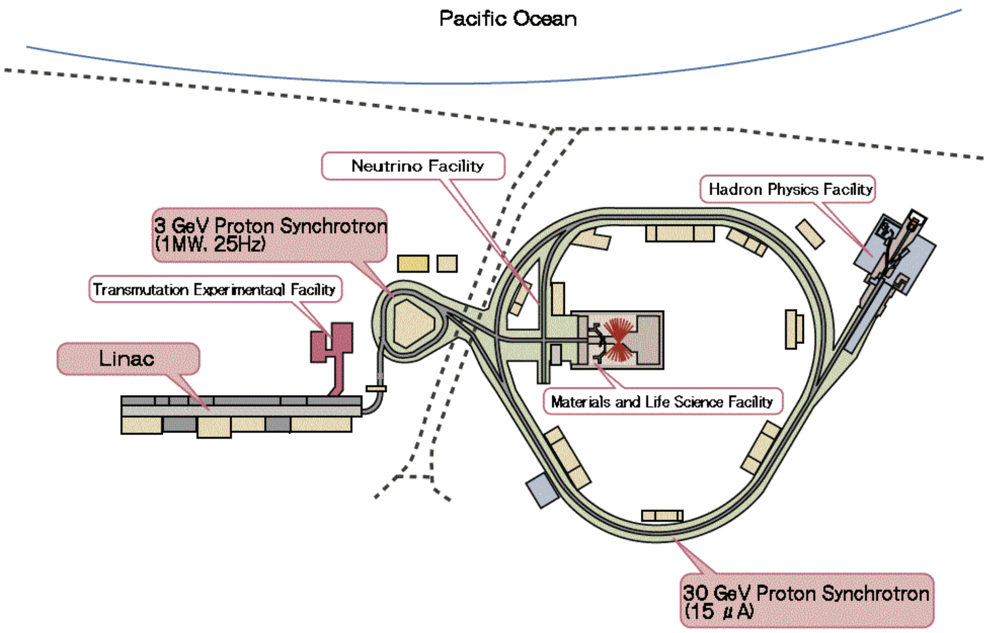

Figure 2.1: Layout of the accelerator complex[2]

2.1 Ion source

Particles generated at the ion source at J-PARC are negative hydrogens (H^-). They travel in Linac, then two electrons are stripped at the injection to RCS and become proton beams. The use of negative hydrogens stands on following reasons.

The harmonic number of RCS is two, which means two bunches are accelerated at the same time. We should compose two bunches in RCS by superposing intermediate bunches which are injected from Linac to RCS one after another. The schematic view of the injection is shown in Figure **2.2**.

Electromagnets bend the orbits of intermediate bunches at the injection, and the injected bunches and circulating bunches are superposed. If the injected bunch is a negative hydrogen, bending directions of an injected bunch and a circulating bunch are opposite and the beams can be superposed as shown in left-hand-side of Figure **2.2**. If the injected bunch is a proton, the bending direction of the injected bunch is same as that of the circulating bunch and they cannot be superposed as shown in right-hand-side of Figure **2.2**[13].

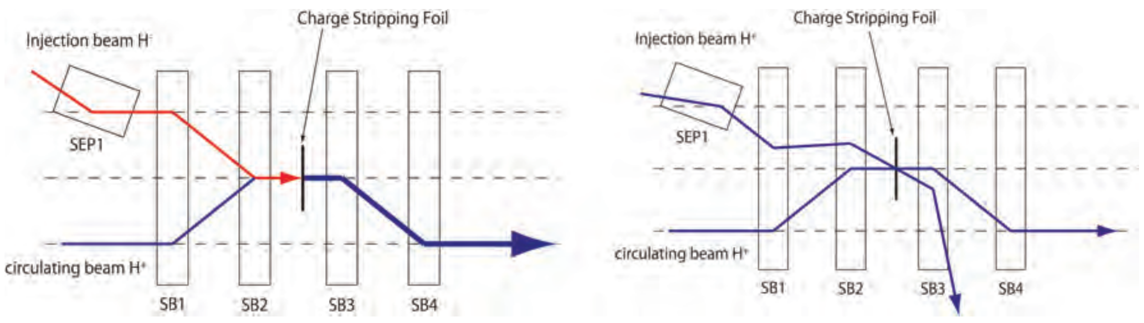

Figure 2.2: (left) Negative hydrogens are injected. Magnets SB1 and SB2 bends the injecting and circulating beams to opposite directions, so that they are able to be superposed. (right) Protons are injected. The injecting and circulating beams are not able to be superposed.

The structure and parameters of the ion source are shown in Figure **2.3** and Table **2.1** respectively. The structure inside plasma chamber is the cylinder whose inside diameter is 100 mm and inside length is 130 mm. A filament made of LaB_6 is installed at the center of the top flange, which generates a source plasma with arc discharges[14]. Equations of generation and extinction reactions of hydrogens are shown below.

Generation: there are two steps for reactions. ν, ν' are excited states of molecules[15].

$$H_2(\nu) + e(\text{high velocity}) \rightarrow H_2(\nu') + e(\nu < \nu') \tag{2.1}$$

$$H_2(\nu') + e(\text{low velocity}) \rightarrow H^- + H^0 \tag{2.2}$$

Extinction: there are three reactions.

$$e + H^- \rightarrow e + H^0 + e \tag{2.3}$$

$$H^+ + H^- \rightarrow H^0 + H^0 \tag{2.4}$$

$$H^0 + H^- \rightarrow e + 2H^0 \ or \ H_2 \tag{2.5}$$

As shown in Figure **2.4**, the extinction reaction is active in higher electron temperature.

To suppress the extinction reaction, magnetic field of permanent magnet is applied. The field prevents high temperature electrons from entering the down stream of the plasma generation room (close to the beam extraction system). It is called a "magnetic filter". The beam extraction system is composed with plasma electrodes (PE), extraction electrode (EXE), and ground electrodes (GE). Voltages of about 10 kV and 40 kV are applied between PE and EXE (extraction voltage), EXE and GE (accelerating voltage), respectively. Therefore, the extracted negative ion beam has 50 keV[14].

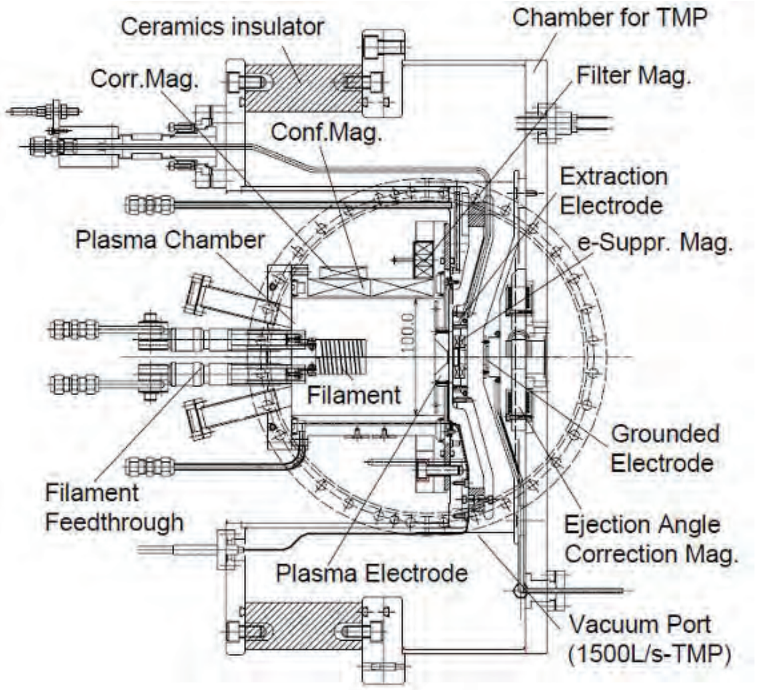

Figure 2.3: A schematic view of the ion source[14]

Table 2.1: Parameters of the ion source[14]

Parameter	Value
Beam Energy	50 keV
Beam Current	$\sim$ 32 mA
Beam Pulse Length / Repetition	100μs / $\leq$25 Hz
Arc Pulse Length / Repetition Rate	350μs / 25 Hz
Filament Voltage / Current	10.2 V / 120 A
Arc Voltage / Current	146 V / 326 A
Arc Power	48 kW
H_2 gas flow rate	17.9 SCCM

*SCCM, Standard Cubic Centimeters per Minute

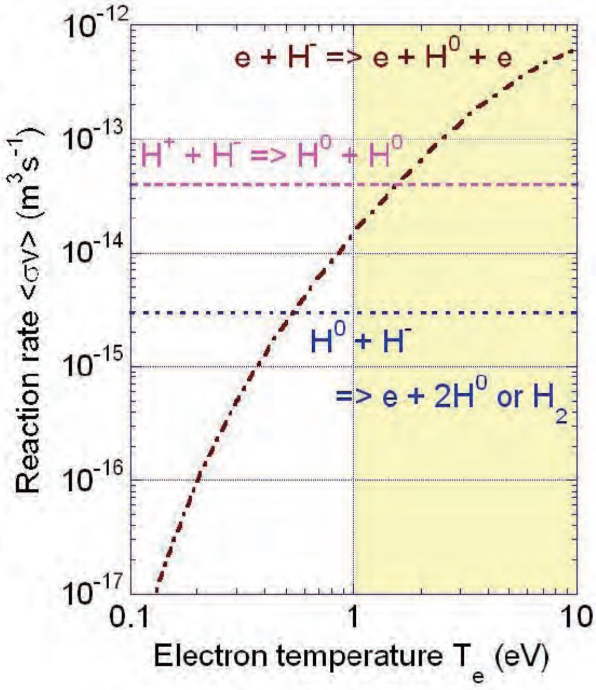

Figure 2.4: Reaction rates of extinction reactions against an electron temperature[15]

2.2 Linac

Linac which is at the first acceleration region is composed with four accelerating part to follow the gradual increase of the velocity of the proton beam. An overall view of Linac is shown in Figure **2.5**. RFQ (Radio-Frequency Quadrupole linac), DTL (Drift Tube Linac), SDTL (Separate-type Drift Tube Linac), ACS (Annular Coupled Structure Linac) are installed in the order of beam's passage. The present output energy of the linac is 181 MeV, which is planed to be upgraded to 400 MeV.

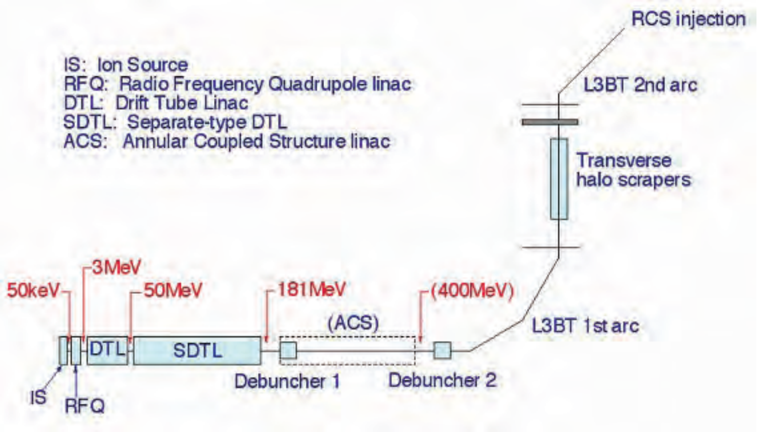

Figure 2.5: An overall view of Linac[16]

RFQ (Radio-Frequency Quadrupole linac)[19]

DTL is often used to accelerate low energy beams, however it is difficult to install it just behind of the ion source. The energy of a beam extracted from the ion source is 50 keV. It corresponds to $\beta = 0.01$. Typical frequency of Alvarez type DTL is 200 Hz. It is equivalent to $\lambda = 150$ cm. As mentioned at the following paragraph for DTL, quadrupole magnets are installed between drift tubes in DTL in order to focus beams. Each length of quadrupole magnet must be less than $\beta\lambda = 1.5$ cm. Fabricating such short Q-magnets is impossible. Some solutions are considerable, for example, to enhance the accelerating voltage of the ion source or to lengthen DTL. The most realistic solution is to introduce RFQ. Structures of RFQ are shown in Figure **2.6** and Figure **2.7**. Parameters of RFQ are shown in Table **2.2**. Four electrodes surrounds a beam. They are two positive electrodes and two negative electrodes which are positioned as alternately. AC electric field of quadruple type appears among electrodes. It focuses beams in the similar manner of Q-magnet. Each electrodes wave along beam axis in the cycle of $\beta\lambda/2$. This waving structure accelerates beams along the beam direction. The length of a cell ($\beta\lambda/2$) is possible to be a few mm, and the installation just behind of the ion source becomes feasible. Another characteristic of RFQ is bunching. DC beam is allowed to be used as an injection beam, because RFQ is able to accelerate and focus a beam over bunching. The output energy of RFQ is 3 MeV.

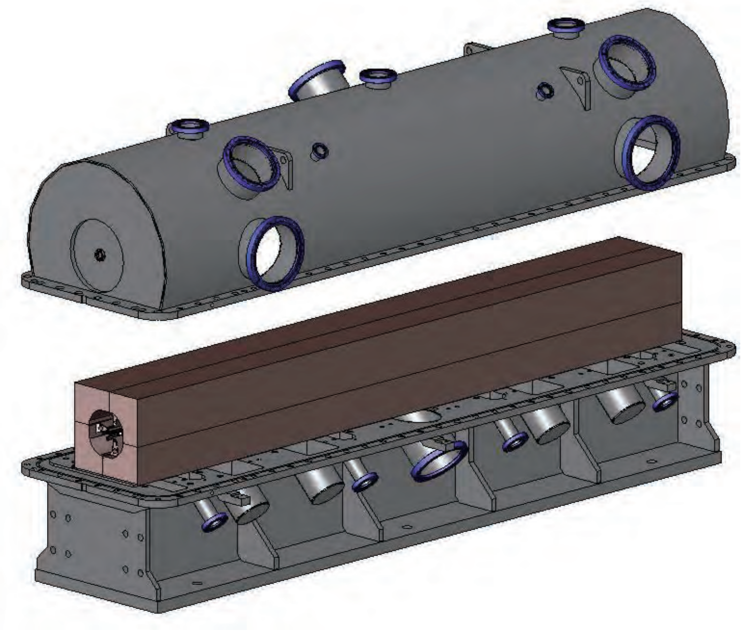

Figure 2.6: A structure of RFQ[18]

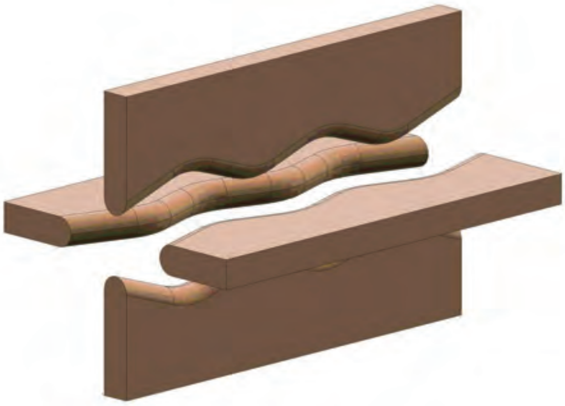

Figure 2.7: A schematic view of the electrodes of RFQ

RF chopper[20]

To decrease the beam loss at the injection, the beam is chopped in the same cycle of the injection to RCS. Three RF choppers are installed at MEBT (Medium Energy Beam Transport) which is between RFQ and DTL. 46% of micro bunches are removed by the RF choppers. Then, an intermediate bunch structure of 500 μs is produced. As shown in Figure **2.8**, this intermediate bunch structure is suitable for forming two bunches at the injection of RCS. The length of MEBT should be short in order to prevent increment

Table 2.2: Parameters of RFQ[19]

Parameter	Value
Length	3.944 m
Input Energy	0.05 MeV
Output Energy	3 MeV
Peak Input Beam Current	53 mA
Peak Output Beam Current	50 mA
Transmission	94 %
Operation Frequency	324 MHz

of beam emittance which is caused by the space-charge-effect when the beam energy is low. Therefore, the RF choppers should be not only compact but also have high bending electric field. This requirement is satisfied by utilizing RF cavity which has low loaded Q. 324-MHz RF deflector (RFD) is adopted as the chopper. The configuration of RFD is shown in Figure **2.9**. TE_{11}-like mode is excited in RFD by two electrodes. Electric field oscillating 324 MHz is generated. Beams are kicked to a beam dump at down stream.

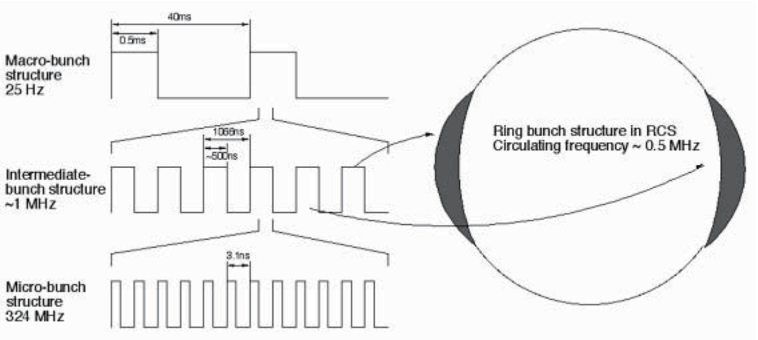

Figure 2.8: A scheme for forming bunches[16]

DTL (Drift Tube Linac)[17]

The function of DTL is to accelerate beams from 3 MeV to 50 MeV after RFQ. Alvalez type DTL used in J-PARC has a structure shown in Figure **2.10**. The configuration of electromagnetic field on resonance is shown in Figure **2.10**. Accelerating electric field is seen between tubes. The resonance frequency is 324 MHz. The length of tubes are short at upstream and long at downstream because the velocity of beam gradually increases in DTL. Electromagnets are installed at spaces between the tubes and focus the beam. The installation of these electromagnets are favorable for accelerating low β beam because low β beam has strong space charge effect and is easy to expand.

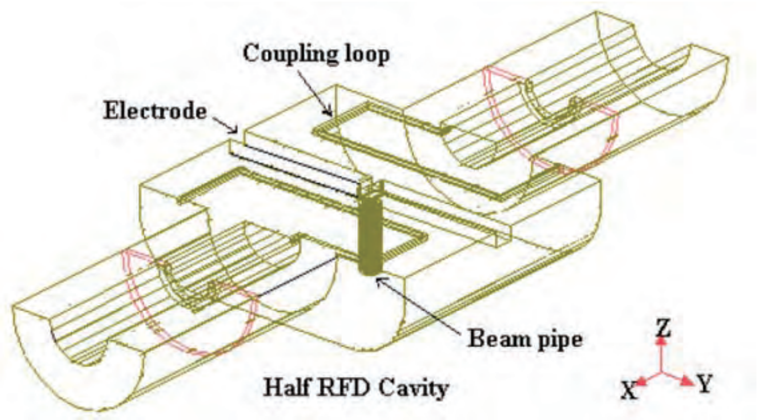

Figure 2.9: A cross-section of RFD[20]

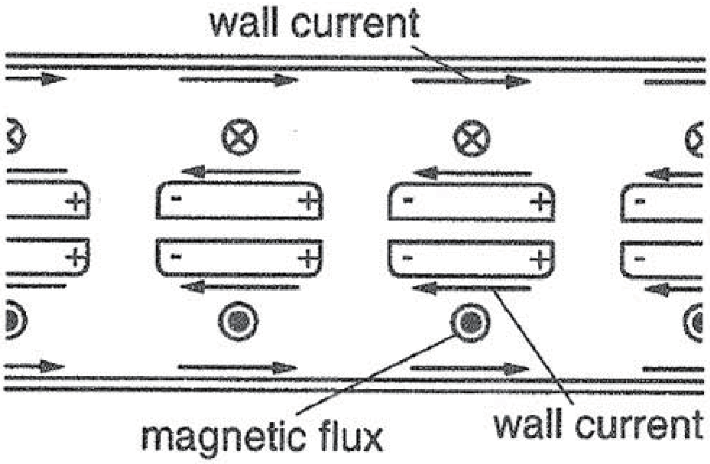

Figure 2.10: A cross-section of DTL[17]

Table 2.3: Parameters of DTL[17]

Parameter	Value
Length	27.12 [m]
Structure length	26.68 [m]
Input energy	3 [MeV]
Output energy	50 [MeV]
Operation frequency	324 [MHz]
Number of DTL tanks	3
Number of cells	146

SDTL (Separate-type Drift Tube Linac)[17]

SDTL is used to accelerate beams from 50 MeV to 181 MeV in the first stage and to 191 MeV in the second stage. Its structure is shown in Figure **2.11**. It is similar to the structure of DTL. The resonance frequency is 324 MHz. Differences are that electromagnets are outside of cavity and the length of every tube is same. It is not necessary to install electromagnets in short intervals because the space charge effect is weak in this energy range. If we take spaces to install magnets, acceleration in a high frequency becomes difficult, instead. Parameters of SDTL are shown in Table **2.4**.

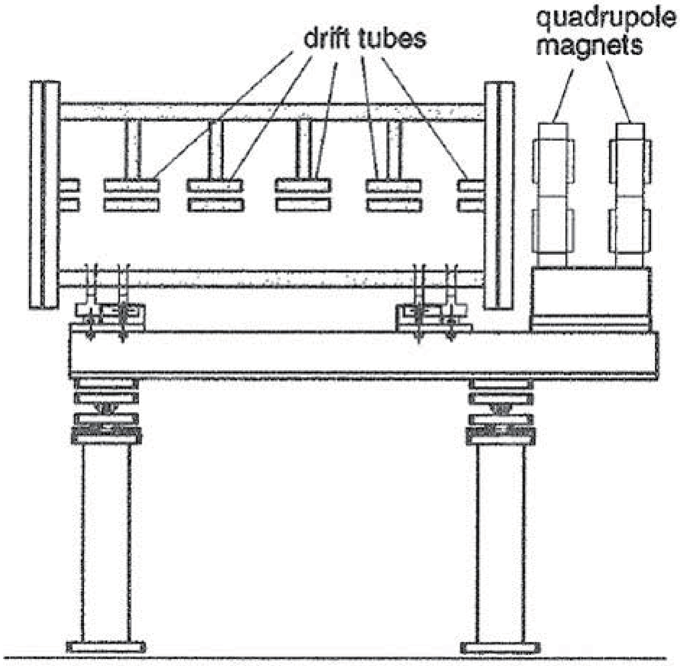

Figure 2.11: A cross-section of SDTL[17]

ACS (Annular Coupled Structure Linac)[17]

ACS accelerates proton beams from 191 MeV to 400 MeV after SDTL. The structure of ACS is shown in Figure **2.12**. It is not utilized in the first stage, but in the second stage. The structure is complicated at a glance. The principle of the acceleration is based on a multi-cell cavity. The eigenvalues of electromagnetic field in a multi-cell cavity are 0 mode, $\pi/2$ mode, π mode, ... in acending order. If a perturbation is applied on the cavity, i.e. the flatness of the cavity is bad, the lowest mode whose detune from the resonance frequency is the least is $\pi/2$ mode. That means $\pi/2$ mode is the most suitable for the stable operation. However, as shown in Figure **2.13**, cells without electric fields appear every other cell in $\pi/2$ mode. To remove these cells and improve accelerating efficiency, ACS shown in Figure **2.14** was developed. The cells without electric fields are excluded

Table 2.4: Parameters of SDTL[17]

Parameter	Value
Length	91.2 [m]
Structure length	65.69 [m]
Input energy	50.1 [MeV]
Output energy	first stage: 181 [MeV] second stage: 190.8 [MeV]
Operation frequency	324 [MHz]
Number of DTL modules	16
Number of quadrupoles	62

to the sides and every accelerating cavities is next to each other. Parameters of ACS are shown in Table **2.5**.

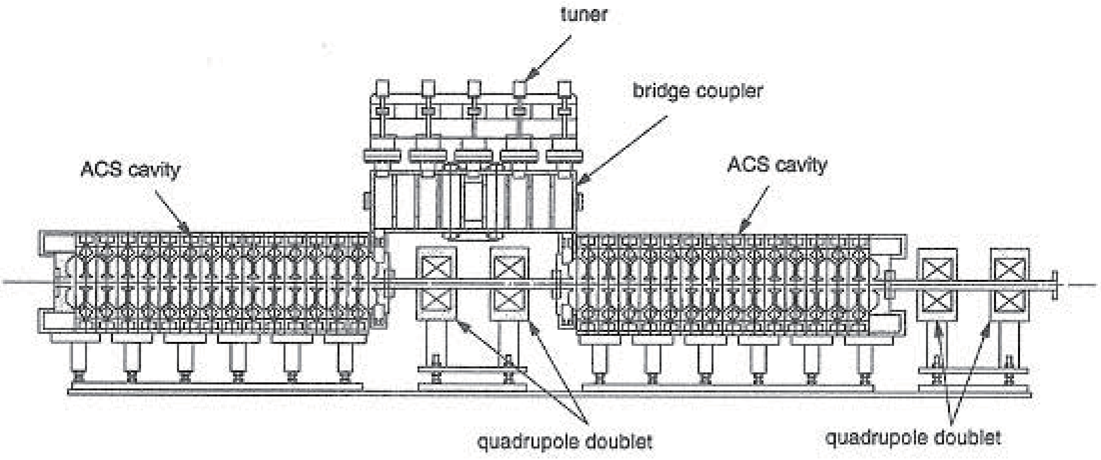

Figure 2.12: A cross-section of ACS[17]

2.3 RCS

The ring accelerator which is down stream of the linac is RCS (Rapid-cycling Synchrotron). The circumference is approximately 350 m. It has three linear sections. Each linear section is specific for acceleration, injection, and extraction, respectively. Main parameters of RCS are shown in Table **2.7**. The purpose of RCS is to generate secondary particles which have energies of a few GeV. RCS accelerates proton beams from 181 MeV (in the first stage) to 3 GeV and provides them to Materials and Life Science Experimental Facility (MLF). The design goal of the beam power is 1 MW. RCS also has a function to provide beam to MR.

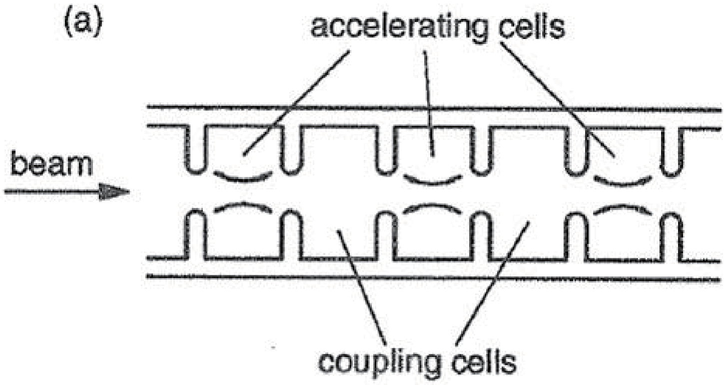

Figure 2.13: A $\pi/2$ mode of a multi-cell cavity[17]

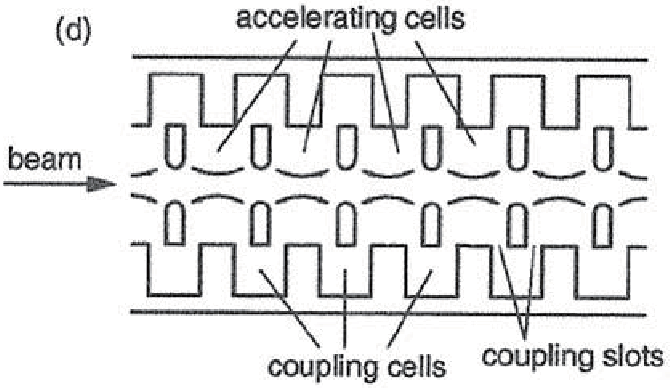

Figure 2.14: A schematic view of ACS[17]

In the first stage, proton beams from SDTL, which have intermediate-bunch-structure of 1 MHz, are injected to RCS. The beams circulate at 0.5 MHz in RCS which corresponds to the injection energy of 181 MeV. This frequency is equal to half of the injection frequency of the intermediate-bunch-structure. Odd bunches and even bunches in the intermediate-bunch-structure form one bunch in RCS, respectively. The harmonic number of RCS is two. As shown in Figure **2.8**, odd bunches enter in one bucket, even bunches enter in another bucket. These two bunches formed in RCS are accelerated to 3 GeV in 20 ms, and extracted to MR or MLF before next beams are injected from SDTL. The repetition rate of this process is 25 Hz. Two bunches formed in the process are called one cycle. Four cycles are extracted from RCS to MR, then 87 cycles are extracted to MLF. In this 87 cycle extraction, beam acceleration and extraction are completed in MR, and next four cycles are extracted to MR again. This process is repeated.

Table 2.5: Parameters of ACS[17]

Parameter	Value
Length	108.3 [m]
Input energy	190.8 [MeV]
Output energy	400 [MeV]
Operation frequency	972 [MHz]
Number of ACS modules	23
Number of quadrupoles	90

2.3.1 RF system

The RF system in RCS is mainly consisted with following components[68].

- RF power amplifier
- Anode power supply
- Accelerating cavity

Each RF power amplifier drives one accelerating cavity. The three gaps of each cavity are connected in parallel and directly driven by the amplifier. The output stage of the amplifier consists of two tetrodes operated in push-pull. One dc-power supply is employed for the two tetrodes. The detail of the accelerating cavity is given in the next subsection.

2.3.2 Accelerating cavity

Eleven accelerating cavities are installed in RCS. The cross-section of the RCS accelerating cavity is shown in Figure **2.16**. The cavity is $\lambda/4$-wave coaxial and is corresponds to type B which is shown in Appendix J. One cavity is consists with three accelerating cells. Each cell has one accelerating gap and two tanks are installed on both sides of each accelerating gap. Three magnetic alloy cores are installed in each tanks. Namely, six cores are installed in one accelerating cell. The Q value of the RCS cavity is $\sim$2. No automatic tuning system for the resonance frequency is necessary on the RF system. The cavity is suited for the operation with the second harmonics, because the low Q allows the second harmonics to exist. The range of the operating frequency is from 1.23[MHz] to 1.67[MHz]. The accelerating gradient per gap is 15[kV].

2.3.3 FINEMET cores

Amorphous

Most of materials such as metals, oxides, compounds are formed by crystals because atoms are aligned in order. However, there is another type of material which has random alignment of atoms. The material is called amorphous. Because of the randomness, we can regard amorphous as an isotropic material in macroscopic view. It does not have magnetic crystalline anisotropy, and no grain boundary which prevents domain wall from moving exists, so that amorphous possesses excellent properties as a soft magnetic material[26]. By making it as a ribbon, eddy current is reduced and is durable in RF field. An amorphous core of accelerating cavity in the synchrotron of National Institute of Radiological Science (NIRS), which is introduced in Appendix J, is fabricated by winding an amorphous ribbon of 1.5 μm thick applied with a silica insulation layer of 1.5 μm thick on one surface. A filling ratio of the core is approximately 75% .

FINEMET

A magnetic material called FINEMET was developed by Hitachi Metals, Ltd.. This is a magnetic alloy which has a high permeability, saturation magnetic-flux-density, and Curie temperature. These properties is suited for the RF cavity of the proton and ion synchrotrons. Typical properties of conventional ferrite and FINEMET (FT-3M) are shown in Table **2.6**.

In the production process of FINEMET, an amorphous ribbon which has 18 μm thickness and 35 mm width is painted with the silica on one surface. The amorphous consists of Fe, Si, B and small amounts of Cu and Nb. The ribbon is wound into a toroidal core. Then, it is annealed in a nitrogen atmosphere to increase magnetic properties by making crystals small in order of 10 nm. The amorphous core becomes to have an excellent magnetic properties and is called FINEMET core[69]. The magnetic alloy cores assembled in the RCS cavity are the FINEMET cores. The figure of the FINEMET core for RCS is shown in Figure **2.15**.

Table 2.6: Properties of FINEMET[69]

	FINEMET (FT-3M)	Ni-Zn ferrite
Relative permeability (1MHz)	2400	500
Saturation magnetic-flux-density [T]	1.2	0.4
Curie temperature [°C]	570	200
Thermal conductivity [W/m/K]	7.1	6

2.3.4 Power loss in the core and Cooling of the heat load

Most input powers to the cavities are dissipated in the cores. Water cooling is adopted to cool the heat load. Laminar water flows on the surfaces of the cores. The heat transfer coefficients from the surface of the core to laminar water is calculated as 500[W/m^2/K]. The calculation is shown in Appendix D.

The power loss in operation was evaluated by measuring the rise of water temperature. It was approximately 6 kW per core.

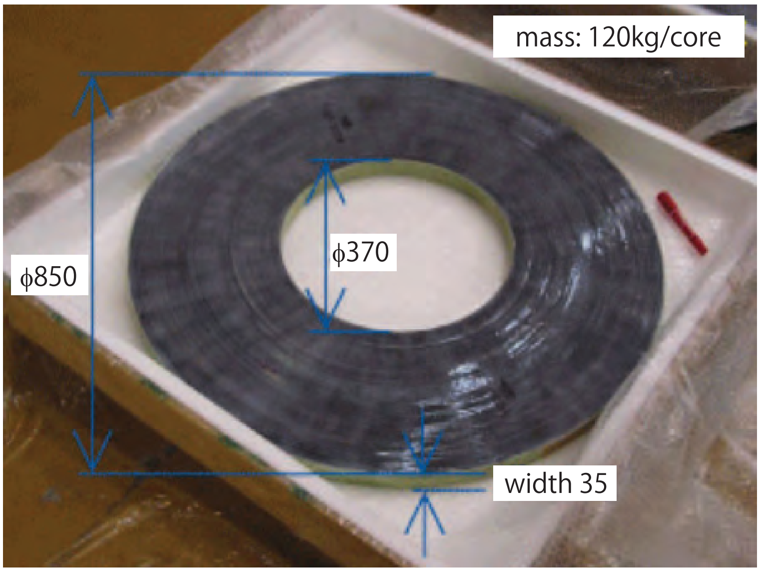

Figure 2.15: The figure of the FINEMET core for RCS[2]

2.3.5 Problems

The heat on the core causes a buckling and decrease the impedance of the core. Water has a good cooling efficiency, however, the magnetic alloy cores are corroded by water. The surface of the cores are coated not to touch with water. This coating strongly interrupts the heat radiation, which raises fatal bucklings. To stabilize and enhance the performance of RCS by solving the buckling problem, it is necessary to develop a new cavity which is able to release the thermal stress in the cores. The purpose of this paper is introducing the development. Details of the cavity is described in the next chapter.

2.4 MR

MR (Main Ring) is located after RCS. MR has three linear sections. Its purpose is to provide secondary particles whose energies are a few tens GeV. Each linear section has a function of injection, acceleration, and extraction, respectively. The main parameters of MR are shown in Table **2.8**. MR accelerates proton beams from 3 GeV to 30 GeV. The accelerated beams are used at the neutrino beam line and Hadron hall. The aiming beam power is 0.75 MW.

Four cycles consisted of eight bunches injected from RCS to MR. One bucket is empty because the harmonic number of MR is nine. This vacant bucket provides a time for the standing of a kicker for ”fast extraction”.

There are two beam lines for extractions in MR. One leads to Hadron Hall, the other leads to Neutrino experimental facility. Each method for extraction is called ”slow extraction” and ”fast extraction”, respectively.

In the slow extraction scheme, the proton beam accelerated up to 30 GeV is attracted

Table 2.7: Parameters of RCS[2]

Parameter		Value
Circumference		348.333 [m]
Average radius		55.44 [m]
Injection energy		0.181/0.4 [GeV]
Extraction energy		3.0 [GeV]
Particle per pulse		8.3×10^{13}
Revolution period		
	at Injection	1.629 [μs]
	at Extraction	1.196 [μs]
Repetition rate		25 [Hz]
Ramping pattern		Sinusoid
	Injection	$\sim$500 [μs]
	Acceleration	20 [ms]
	Decreasing Field	20 [ms]
Average current		333 [μA]
Circulating current		
	at Injection	8.2 [A]
	at Extraction	11.1 [A]

to the electro-static septum (ESS) by bump magnets as shown in Figure **2.17**. Then the beam size of horizontal direction is enlarged by means of the resonance of betatron oscillation at a resonance sextupole magnet. A thin septum electrodes are installed inside of the ring. When the beam scratches the septum electrodes, a part of the beam is scraped. The scraped part is kicked toward the inside of the ring by the electric field. As the scraped beam oscillates by betatron oscillation, it will close in on the original orbit. Then it will cross the original orbit and flies toward outside of the ring. The septum is at a point where the oscillation is maximum (the phase of betatron oscillation is 270° at the point). The septum lead the beams to a beam line connected to Hadron hall. Though Hadron hall is outside of the ring, the beam is kicked toward inside of the ring in order to take enough distance between ESS and the septum. This process is repeated and the beam is gradually scraped. Duration time for the slow extraction is approximately 0.7 sec[22].

The fast extraction is the method that circulating eight bunches which have been accelerated up to 30 GeV are extracted by one kick. They are extracted to the neutrino beam line which is located inside of MR. Duration time for the fast extraction is approximately 5 μs[23].

The cross-section of the accelerating cavity for MR is shown in Figure **2.18**. The structure is similar with that of RCS. The cavity is $\lambda/4$-wave coaxial and is corresponds to type B which is shown in Appendix J. One cavity is consists with three accelerating cells. Each cell has one accelerating gap and two tanks are installed on both sides of

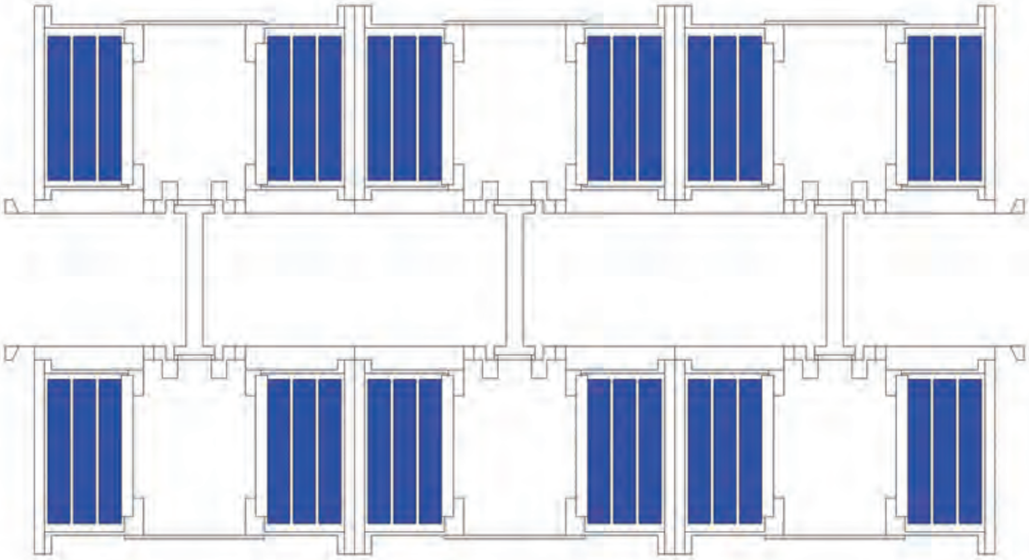

Figure 2.16: A cross-section of the accelerating cavity in RCS. The blue area represents the FINEMET cores.

each accelerating gap. Three magnetic alloy cores are installed in each tanks. Namely, six cores are installed in one accelerating cell. The difference is that MR cavity is loaded with cut cores while RCS cavity is loaded with non cut cores. Q value of the MR cavity is tuned to ∼25 by adjusting the cut width. Six accelerating cavities are installed in MR.

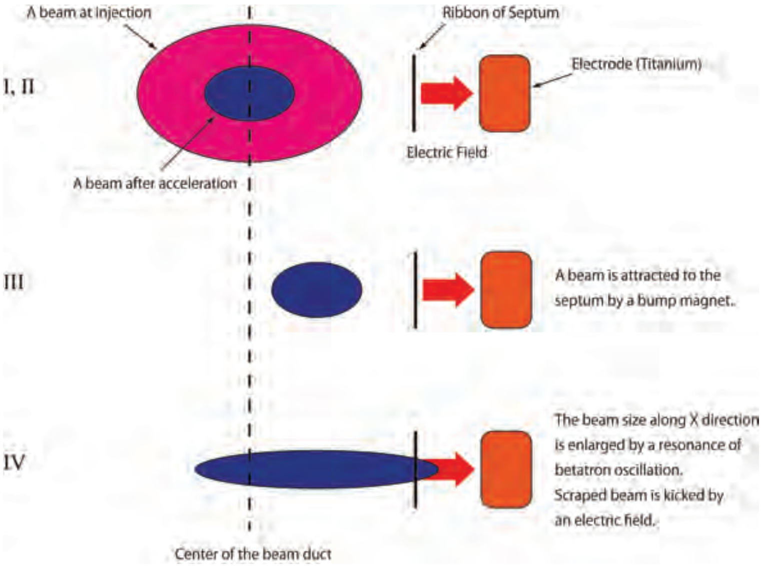

Figure 2.17: A scheme of the slow extraction[22]

Table 2.8: Parameters of MR[2]

Parameter		Value
Circumference		1567.5 [m]
Average radius		249.475 [m]
Injection energy		3 [GeV]
Extraction energy		30 [GeV]
Particle per pulse		3.3×10^{14}
Revolution period		
	at Injection	5.384 [μs]
	at Extraction	5.230 [μs]
Repetition rate		0.3 [Hz]
Ramping pattern		Parabola+Linear+Parabola
	Injection	0.17 [s]
	Acceleration	1.96 [s]
	Parabola	0.13 [s]
	Linear	1.7 [s]
	Parabola	0.13 [s]
Cycles for each repetition		4
Bunches per cycle		2

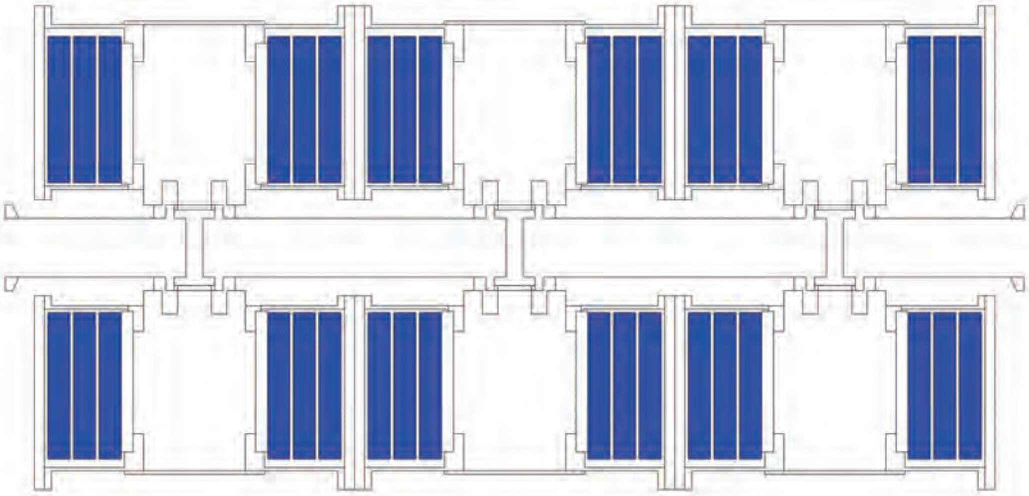

Figure 2.18: A cross-section of the MR cavity. The blue area represents the FINEMET cores.

Chapter 3

Numerical analysis and Experiment to identify the cause of the buckling on RCS cores

The cores in the presently installed cavity were damaged when the cavity was in operation. This chapter reports the study about the cause of the damage.

3.1 Background of the study

RCS is a synchrotron to accelerate proton beams from 181 MeV to 3 GeV and extract them. The accelerating cavity of RCS has a characteristic that it is loaded with FINEMET cores. A cavity loaded with ferrite cores is conventional for a proton and ion acceleration. FINEMET enabled twice higher accelerating gradient than ferrite. Sizes of cores in a presently installed RCS accelerating cavity are shown in Table **3.1**.

In November 2008, RCS was operated with 11 cavities. In January 2009, a shunt impedance of cavity No. 7 suddenly decreased[55]. After inspecting inside of the cavity, damages on two cores in tank 4 were found out of 18 cores in it. Especially, one core is buckled and elevated at the inner diameter, so that layers of FINEMET at the point are broken. The buckling is the cause of the decrease of the shunt impedance. After that, similar damages appeared many times. As of Mar 11th, 2010, 25 cores out of 90 cores installed in cavity No. 3, 4, 5, 6, 7 has been damaged. Two of them showed the decrease of their shunt impedances. An operation time when the decrease of impedance appears is approximately 1,000 hrs.

A photograph of buckling is shown in Figure **3.1**. The elevation of approximately 1 cm is seen at the inner diameter of the core. Furthermore, FINEMET is rusted by water coming through the damaged area.

We need investigate the cause of the buckling in order to design a new cavity because the new cavity will be loaded with FINEMET cores, too. We suspected the cause of the buckling was thermal stress caused by a heat in the cores. Simulations for investigating the buckling problem were performed by means of ANSYS. ANSYS is an engineering simulation software. The calculation of power loss per core is shown in section 3.2, results of the simulation for the thermal stress were shown in section 3.3, and results of the compression test were shown in section 3.4.

Table 3.1: Sizes of presently installed RCS cores

	thickness [mm]	inner diameter [mm]	outer diameter [mm]
RCS core	35	371 (with a collar)	850

Figure 3.1: A picture of a buckled core (left). A closeup of the buckled area.

3.2 Calculation for power loss per core

The power loss of the presently installed RCS core is approximately 6 kW per core. The value is based on the temperature increase of cooling water. We calculated the power loss by hand and compared with 6 kW. An accelerating pattern of RCS is shown in Figure **3.2**. Solid line is the accelerating voltage of fundamental mode, broken line is the accelerating voltage of secondary mode, and dotted line is the frequency. Secondary mode is not considered in the calculation.

The number of accelerating cavities installed in RCS is eleven and one cavity has three gaps, so that the accelerating voltage per gap $V_{gap}(t)$ can be written as

$$V_{gap}(t) = \frac{V(t)}{(11\text{cavites}) \times (3\text{gaps})} = \frac{V(t)}{33}, \tag{3.1}$$

where V(t) is a function representing the solid line in Figure **3.2**.

We apply Faraday's law to an integral pass shown in Figure **3.3**.

$$\oint E dc = -\iint_S \frac{\partial B(r,t)}{\partial t} dS \tag{3.2}$$

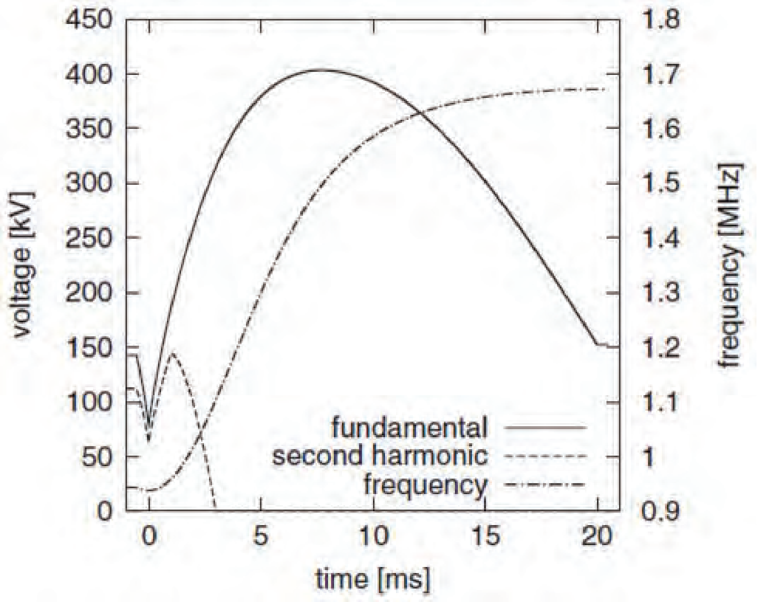

Figure 3.2: A ramping pattern of RCS. The accelerating voltage in the graph is the value per round of RCS.[57]

Left-hand-side is a line integral and right-hand-side is a surface integral.

Because a strength of magnetic field is inversely proportional to r, it can be written as

$$B(r,t) = \frac{\alpha(t)}{r} e^{j\omega(t)t}. \tag{3.3}$$

Substituting equation 3.3 to equation 3.2, the right-hand-side can be written as

$$\begin{aligned}
\text{(Right-hand-side)} &= -\left[\alpha'(t) + j\alpha(t)\left(\omega(t) + \omega'(t)t\right)\right] e^{j\omega(t)t} \iint\limits_{S} \frac{1}{r} dS && (3.4) \\
&= -\left[\alpha'(t) + j\alpha(t)(\omega(t) + \omega'(t)t)\right] e^{j\omega(t)t} \iint\limits_{\substack{\text{cross-section} \\ \text{of a core}}} \frac{1}{r} dS \times 6\text{cores} && (3.5) \\
&= -6 \times 2.864 \times 10^{-2} \times \left[\alpha'(t) + j\alpha(t)\left(\omega(t) + \omega'(t)t\right)\right] e^{j\omega(t)t}. && (3.6)
\end{aligned}$$

Where, the first term $\alpha'(t)$ in the parenthesis has an order of $\alpha(t)/(10^{-3}[s]) = \alpha(t) \times 10^3$ and the second term has an order of $\alpha(t) \times 10^6$, so that the first term is negligible. Therefore, equation 3.6 can be written as

$$\text{(Right-hand-side)} = 6 \times 2.864 \times 10^{-2} \times \alpha(t)\left(\omega(t) + \omega'(t)t\right) e^{j(\omega(t)t - \pi/2)}. \tag{3.7}$$

Hence,

$$\text{(Left-hand-side)} = 6 \times 2.864 \times 10^{-2} \times \alpha(t)\left(\omega(t) + \omega'(t)t\right) e^{j(\omega(t)t - \pi/2)} \equiv V_{gap}(t) e^{j(\omega(t)t - \pi/2)}. \tag{3.8}$$

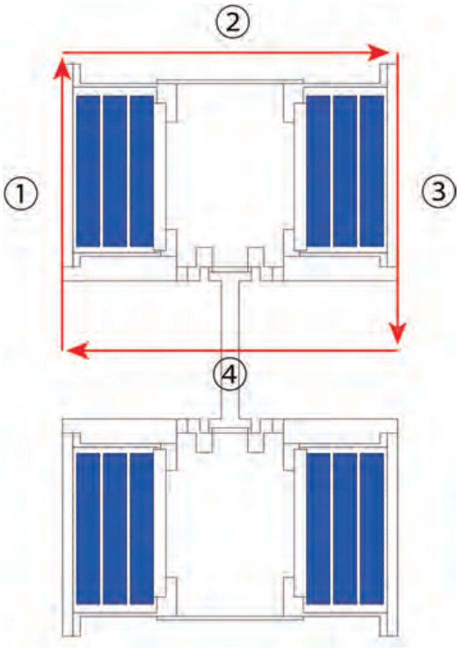

Figure 3.3: An integration path for Faraday's law. The accelerating voltage for one gap is derived by a line integral of electric fields on the path. Integrals on ① and ③ are zero because they are perpendicular to electric fields. An integral on ② is also zero because no electric field exists. An integral on ④ equals the accelerating voltage for one gap.

Therefore, α of t can be expressed as

$$\alpha(t) = \frac{V_{gap}(t)}{6 \times 2.864 \times 10^{-2} \times (\omega(t) + \omega'(t)t)}. \tag{3.9}$$

Hence, a stored energy $U(t)$ at a certain time t for one core is written as

$$U(t) = \int_{\text{core volume}} \frac{1}{2\mu(t)} \left| \frac{1}{\sqrt{2}} B(r,t) \right|^2 dV \tag{3.10}$$

$$= 6.75 \times 10^6 \times \frac{1}{\mu_s'(t)} \left(\frac{V_{gap}(t)}{\omega(t) + \omega'(t)t} \right)^2 \int_{\text{core volume}} \frac{1}{r^2} dV \tag{3.11}$$

$$= 1.22 \times 10^6 \times \frac{1}{\mu_s'(t)} \left(\frac{V_{gap}(t)}{\omega(t) + \omega'(t)t} \right)^2, \tag{3.12}$$

where $\mu(t) = \mu_0 \mu_s'(t)$. $\mu_s'(t)$ is a real part of relative permeability of the core. A loss of the core at a certain time t can be expressed as

$$P = \omega(t)U(t)\left(\tan\delta\right)(t) = 1.22 \times 10^6 \times \frac{\omega(t)}{\mu_s'(t)} \left(\frac{V_{gap}(t)}{\omega(t) + \omega'(t)t} \right)^2 \left(\tan\delta\right)(t)dt. \tag{3.13}$$

Considering the period of the pattern is 40 ms and the voltage is applied for 20 ms, the average loss $\bar{P}$ can be written as

$$\bar{P} = \frac{1.22 \times 10^6}{40 \times 10^{-3}} \int_0^{20\times10^{-3}} \frac{\omega(t)}{\mu_s'(t)} \left(\frac{V_{gap}(t)}{\omega(t) + \omega'(t)t} \right)^2 (\tan\delta)\,(t)dt. \tag{3.14}$$

The time dependencies of μ_s', μ_s'', and tanδ are shown in Table **3.2**. The time dependencies of the frequency and V_{gap} in Table **3.2** are obtained from Figure **3.2**.

Table 3.2: Time dependences of the properties of the presently installed cavity

time [ms]	0	5	10	15	20
frequency [MHz]	0.94	1.29	1.58	1.65	1.67
$\mu_s'(t)$	1919	1510	1296	1254	1242
$\mu_s''(t)$	3087	2515	2206	2145	2128
(tanδ)(t)	1.61	1.67	1.70	1.71	1.71
V_{gap}(t) [V]	2.42×10^3	1.15×10^4	1.18×10^4	9.09×10^3	4.55×10^3

The time derivative of the frequency in Table **3.3** is derived by differentiating the function of the frequency in Figure **3.2**.

Table 3.3: Time derivatives of the frequencies

time [ms]	0	5	10	15	20
A time derivative of frequency [Hz/s]	8.67×10^7	6.16×10^7	3.65×10^7	1.14×10^7	-1.37×10^7

Parameters in Table **3.2** and **3.3** are assigned to the equation 3.14 and the plot of the integrand is obtained as shown in Figure **3.4**.

The integral part of $\bar{P}$ is calculated by substituting the integrand which is derived with a fitting in Figure **3.4**. The integral part is written as

$$\text{(Integral part)} = 1.88 \times 10^{-4}. \tag{3.15}$$

Hence,

$$\bar{P} = \frac{1.22 \times 10^6}{40 \times 10^{-3}} \times 1.88 \times 10^{-4} = 5.73 \text{ [kW]}. \tag{3.16}$$

This value is consistent with the value of 6 kW which is obtained from the temperature rise of the cooling water. To calculate more accurately, it should be taken into account that the frequency of input power does not always stay at the resonance point of the cavity.

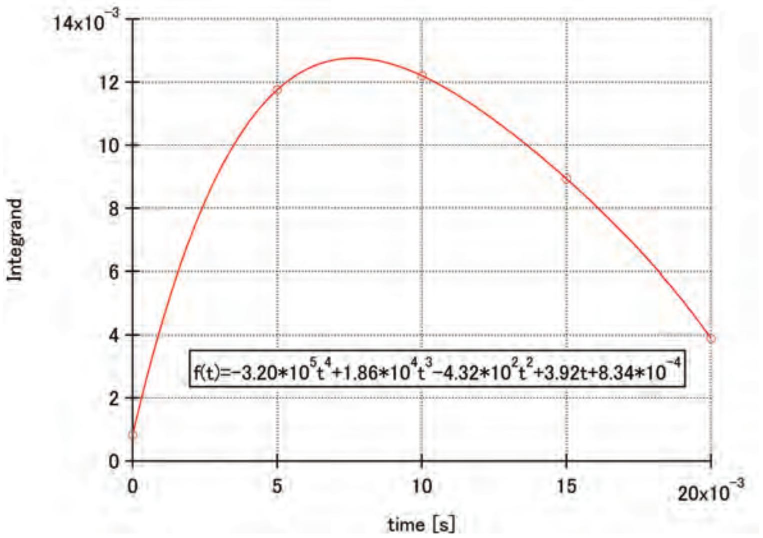

Figure 3.4: A plot of the integrand which is in the equation 3.14

3.3 Calculation for Thermal Stress

Accelerating cavities in RCS are loaded with FINEMET cores. The cores are fabricated by winding amorphous ribbons into a toroidal core. The ribbons are coated with silica on one surface. The silica works as an insulator. As mentioned above, a phenomenon that cores are buckled and its impedance decreases appears while RCS is in operation. We suspected a cause of the buckling is the thermal stress on the cores. We performed a simulation to identify the cause by means of ANSYS. The calculation of thermal stress with a micro model is shown in this section.

3.3.1 Structure of presently installed RCS cavity

There are three types of cores. A core model called "Type 3" is used in the simulation. The cross-section of Type 3 is shown in Figure **3.5**. This type of core is applied with low viscous epoxy resin impregnation and surface coating (high viscous epoxy resin + glass cloth = 300μm). On the inner diameter of the core, a cylindrical G-10 collar whose wall thickness is 2 mm is attached. Type 3 core is damaged with the greatest numbers among three types. Following parameters are required to simulate the thermal stress in the core.

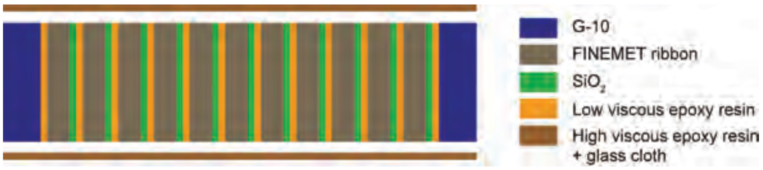

Figure 3.5: A schematic view of a cross-section of a core

- Young's ratio
- Poisson's ratio
- Thermal expansion
- Thermal conductivity

The Young's ratio, Poisson's ratio and thermal expansion of FINEMET are given by Hitachi Metal, Ltd.. The thermal conductivity of FINEMET was measured. The next subsection reports the measurement. The Young's ratio, Poisson's ratio, thermal expansion, and thermal conductivity of epoxy resin are obtained from the reference [60].

3.3.2 A measurement for a thermal conductivity of FINEMET core

A thermal conductivity of FINEMET is dispensable for the calculation of thermal stress. We obtained the thermal conductivity by measuring a coefficient of thermal diffusion of the FINEMET core by means of the laser flash method in cooperation with National Institute of Advanced Industrial Science and Technology (AIST). The configuration of the laser flash method is shown in Figure **3.6**. It is the method to obtain the coefficient of thermal diffusion by measuring the increase of the temperature on the back surface of the sample after applying a heat flux on its forward surface with a pulsed YAG laser. Half time method is used in the measurement. Details of half time method is shown in a following paragraph.

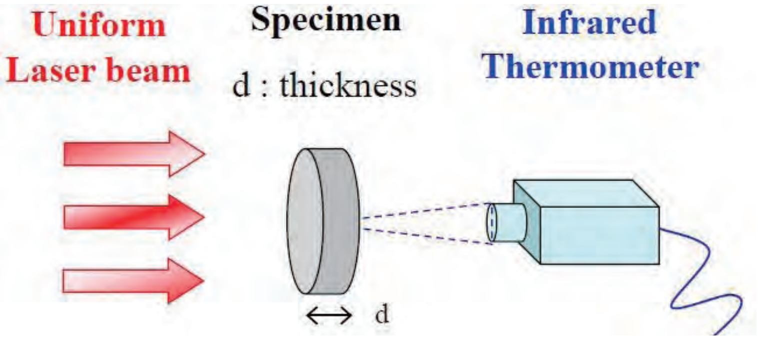

Figure 3.6: A schematic view of the laser flash method[62]

Initial temperature of a solid in adiabatic state, which has density D [g/cm^3], specific heat at constant pressure C [cal/g/°C], thickness L [cm] is defined as T(x,0). Then, a temperature distribution at time t is written as[63]

$$T(x,t) = \frac{1}{L}\int_0^L T(x,0)dx + \frac{2}{L}\sum_{n=1}^{\infty} \exp\left(\frac{-n^2\pi^2\alpha t}{L^2}\right)\cos\left(\frac{n\pi x}{L}\right)\int_0^L T(x,0)\cos\left(\frac{n\pi x}{L}\right)dx, \tag{3.17}$$

where α [cm^2/s] is a coefficient of thermal diffusion. Assuming heat Q [cal/cm^2] is applied isotropically and absorbed in depth g [cm] at $x = 0$ and $t = 0$, $T(x, 0)$ can be written as

$$T(x,0) = \frac{Q}{DCg} \ (0 < x < g), \tag{3.18}$$

$$T(x,0) = 0 \ (g < x < L). \tag{3.19}$$

Therefore, equation 3.17 can be expressed as

$$T(x,t) = \frac{Q}{DCL}\left[1 + 2\sum_{n=1}^{\infty} \cos\left(\frac{n\pi x}{L}\right) \frac{\sin\frac{n\pi g}{L}}{\frac{n\pi g}{L}} \exp\left(\frac{-n^2\pi^2\alpha t}{L^2}\right)\right]. \tag{3.20}$$

The opaque has small g, so that, the sinusoidal function can be approximated as

$$\sin\frac{n\pi g}{L} \approx \frac{n\pi g}{L}. \tag{3.21}$$

The temperature rise on the back surface ($x = L$) can be written as

$$T(L,t) = \frac{Q}{DCL}\left[1 + 2\sum_{n=1}^{\infty}(-1)^n \exp\left(\frac{-n^2\pi^2\alpha t}{L^2}\right)\right]. \tag{3.22}$$

Two nondimensional parameters are introduced.

$$V(L,t) \equiv \frac{T(L,t)}{T_M} \tag{3.23}$$

$$\omega \equiv \frac{\pi^2\alpha t}{L^2} \tag{3.24}$$

where T_M $(=\frac{Q}{DCL})$ is a peak temperature on the back surface. Then, a following equation is deduced.

$$V = 1 + 2\sum_{n=1}^{\infty}(-1)^n \exp\left(-n^2\omega\right) \tag{3.25}$$

The plot of this function is shown in Figure **3.7**. $\omega = 1.38$ at $V = 0.5$ is obtained from the plot. Substituting the value into definition 3.24, α is derived as

$$\alpha = \frac{1.38L^2}{\pi^2 t_{\frac{1}{2}}}, \tag{3.26}$$

where $t_{\frac{1}{2}}$ is a time when the temperature of the back surface is half of its peak value ($V = 0.5$).

Hence, a thermal conductivity λ [cal/cm/°C] is obtained from a following equation.[64]

$$\lambda = \alpha CD \tag{3.27}$$

Because the core has the structure that FINEMET ribbon is wound into a toroidal core, the thermal conductivity must be anisotropic. As shown in Figure **3.8**, measurements in

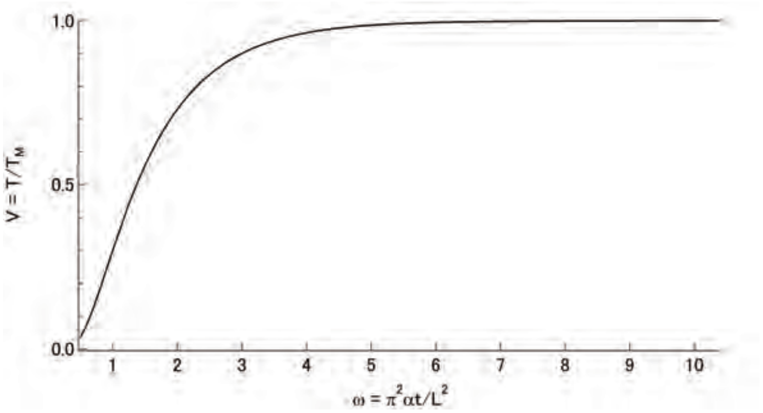

Figure 3.7: A nondimensional plot of the temperature of the back surface

two cases were performed. One is that the laser is applied perpendicular to FINEMET layers (radial direction), the other is that the laser is applied parallel to the layers (circumferential direction and beam direction). Two samples were prepared for each measurement. Measurements were performed twice for each samples. The results are shown in Table **3.4**. The specific heat of the core at the constant pressure was measured by the measurement service with Physical Properties Measurement System (PPMS) at Cryogenic Research Center in the University of Tokyo.

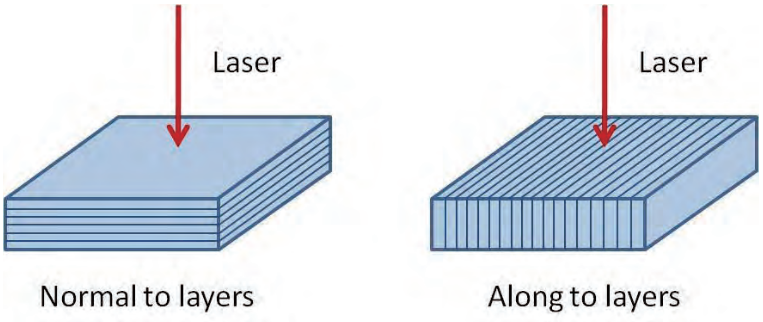

Figure 3.8: Definitions of the directions of the laser

Obtained anisotropic-thermal-conductivity of FINEMET cores are,
0.6 [W/m/K] for radial direction, and
7.1 [W/m/K] for circumferential direction and beam direction.[59]

3.3.3 Calculation for thermal stress with micro model

Calculations for thermal stress on the core were performed with a model which represents the layered structure of the core (micro model). Considering the aging property of the epoxy resin, calculations in two cases were performed.

1. Percentages of Young's ratio were changed into 100% , 10% ,and 1 % .

Table 3.4: Results of the measurements for the thermal conductivity

	Normal to layers				Along to layers			
	Sample 1		Sample 2		Sample 3		Sample 4	
	Trial 1	Trial 2	Trial 1	Trial 2	Trial 1	Trial 2	Trial 1	Trial 2
Mass [g]	1.00		1.59		1.48		1.65	
Vertical [mm]	10.21		8.59		9.08		10.19	
Horizontal [mm]	9.83		9.56		9.47		9.55	
Height [mm]	1.84		3.42		3.04		3.09	
Volume [mm^3]	184.67		280.85		261.40		300.70	
Density [g/cm^3]	5.39		5.66		5.67		5.49	
Specific heat capacity [J/g/K]	0.500							
Half time [s]	2.20	2.15	6.95	7.36	0.497	0.502	0.525	0.519
Thermal diffusivity [10^{-7}m^2/s]	2.14	1.93	2.34	2.21	25.8	25.6	25.2	25.6
Thermal conductivity [W/m/K]	0.577	0.520	0.661	0.624	7.317	7.241	6.930	7.018

2. A contact simulation for the no impregnation core was performed.

ANSYS is utilized for these calculations. All of them are two dimensional calculations.

1. Model of 20,000 layers

The structure of the core is shown in Figure **3.9**. The number of the layers of FINEMET is approximately 20,000. Sizes of each material are shown in Table **3.6**. The model of 2,000 layers (thickness of FINEMET, impregnated epoxy resin, water proof coating, and G-10 collar are 180μm, 60μm, 300μm, and 2 mm, respectively) is used for the calculation of the temperature distribution. To represent a real structure that FINEMET ribbons and epoxy resins are laminated alternately, the model of 20,000 layers (FINEMET and epoxy are approximately 10,000 layers for each) is required. However, the number of layers is too much and impossible to model it on a computer, so that the model of 2,000 layers is adopted for the calculation of the temperature distribution. This model corresponds to the model that that the number of layers in Figure **3.9** is reduced to 2,000.

Heat distribution used for the calculation was derived by normalizing the distribution of squared magnetic-flux-density with the power loss per core (6kW). The magnetic-flux-density was derived from a simulation with HFSS. In the simulation, 30°C for isotropic temperature of coolant and 500 [W/m^2/K] for isotropic heat transfer coefficient on the surfaces of the core are assumed.

As shown in Figure **3.10**, adiabatic conditions are applied at inner diameter and outer diameter of the core, and center of the core also has an adiabatic condition because of the symmetry of the model.

The thermal conductivity of each material are shown in Table **3.5**. The measured thermal conductivity of circumferential and beam directions is used for simple FINEMET.

The temperature distribution obtained from the calculations is shown in Figure **3.11**.

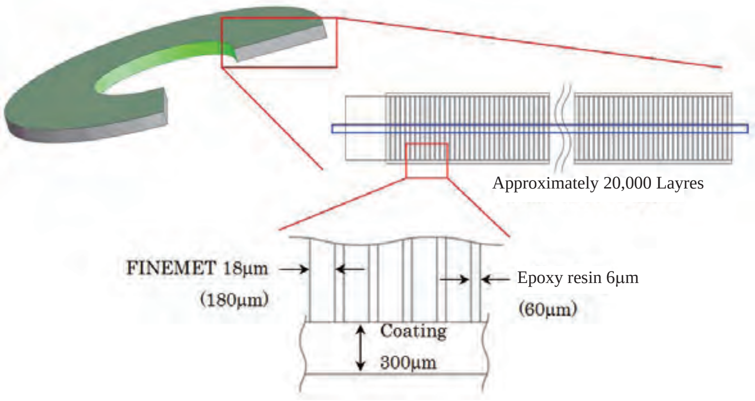

Figure 3.9: A structure of the core

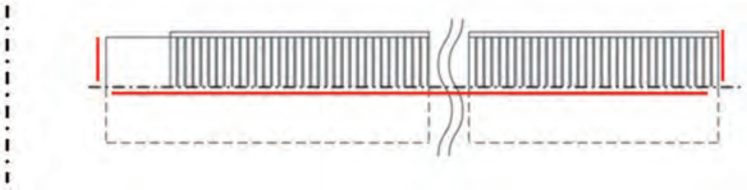

Figure 3.10: An adiabatic condition on the core for the simulation of the core temperature

Table 3.5: Thermal conductivities of materials used in the simulation

FINEMET	7.1
Epoxy resin, water proof coating[60]	0.2
G-10[60]	radial: 0.4 circumference and beam direction: 0.8

Using the temperature distribution obtained above, a simulation for the thermal stress against various Young's ratios of epoxy was performed. This variation represents the aged deterioration of the epoxy resin. The model of 20,000 layers was used for the simulation. In this case, 20,000 layers was feasible, because only the elements along the center line of the core were used. These elements are in the area surrounded by blue lines in Figure **3.9**. As shown in Figure **3.12**, displacement of upside and downside of the model are assumed to be constraint along the direction of center axis. Properties of each material are shown in Table **3.7**. Measured values in Hitachi Metal are used for properties of FINEMET.

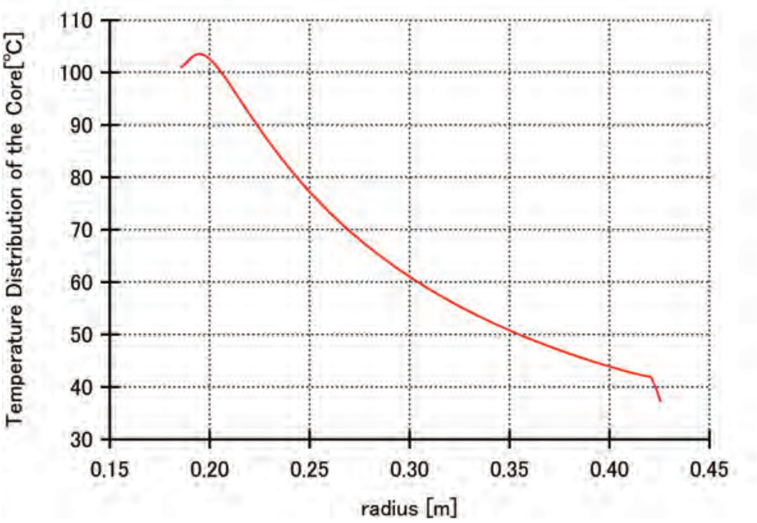

Figure 3.11: A temperature distribution along radial direction in the core, which is obtained from the simulation

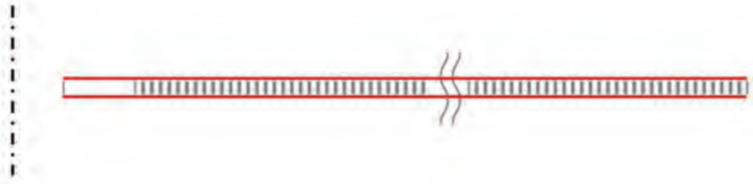

Figure 3.12: A condition of constraint against displacements of the elements, which is used in simulations for thermal stresses

Figure **3.13**, **3.14**, and **3.15** are results of the calculations for circumferential components of thermal stress which are applied on FINEMET, epoxy resin, and G-10 collar, respectively. The percentages of Young's ratio of epoxy resin are changed into 100% , 10% , and 1% . Plus and minus values represent tensile and compressive stresses, respectively. The result shows the stresses drastically decrease as the Young's ratio of the epoxy resin decreases. A conclusion is that a methods to decrease Young's ratio of cores, for example, adopting no resin core, using soft resin, transform the epoxy resin into sponge, are effective. In fact, the cores without epoxy resin among presently installed RCS cores have never experienced buckling.

2. Contact simulation

No impregnation is assumed. Only FINEMET ribbon was input for modeling and the contact simulation was performed. The temperature distribution in Figure **3.11** was used again. Values in Table **3.7** are used for FINEMET properties. A result in Figure **3.16** was obtained for a circumferential component of stress. This result shows the circumferential component of stress is less than 20 kPa. A large stress can be seen at the inner diameter.

Table 3.6: Sizes of materials used in the simulations for the thermal stresses

	width [mm]	thickness [μm]
FINEMET ribbon	35	18
Epoxy resin	35	6
Water proof coating	-	300

Table 3.7: Properties of each material

	Young's ratio [GPa]	Poisson's ratio	Coefficient of thermal expansion [10^{-6}/K]
FINEMET ribbon	200	0.32	10.6
Epoxy resin[60]	3.2 or 0.32 or 0.032	0.34	60
G-10[60]	7.8	0.32	radial: 23 circumference: 7 beam direction: 7

This stress is caused that one end of the FINEMET ribbon contacts with the G-10 collar, and is unavoidable. A part of Figure **3.16** is zoomed and shown in Figure **3.17**. Periodical spikes are seen. A reason for this phenomenon is that input values of the temperature are only 100 points, so that temperature varies at every 24 cm. Spikes appear at the points. If smooth distribution of the temperature is used, the stress is expected to be less than 20 kPa. Displacement of FINEMET ribbon and circumferential component of stress at contact point are shown in Figure **3.18** and **3.19**, respectively. The results of the simulation showed that thermal stresses drastically decrease by using the core without epoxy resin. Therefore, cores for a new cavity are not impregnated.

3.4 Compression test for the core

We suspect the cause of the buckling is thermal stress on the core, however, there is no experiment which measures the required stress for the buckling. Therefore, we measured the buckling stress in cooperation with NIMS. In this section, results of the compression test for the core which was performed at NIMS in November 2009 are shown.

Fatigue Testing System

A fatigue-testing-system INSTRON 8802 shown in Figure **3.20** was used for the compression test. TCLP-50KNB of Tokyo Sokki Kenkyujo Co., Ltd. was used for a load cell. 50 kN is possible for the maximum-compression-force. A jig for the compression is shown in Figure **3.21**.

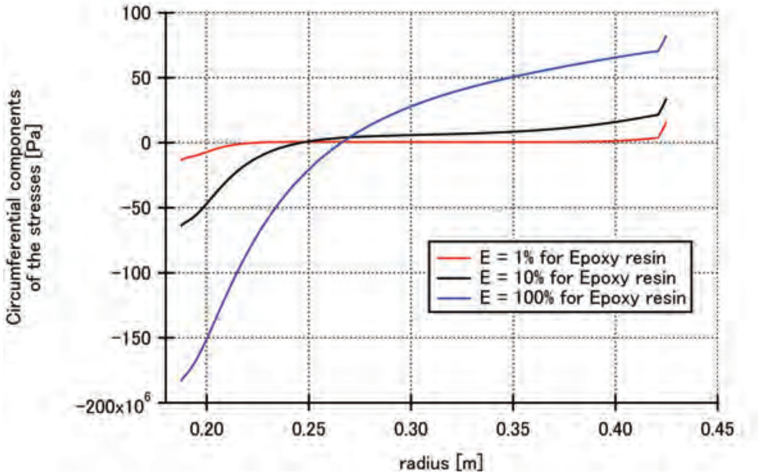

Figure 3.13: Thermal stresses on the FINEMET. Three calculations were performed. The Young's ratio of the epoxy resin (E) is varied in the three cases.

High resolution camera

A transform of the sample by the compression was measured with a high resolution camera shown in Figure **3.22**. The camera monitors the positions of two markers shown in Figure **3.21**. The amount of the deformation of the sample is measured by the camera.

Samples used in this test are not RCS core's but MR core's. They were cut out from quoter sized MR core (product number: KE081-8) and 1/8 sized MR core (product number: unknown) with a diamond cut machine of Ryowa Inc. which was at the machine shop bldg. in KEK. The coating had been damaged at some areas on the surface of the quoter sized core. We cut out samples from non damaged areas. Compression direction is defined as shown in Figure **3.23**.

The direction of the beam axis is selected as the compression direction. Circumferential direction is the best direction because the thermal stress on this direction is the strongest. However, beam direction and circumferential direction are consistent in the meaning of the direction along layers, so that the beam direction was selected. Circumferential direction is not suited for compression because FINEMET layers have a curvature in this direction.

The sample is shown in Figure **3.24**. Original positions of samples and their Young's ratios and buckling stresses are shown in Figure **3.25**. Buckled and sheared samples are shown in Figure **3.26** and **3.27**, respectively. Filling ratios of samples, which are calculated from their volumes and masses, are also shown in Figure **3.25**.

As the result above, Figure **3.28**, **3.29**, **3.30**, and **3.31** are obtained. A plot showing a buckling stress of 129.6 MPa (sample 13) is not a buckling but a shear failure.

As shown in Figure **3.28** and **3.29**, filling ratios and buckling stress are not dependent on positions where samples were cut. Figure **3.30** shows buckling stresses are not dependent on filling ratios. Figure **3.31** shows buckling stresses of samples are proportional to Young's ratios.

All samples except sample 13 are buckled under 70 MPa. The simulation for the

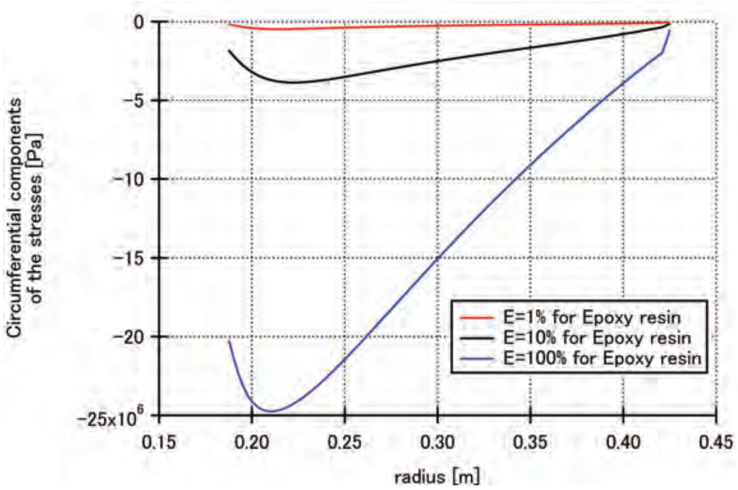

Figure 3.14: Thermal stresses on the epoxy resin

thermal stress in previous section shows the maximum thermal stress in the RCS core is over 70 MPa. The result of this simulation backs the expectation that the cause of buckling is the thermal stress.

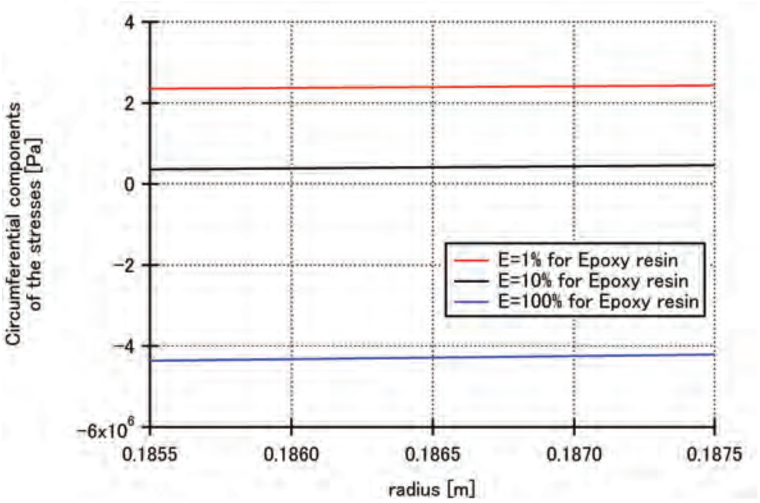

Figure 3.15: Thermal stresses on the G-10

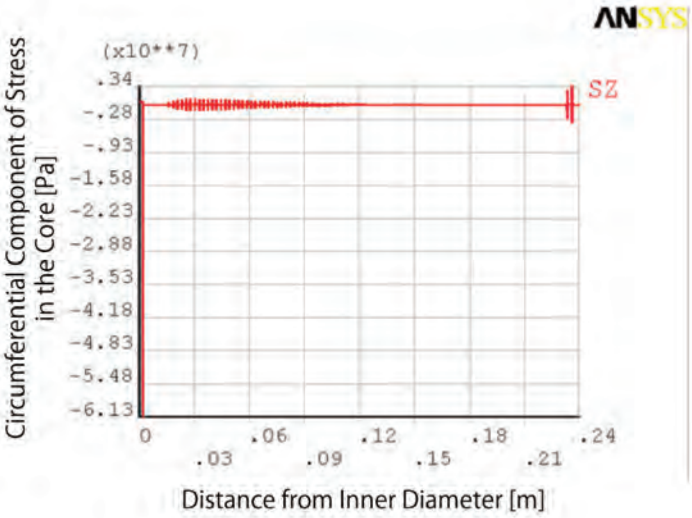

Figure 3.16: A result of the contact simulation

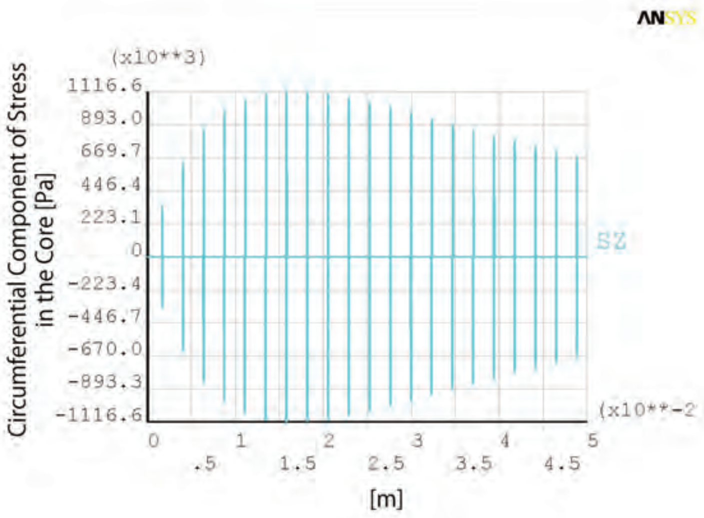

Figure 3.17: A closeup of Figure **3.16**

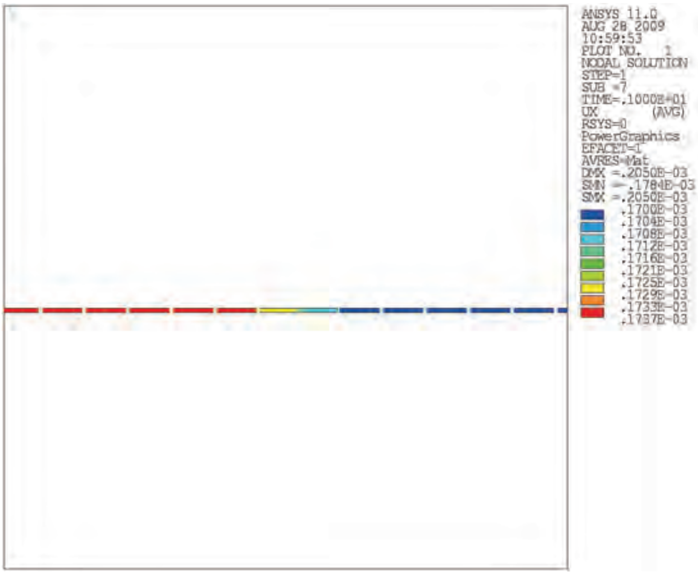

Figure 3.18: Displacement of the elements

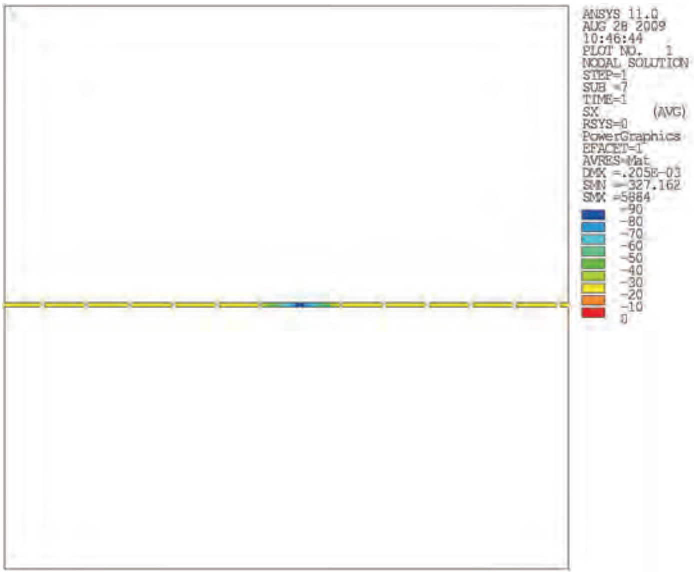

Figure 3.19: A stress emerging at a contact point

Figure 3.20: A fatigue-testing-system "INSTRON 8802" at NIMS

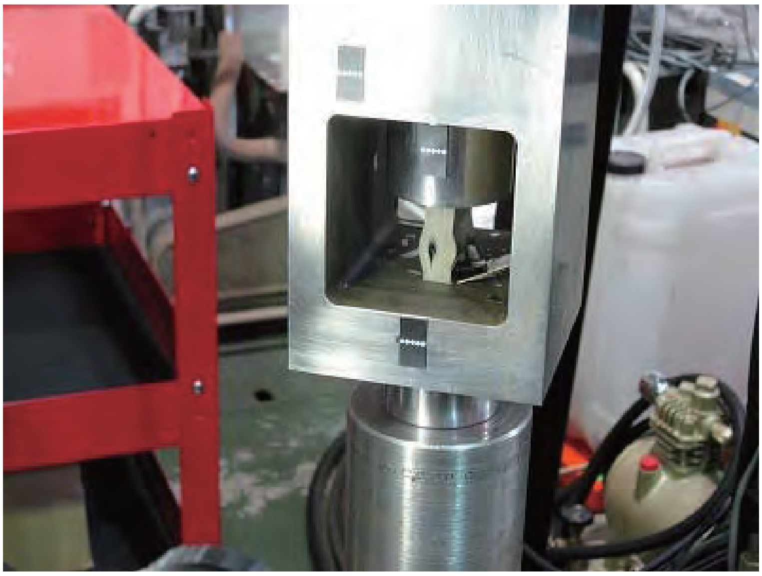

Figure 3.21: A jig for the compression test

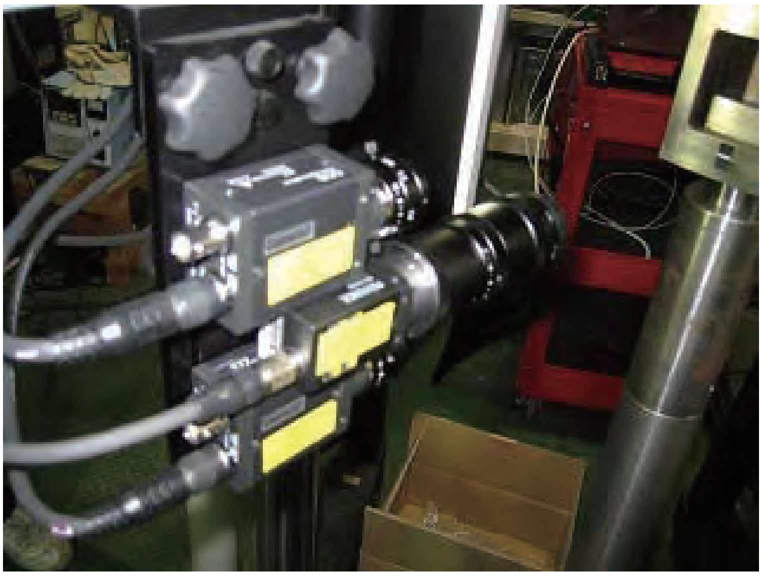

Figure 3.22: A high resolution camera

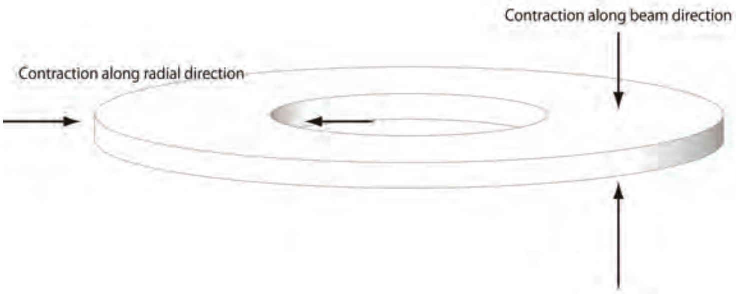

Figure 3.23: A definition of the compressing direction

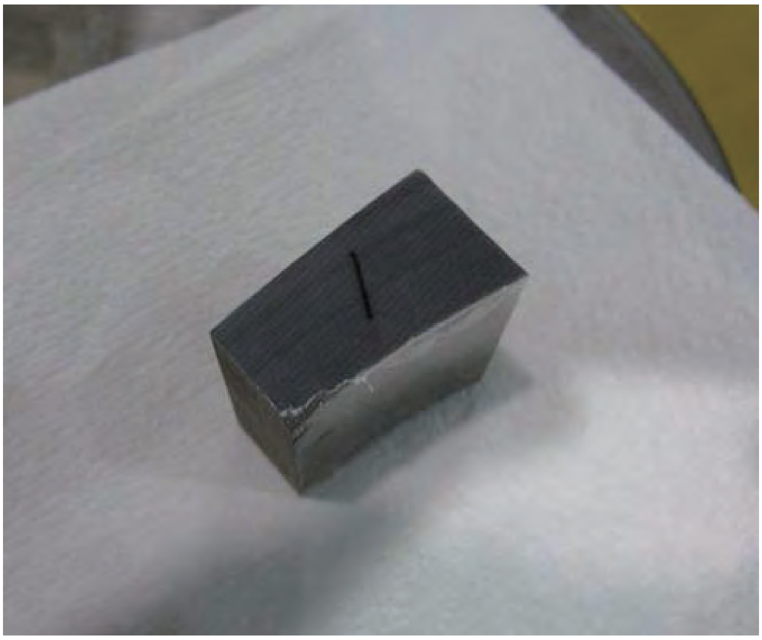

Figure 3.24: A sample for the compression test

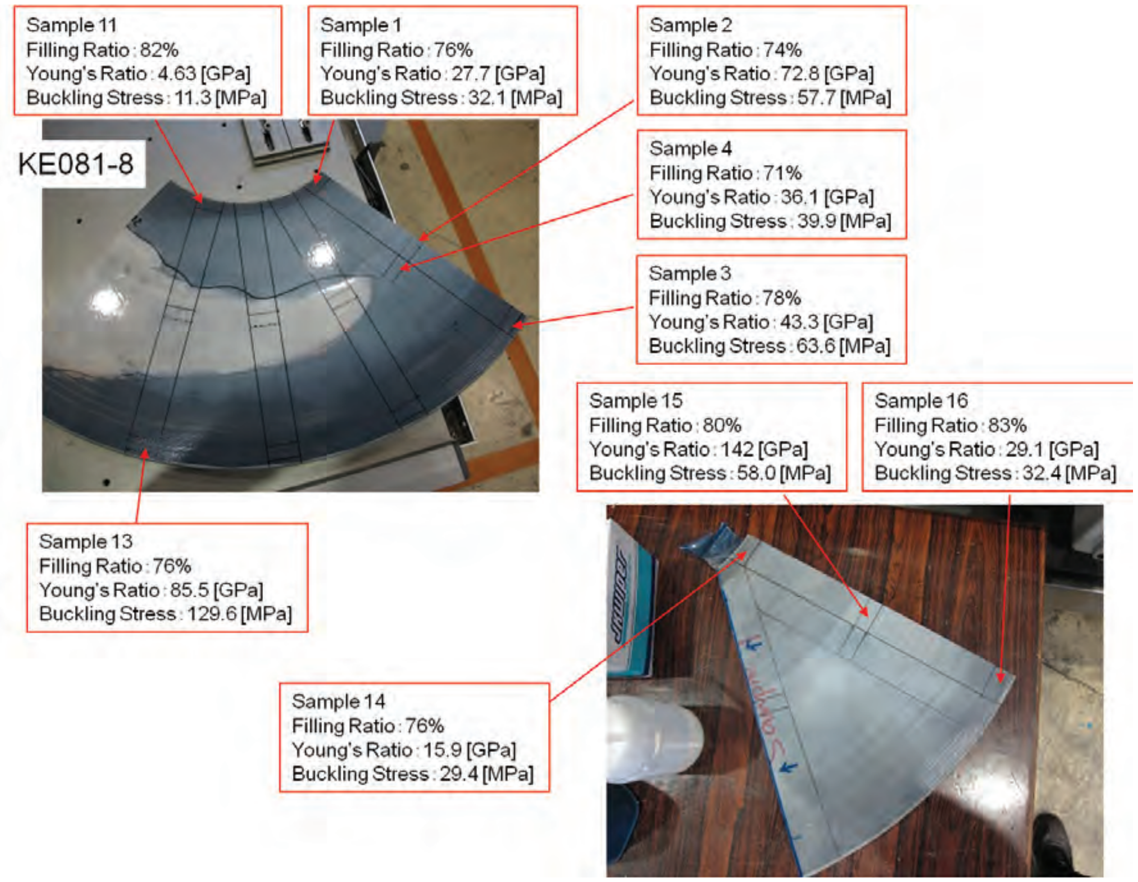

Figure 3.25: Original positions of samples and results of the compression test

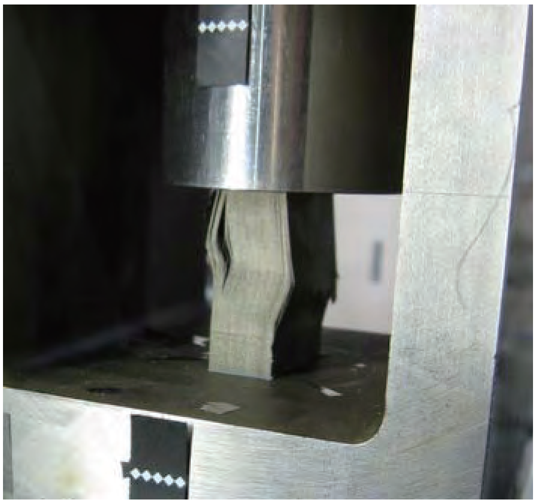

Figure 3.26: A buckled sample

Figure 3.27: A sheared sample

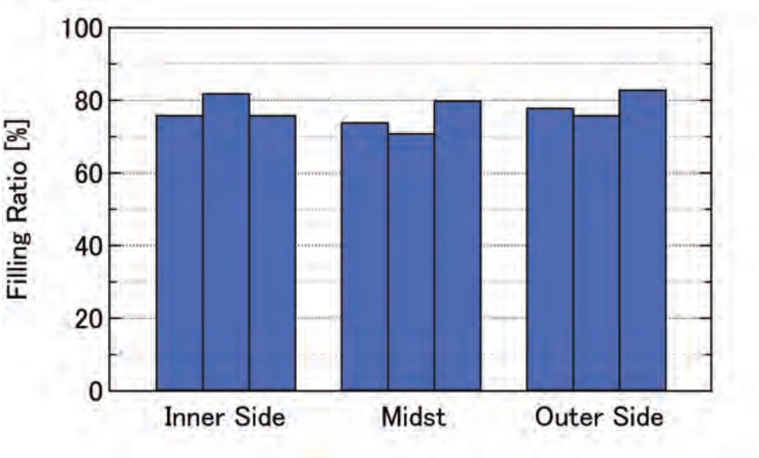

Figure 3.28: A position dependency of a filling ratio

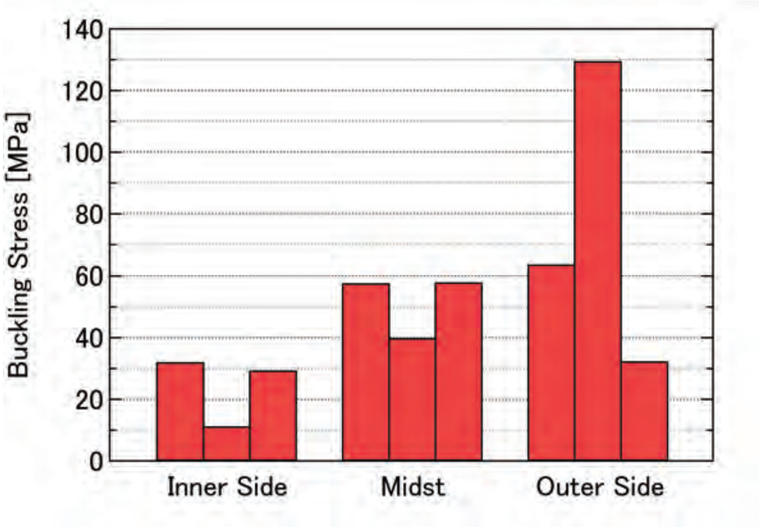

Figure 3.29: A position dependency of a buckling stress

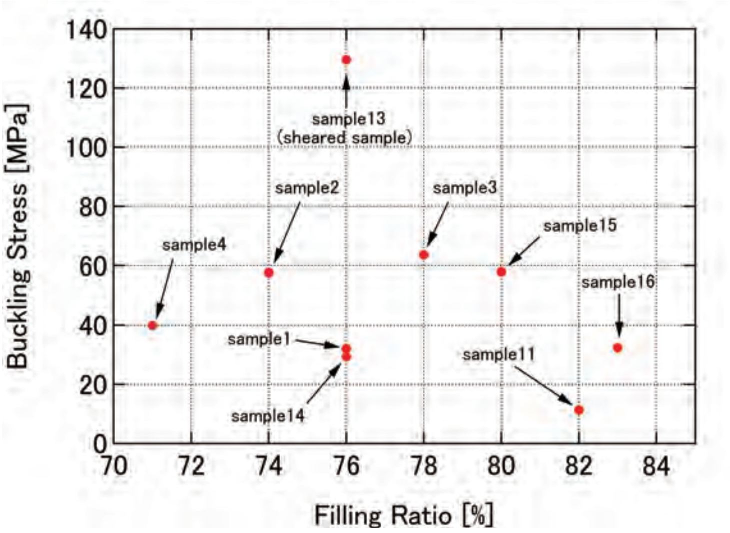

Figure 3.30: A filling ratio dependency of a buckling stress

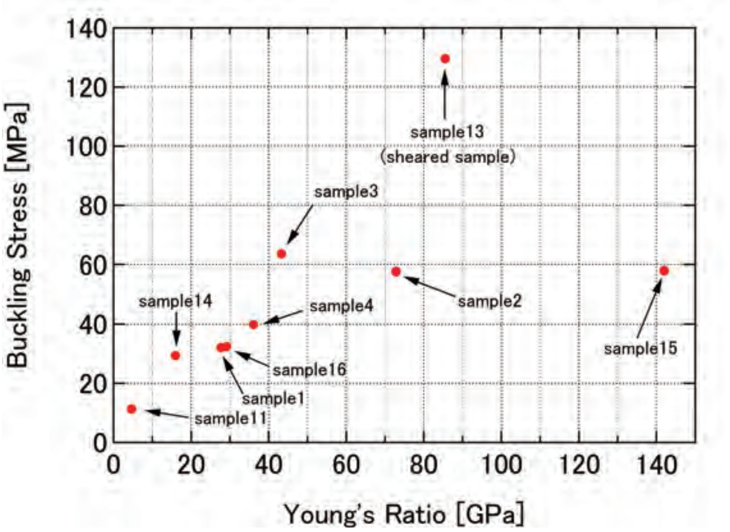

Figure 3.31: A Young's ratio dependency of a buckling stress

Chapter 4

Development of a new RF accelerating cavity loaded with FINEMET cores cooled by Fluorinert

Development of a new cavity is introduced in this chapter. We adopted the cores without impregnation in order to avoid the buckling. Fluorinert is selected as a coolant. First of all, we propose essential parameters for developing an accelerating cavity.

- Resonance frequency
- Shunt impedance
- Q factor

These parameters have to have sufficient values in order to carry out successful development. In addition to these parameters, two more parameters which are specific for our cavity have to be examined.

- Cooling efficiency for the core
- Breakdown voltage on the surface of the core

We will check them in chapter 7.

4.1 Selection of coolant

The coolant is required not to oxidize the cores. We had three candidates. They are Fluorinert, Normal paraffin, and Novec. Properties of them are shown in Table **4.1**.

Table 4.1: Properties of the candidates for the coolant[58]

	FC-3283 (Sumitomo 3M FC-3283)	Normal paraffin (ENEOS Glade L)	Novec (Sumitomo 3M HFE-7300)
Chemical formula	$(C_3F_7)_3N$	$C_{11}H_{24}$, $C_{12}H_{26}$	$C_6F_{13}OCH_3$
Boiling point [°C]	128	190∼210	98
Flash point [°C]	-	71	-
Density [kg/m^3]	1780	751	1660
Dynamic viscosity [m^2/s]	0.59×10^{-6}	1.36×10^{-6}	0.7×10^{-6}
Specific heat [J/kg/K]	1076	2180	1137
Thermal conductivity [W/m/K]	0.0624	0.126	0.062
Breakdown voltage [kV/2.54 mm gap]	43	30	27
Relative permittivity (1 kHz)	1.91	2.0	6.14
Electric loss tangent (1 kHz)	$<4\times10^{-4}$	$\sim1\times10^{-4}$	0.016

Normal paraffin is affordable and has a high breakdown voltage which is favorable as the coolant. But Normal paraffin is not adopted because it is flammable. Novec is not accepted because it has a large permittivity and tanδ, and it has an oxygen in the chemical formula. We concluded the FINEMET cores without impregnation cooled by Fluorinert is the best choice.

4.2 Overview of the accelerating cavity for RCS

The beam energy at injection and extraction of RCS are 181 MeV and 3 GeV, respectively. The circumference of RCS is 348.333 m, so that the frequency for a beam to circulate RCS is 0.47 MHz for 181 MeV, 0.84 MHz for 3 GeV. Because the harmonic number is two, the resonance frequency of RCS cavity should be 0.938 MHz for 181 MeV and 1.67 MHz for 3 GeV. This is twice of an RCS revolving frequency. The accelerating voltage per turn of the ring is proportional to the product of the average radius of the ring and maximum-time-derivative of magnetic-flux-density. The voltage is obtained from the following equation.

$$V_0 \sin(\omega t) = 2\pi R \frac{d(B\rho)}{dt} \tag{4.1}$$

Where, V_0 is the peak voltage, R is the average radius of the ring, ρ is the radius of curvature at a bending magnet. In the case of RCS, R=55.44 m, ρ=12.578 m, sin(ωt)=sin(28.09 [deg])=0.4709 at maximum voltage (at a point of 6 ms in 20 ms cycle) which corresponds to accelerating phase ϕ_s=28.09 deg. Magnetic flux densities around this time are 0.394 [T] and 0.443 [T] at 5 ms, 7 ms, respectively. The time derivative of magnetic-flux-density is calculated as (0.443-0.394)/1×10^{-3}=0.490 [T/s]. Therefore, V_0 ~450 [kV][65]. Ten cavities and one spare cavity are able to be installed in a space of linear section in RCS. One cavity is approximately 2 m long. In the case of ten cavities installation, an accelerating voltage per cavity is 450 [kV] / 10 [cavities] = 45 [kV]. One cavity has 3 gaps, so that an accelerating voltage per gap is 45 [kV] / 3 [gaps] = 15 [kV]. Therefore, a cavity should have a resonance frequency of 0.938-1.67 [MHz] and an accelerating voltage of 15 [kV] per gap. A geometry of a cell is a structure of $\lambda/4$-wave coaxial resonance cavity as shown in Figure **4.1**. It is the structure that 3 cores are installed in each side of the accelerating gap. In this paper, fabrication of a prototype cavity which is loaded with a core module and results of performance test for the cavity are shown. The cross-section of the prototype cavity is shown in Figure **4.2**. A variable vacuum capacitor is attached instead of an accelerating gap. The resonance frequency is tuned to 1.7 MHz by adjusting the capacitor, which is the maximum frequency of the cavity operated in RCS.

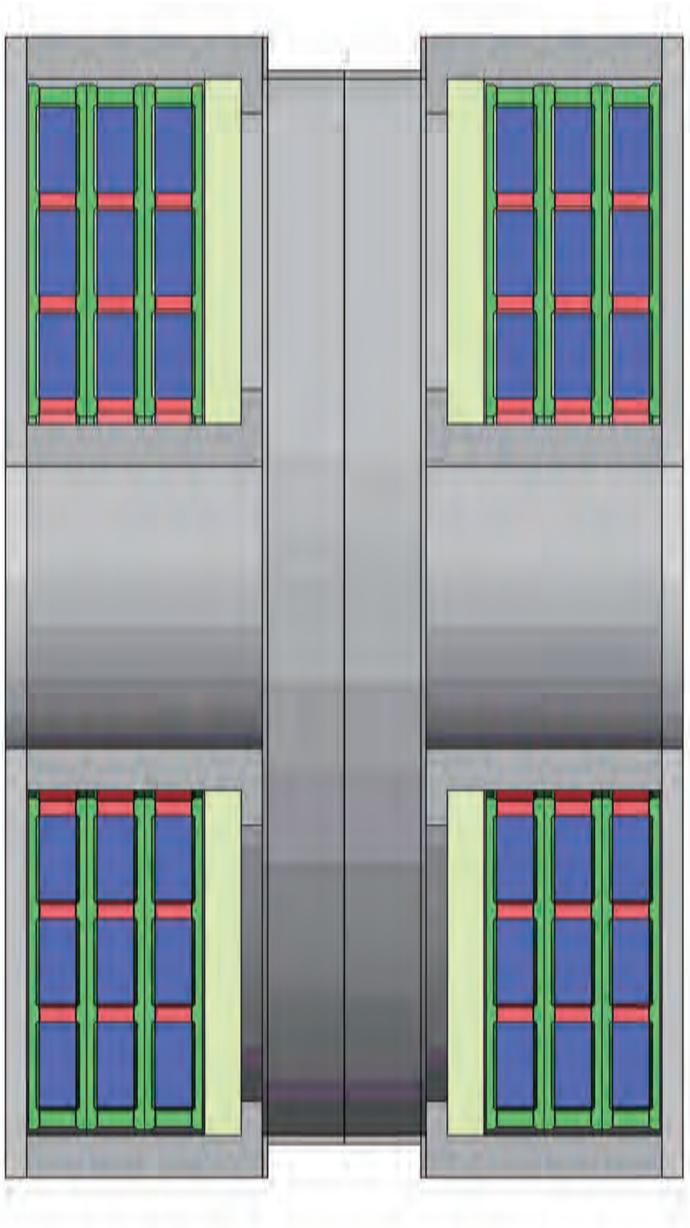

Figure 4.1: A cross-section of the new accelerating cavity

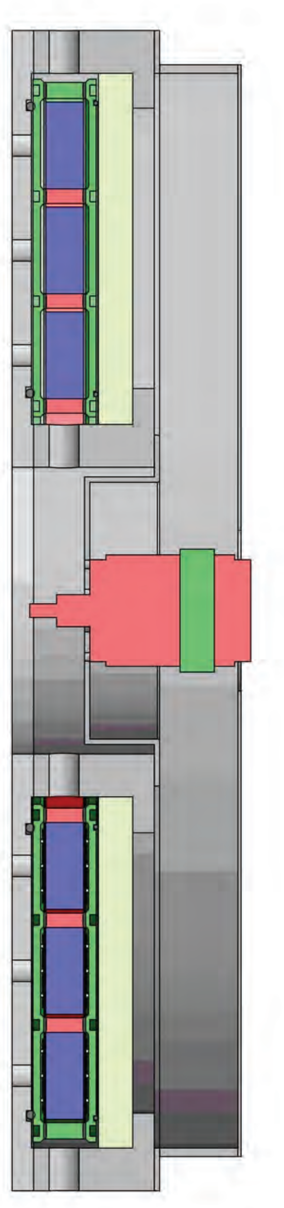

Figure 4.2: A cross-section of the prototype cavity

4.3 FINEMET core module

Presently installed RCS cores are impregnated with epoxy resin and the structure is solid. However, cores which we use are not impregnated because a maximum temperature for the cores is limited by a glass-transmission-temperature of epoxy resin. Furthermore, considering the results in previous section, even a resin which is endurable against heat is available, it should not be used to prevent the buckling. A geometry of the core is a structure that it is radially divided into three. They are called small core, middle core, and large core. Te winding thickness of each core becomes thin, which means the control of wounding stress becomes easy, and the magnetic properties are possible to increase. The thin winding thickness makes it easy to deal with no impregnation core, what we call a "raw core". A structure which is fabricated by binding raw cores with two G-10 plates is called a "core module". The structure is shown in Figure **4.3**. Only collars are structural material and no stress is applied on FINEMET cores (functional material). The aperture surrounded by the G-10 plates and the surfaces of the cores is the flow channel.

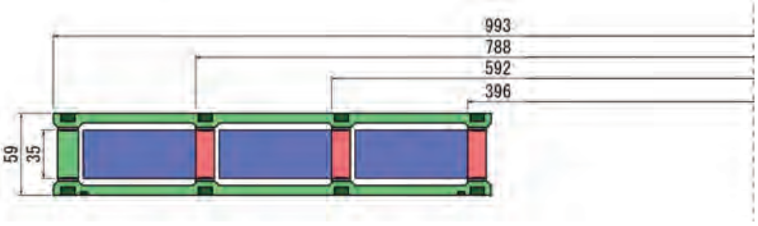

Figure 4.3: A cross-section of a core module

Raw cores have following advantages. **1. Release of thermal stress**

The raw core is not impregnated and soft. It is able to release the thermal stress and prevent the buckling. **2. Self cleaning**

As the surface of the raw core contacts with the coolant directly, self cleaning that seeds of spark are removed by the coolant which flows fast is expected. The coolant enter between FINEMET layers. Seeds move to the surface by diffusion and are removed by the flowing coolant.

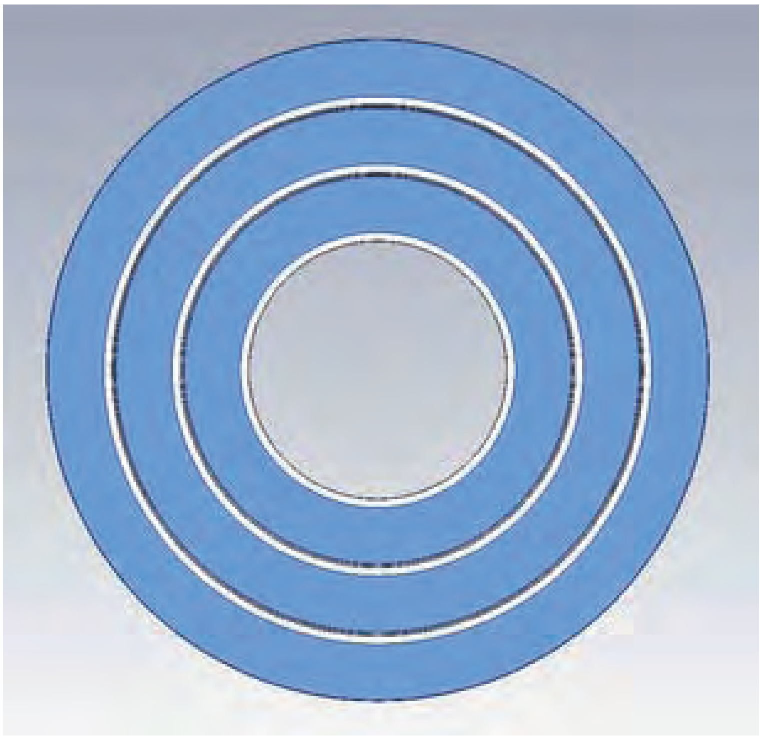

Figure 4.4: A schematic view of the new cores

Table 4.2: Sizes of the new cores

	Inner diameter [mm]	Outer diameter [mm]
Small core	396	558
Middle core	592	754
Large core	788	950

Sizes of small, middle, large cores are decided to make their total cross sections same as that of an RCS core. Their configuration and sizes are shown in Figure **4.4** and Table **4.2**, respectively. Values of relative permeability, shunt impedance, and μ_pQf are shown in Table **4.3** and **4.4**, respectively.

Table 4.3: Permeabilities of the new cores

μ_s'	0.5 MHz	1 MHz	5 MHz	10 MHz
Small core	4100	2400	760	480
Middle core	4300	2600	1000	730
Large core	4100	2700	1200	860
Average	4200	2600	980	690

μ_s''	0.5 MHz	1 MHz	5 MHz	10 MHz
Small core	4400	3200	1200	780
Middle core	5000	3400	1200	820
Large core	4300	3000	1200	810
Average	4600	3200	1200	800

Table 4.4: Shunt impedances and $\mu_p Qf$ of the new cores

	Small core		Middle core		Large core		Sum of three cores	Core module
	$R_p[\Omega]$	μ_pQf	$R_p[\Omega]$	μ_pQf	$R_p[\Omega]$	μ_pQf	$R_p[\Omega]$	$R_p[\Omega]$
0.5[MHz]	46.9	3.14	34.6	3.27	25.0	3.08	106.5	103.7
1[MHz]	56.9	3.81	42.7	4.04	32.4	3.99	132	127
5[MHz]	95.1	6.37	83.2	7.87	70.5	8.69	248.8	222.3
10[MHz]	121.3	8.12	117.8	11.14	104.5	12.89	343.6	287.9

4.4 Fluorinert

FINEMET which is an Fe-based magnetic alloy can be oxidized. A coolant for cores must not contain oxygen. Fluorinert (FC-3283, Sumitomo 3M, Inc.) which is a perfluorinated inert liquid is used. Properties of Fluorinert and water are shown in Table **4.5**.

Table 4.5: A comparison of properties of Fluorinert and water

	FC-3283	Water[70]
Chemical formula	$(C_3F_7)N_3$	H_2O
Boiling point [°C]	128	100
Density [kg/m^3]	1780	992.215
Dynamic viscosity [m^2/s]	0.59×10^{-6}	0.6580×10^{-6}
Specific heat [J/kg/K]	1076	4192
Thermal conductivity [W/m/K]	0.0624	0.628
Break down voltage [kV/2.54 mm gap]	43	-
Relative permittivity (1 kHz)	1.91	81
Electric loss tangent (1 kHz)	$<4\times10^{-4}$	0.16
Heat transfer coefficient [W/m^2/K]	530 (turbulence)	500 (laminar)
Price [thousands yen/L]	∼19	-

By using FC-3283 on the condition of turbulence, the cooling efficiency is comparable with presently installed cavities. Reasons of selecting FC-3283 are listed below.

- ◦ The breakdown voltage is high.
- ◦ The relative permittivity is low.
- ◦ The kinetic viscosity is low.
- ◦ The boiling point is high.

An ion decomposition rate of FT-3283 is shown in Figure **4.5**. Though the boiling point is high, its ion decomposition rate begins increasing around 120°C, so that the temperature of Fluorinert in operation must be lower than 120°C.

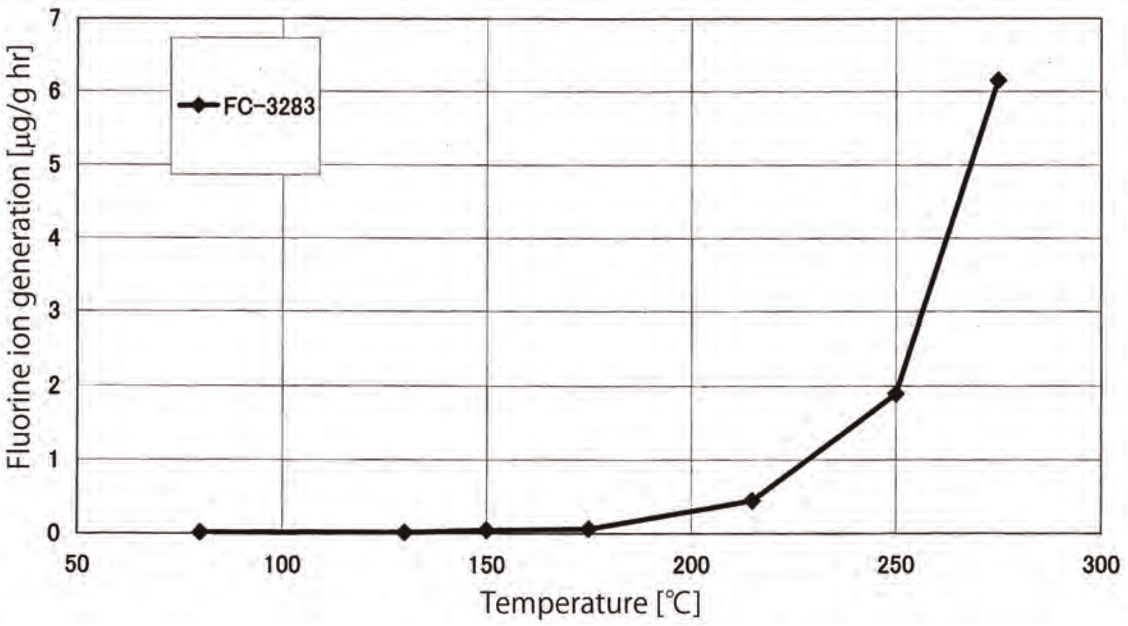

Figure 4.5: A temperature dependency of the ion decomposition rate of FT-3283[66]

4.5 Swelling test for G-10

G-10 is a material used for fabricating a flow channel. We put three small plates of G-10 into Fluorinert, and observed them for 5 months. Their appearances and textures did not change. As shown in Table **4.6**, no significant increment of masses were seen.

Table 4.6: A result of the swelling test

	Before test (18/12/2009)	After test (27/5/2010)	Difference of mass [g]
G-10 sample No. 1	41.98	41.98	0.00
G-10 sample No. 2	43.31	43.32	0.01
G-10 sample No. 3	43.27	43.28	0.01

4.6 Erosion test of the core

To examine appearance of erosion on the surfaces of the core, which is expected in a flowing fluid, the surfaces of the core whose outer diameter was 200 mm were exposed to flowing Fluorinert. The velocity of the flow was over 0.7 m/s (∼4 m/s at an inlet). A strainer was checked 14 days after from the start of the operation. Some small pieces of FINEMET were seen, which were considered to have initially existed on the surface or between FINEMET layers. One small piece was seen 33 days after. Its diameter was 0.2~0.3 mm. Operation was continued, however, no piece was observed. The total operation time was two months. The surface of the core was observed by bare eyes and microscope (magnification: 25-175). No defect was seen.

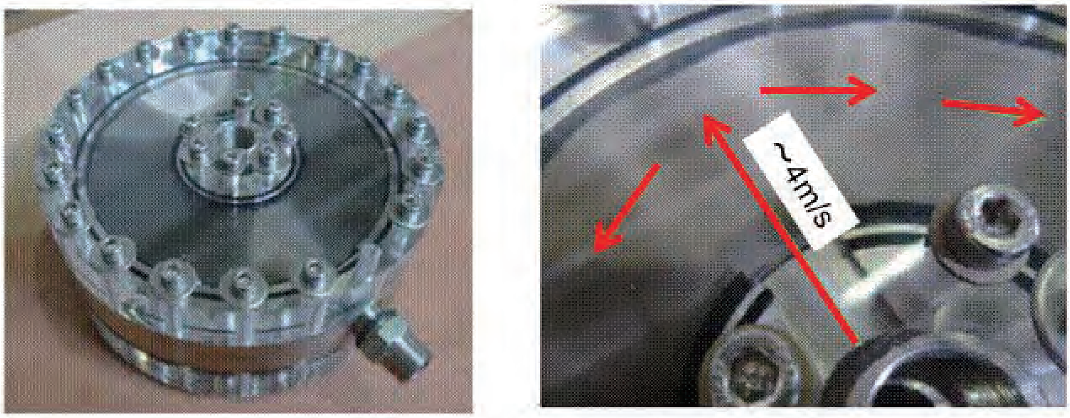

Figure 4.6: An experimental apparatus for the erosion test

4.7 RF designing for the new cavity

The new cavity was designed and its resonance frequency is determined to be ω_0. ω_0 is determined by the inductance L and capacitance C of the prototype cavity. C (the capacitance of the accelerating gap) was determined in the designing, because L was fixed by the sizes of cores. HFSS (High-Frequency Structure Simulator) which is a product of ANSYS, Inc. was used for the RF designing. Three issues were simulated.

- The value of the gap capacitance which is obtained by tuning the resonance frequency to 1.7 MHz
- The heat distribution in the cores
- The voltage on the core surfaces

Properties of the core such as relative permittivity or permeability are not isotropic because of the layered structure of the core. To introduce them to the simulation with HFSS, we assumed as following. According to Appendix A, a capacitive transmission of a signal is dominant over 76 kHz. That means the core is possible to be expressed as a combination of a lot of cylinders whose diameters are different each other. A schematic view is shown in Figure **4.7**. The operational frequency of the test cavity is 1.7 MHz which is enough larger than 76 kHz. Then, in more macroscopic view, it is able to be expressed as a bulk which has anisotropic permittivity and permeability in cylindrical coordinate system. However, HFSS does not have a function to represent anisotropy in cylindrical coordinate system. We adopted a method which is introduced below.

Each core are circumferentially separated 60 parts. Their angles are equally 6°. HFSS is able to define local coordinate systems. As shown in Figure **4.8**, local coordinate systems drawn in red are defined at each separated part. Relative permittivity and permeability which are orthogonally anisotropic are defined in them. This procedure has a same effect as defining anisotropy in cylindrical coordinate system. The anisotropy becomes more accurate in a finer separation, however, circumferential separation of 60 was selected to reduce a time for calculating. Properties of orthogonal anisotropy which are defined in the local coordinate systems are shown in Table **4.7**. A method to obtain these values are introduced in following subsections.

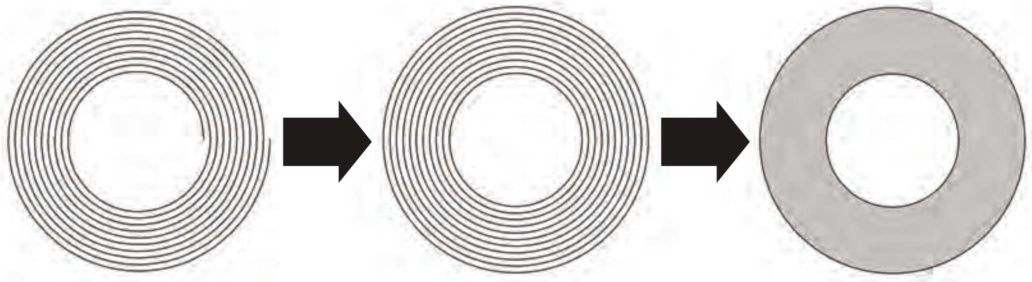

Figure 4.7: A macroscopic treatment for the core model

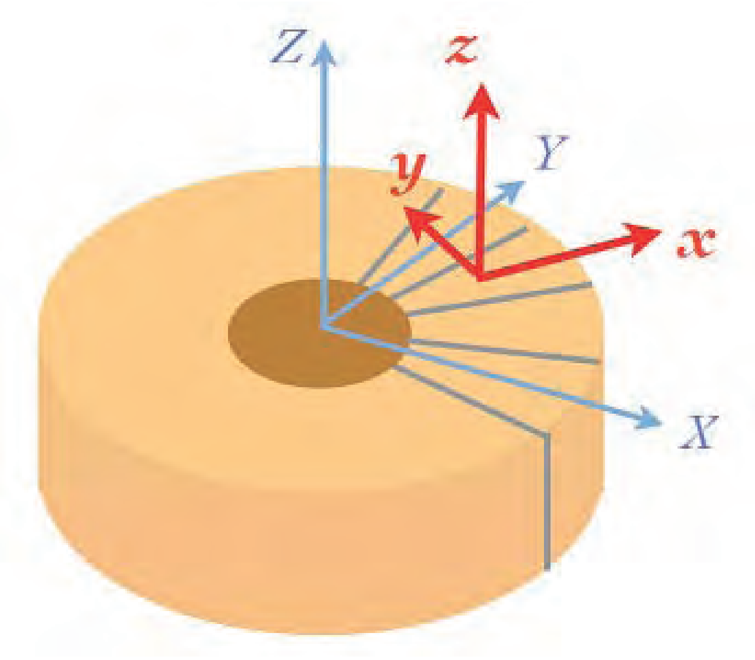

Figure 4.8: Definitions of local coordinate systems[67]

Table 4.7: Anisotropic properties defined at each local coordinate system

	Relative permittivity	Relative permeability
X direction	15	4
Y direction	1	3500
Z direction	1	3500

Relative permittivity in radial direction

As shown in Figure **3.9**, the core has a structure that FINEMET ribbon and silica are laminated alternately. Microscopically, the layered structure is a capacitor whose distance of two electrodes is h [m] and the area of the electrode is S [m^2]. The capacitance of the capacitor, C [F], can be written as

$$C = \epsilon\epsilon_0 \frac{S(a+b)}{bh}, \tag{4.2}$$

where a=18[μm] and b=2[μm]. They are thicknesses of a FINEMET ribbon and silica, respectively. ϵ=2 is a relative permittivity of silica. We treated this layered structure in macroscopic way. We assumed the structure has a effective relative premittivity ϵ_{eff}. Then, a capacitance C$_{eff}$ can be expressed as

$$C_{eff} = \epsilon_{eff}\epsilon_0 \frac{S}{h}. \tag{4.3}$$

Assuming these two capacitance are consistent, $\epsilon_{eff} \sim 20$ is derived. Considering the filling ratio of the FINEMET core is 75 % , $\epsilon_{eff} \sim 15$.

Relative permittivity in circumferential and beam directions

Relative permittivities in these directions are considered to be infinite, because these directions are along conductive FINEMET layers. Results of the calculation with relative permittivities of 9999 in these directions showed that higher order modes appeared, which should not appear in reality. 9999 is the maximum value which is able to be input into HFSS. This is because a wavelength in the cores was shorten by the large relative permittivity. In a real condition, layered FINEMET ribbons are expected to force the direction of an electric field to be along a radial direction. To represent this condition, some layers of perfect-electric-conductor are concentrically assembled in the core model. Electric fields only exist along a radial direction, so that the relative permittivities in circumferential and beam directions are arbitrary. "1" was used as the relative permittivity in these directions.

In the case of the new cavity, radial thickness of the core is thin, so that the directions of electric fields are along radial direction naturally. Hence, no perfect electric conductive layer is assembled and the relative permittivity is "1".

Relative permeability in a radial direction

The relative permeability of simple FINEMET and the insulating layer (the impregnated epoxy resin) are 1900 and 1, respectively at 1.7 MHz. Treating the layered structure macroscopically, an effective relative permeability can be written as

$$\frac{75+25}{\mu_{eff}} = \frac{75}{1900} + \frac{25}{1}. \tag{4.4}$$

Hence, a following result is deduced.

$$\mu_{eff} = \frac{(75+25)\cdot 1900}{75\cdot 1 + 25\cdot 1900} = 4 \tag{4.5}$$

Where, 75 and 25 represent filling ratios of FINEMET and the insulating layer, respectively.

Relative permeability in circumferential and beam directions

These directions are along FINEMET layers. Therefore, relative permeabilities of 1400 are derived by multiplying a filling ratio of 75% to the relative permeability of simple FINEMET. According to Appendix G, μ'_p must be used in no loss calculation, and is calculated as 3500 in the present case.

4.7.1 Simulations for electromagnetic fields

Using relative permittivity and permeability derived above, we performed calculations for the eigen mode with HFSS. A resonance frequency of the prototype cavity was tuned to

1.7 MHz by adjusting a permittivity of the accelerating gap. The result showed optimum capacitance of the gap was 660 pF. The accelerating gap of the actual cavity will be made of alumina, however, variable capacitor is connected for the prototype cavity instead of the alumina gap. Distributions of the electric field along the beam axis and magnetic-flux-density in the core, which are normalized with the power loss of a presently installed RCS core (6 kW), are shown in Figure **4.9** and **4.10**, respectively. A distribution of the heat in the core is proportional to the squared distribution of magnetic-flux-density in the core, and is shown in Figure **4.11**. A distribution of electric fields on lines which are shown in Figure **4.12** are shown in Figure **4.13**. Properties of each material used in this simulation are shown in Table **4.8**. All of them are lower than the breakdown voltage of Fluorinert ~40 [kV] per 2.54 [mm], so that no breakdown is expected.

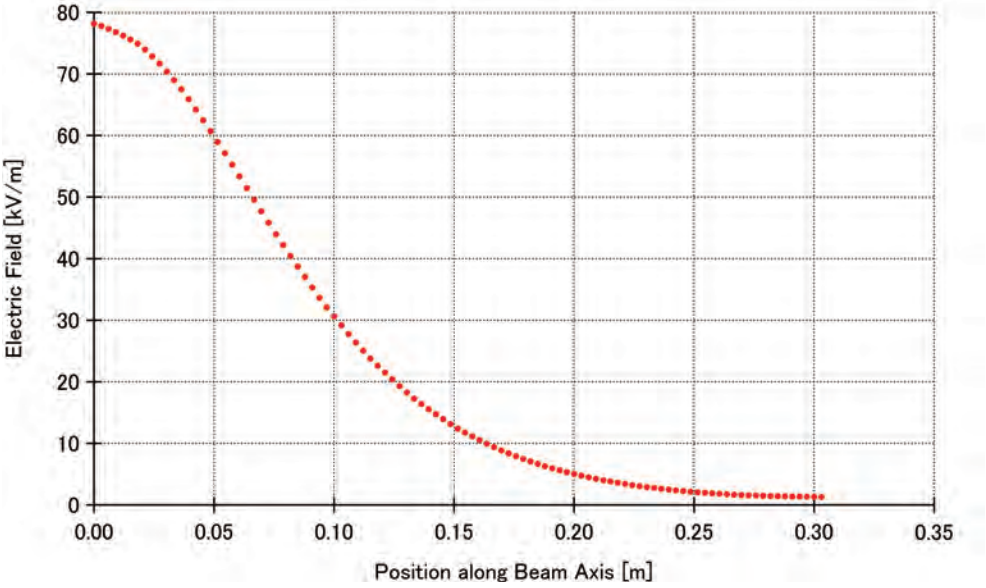

Figure 4.9: A distribution of an electric field along the beam axis, which was derived from the simulation

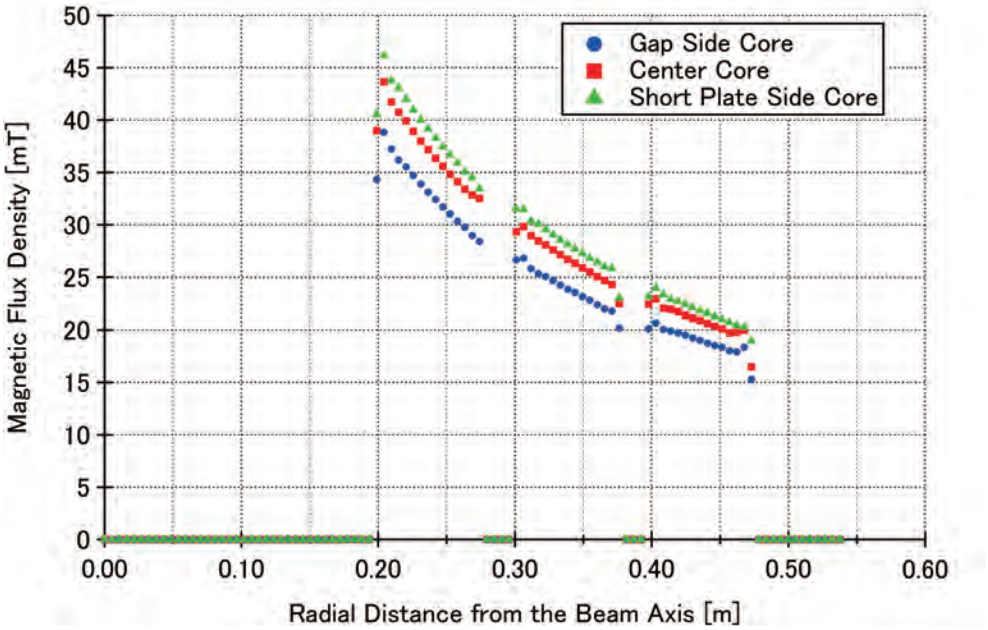

Figure 4.10: A distribution of magnetic fields in the cores, which were derived from the simulation. A blue circle, red rectangular, and green triangle represent the magnetic-flux-densities in the gap side core, center core, and short plate side core, respectively.

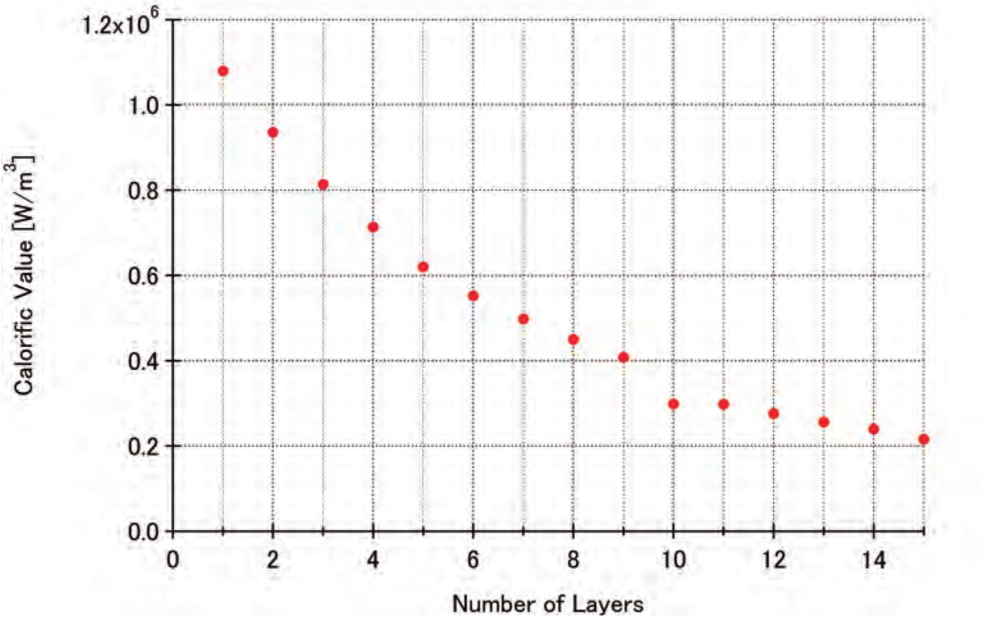

Figure 4.11: A distribution of a calorific value in the cores, which is proportional to the squared distribution of magnetic-flux-density in Figure **4.10**

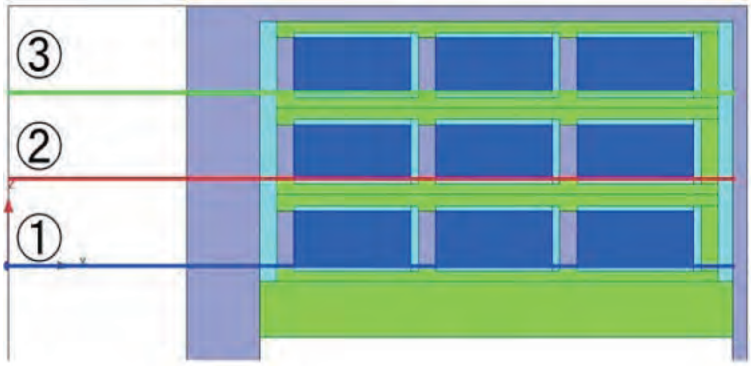

Figure 4.12: Lines where electric fields on the core surfaces are calculated[58]

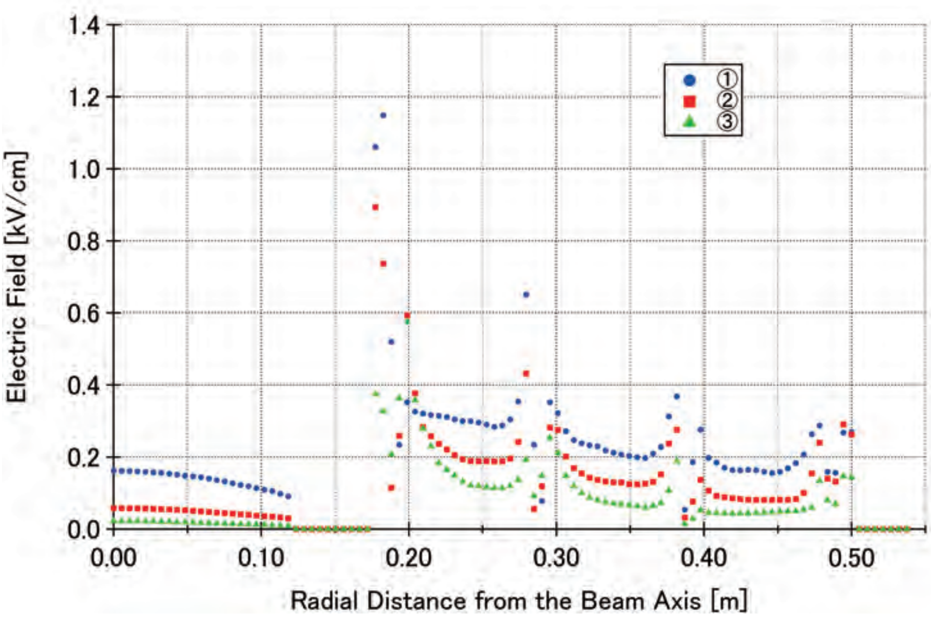

Figure 4.13: Electric fields on the lines which are shown in Figure **4.12**

Table 4.8: Electromagnetic properties of materials used in the simulation

	Relative permittivity	Relative permeability
FINEMET core	radial: 15 circumferential: 1 beam direction: 1	radial: 4 circumferential: 3500 beam direction: 3500
Fluorinert	1.91	1
G-10	4.5	1
Alumina	38	1

4.7.2 Thermo-fluid simulation, and design for the flow channel with a half sized flow channel

A flow channel is formed on the surface of the cores to make the flow turbulent by increasing the velocity of Fluorinert, and enhance the cooling efficiency. The apertures surrounded by the surfaces of the cores and G-10 plates in Figure **4.3** form flow channels (3mm hight × 81 mm width). A geometry of the flow channel is shown in Figure **4.14**. Fluorinert enters inner diameter and exits outer diameter. Reynolds number of over 2320 is necessary to make the flow turbulent. It corresponds to a velocity of over 0.33 m/s. In the flow channel, the flow rate of Fluorinert is set to approximately 45 L/min to gain a velocity of 0.7 m/s which is enough to realize the turbulence.

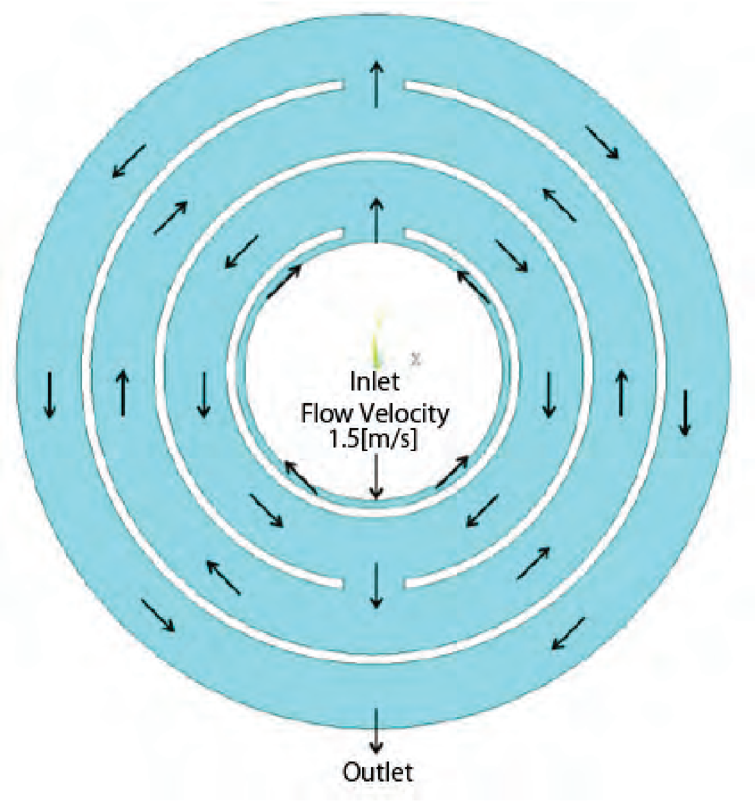

Figure 4.14: A schematic view of a flow channel

A distribution of the velocity calculated with ANSYS CFX is shown in the left-hand-side of Figure **4.15**. A velocity which is needed for a turbulence is seen in almost whole region of the flow channel. In the left-hand-side of Figure **4.16**, the upper limit of the contour is set to 0.4 m/s in order to help us to identify the area of turbulence. The red area represents turbulence.

Some stagnations are seen at connections between the flow channels with the different diameters. To evaluate the adequacy of the simulation, a half sized flow channel (1.5 mm height × 38 mm width) was fabricated and a visualization test for the flow was performed. The flow channel is shown in Figure **4.18**. Both sides of the container are made of a transparent acrylic-acid-resin to observe the flow. Dummy cores are made of aluminum and painted white to help the visualization. The fluid is water. Black ink is mixed into the fluid and the flow is visualized. Stagnations are seen at the same regions as the simulation. This result shows the simulation is reliable. At the beginning of the test, bubbles were trapped in the flow channel. They disappeared in an hour. The results of the test are shown in Table **4.9**.

Rudders made of G-10 are mounted and spout holes are fabricated to solve stagnations. These ideas are based on the design of an airplane. The rudders also have a function to keep the shape of the soft cores. Positions and geometries of the rudders are optimized with ANSYS CFX. An optimum geometry of the rudder and positions of them are shown in Figure **4.19** and **4.20**, respectively. Geometries and positions of the spout holes are also shown in Figure **4.20**.

The result of the simulation for the velocity of the Fluorinert after the optimization is shown in the right-hand-side of Figure **4.15**. The upper limit of the contour is set to 0.4 m/s in the right-hand-side of Figure **4.16**. The stagnations disappeared.

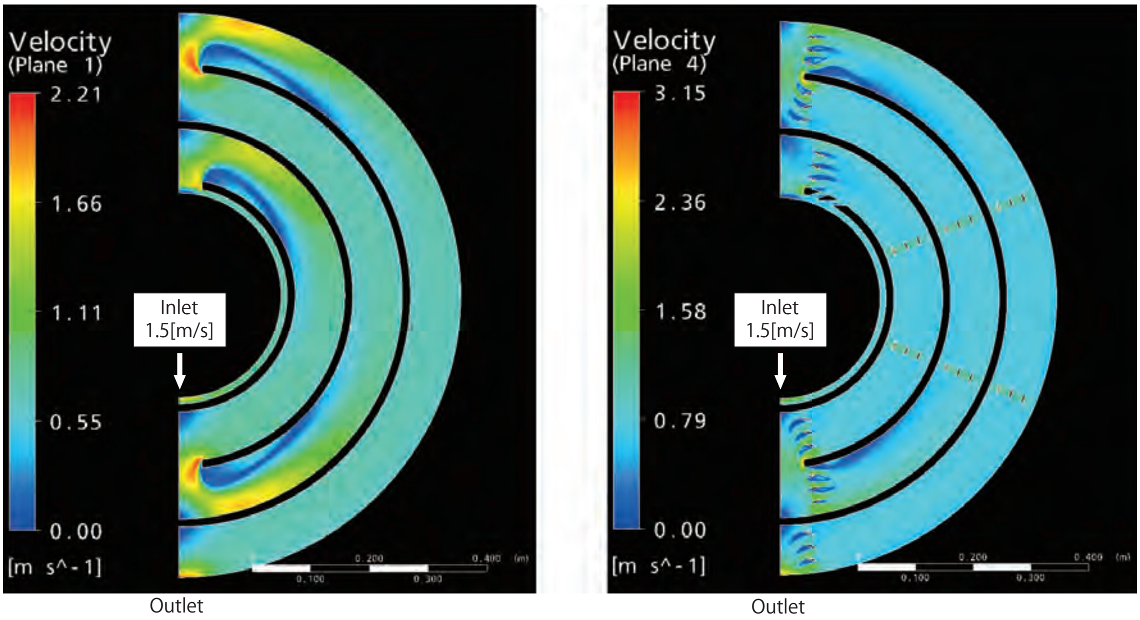

Figure 4.15: Distributions of Fluorinert velocity calculated by means of ANSYS CFX. Left-hand-side is the calculation before the optimization of the flow channel. Right-hand-side is after optimization.[58]

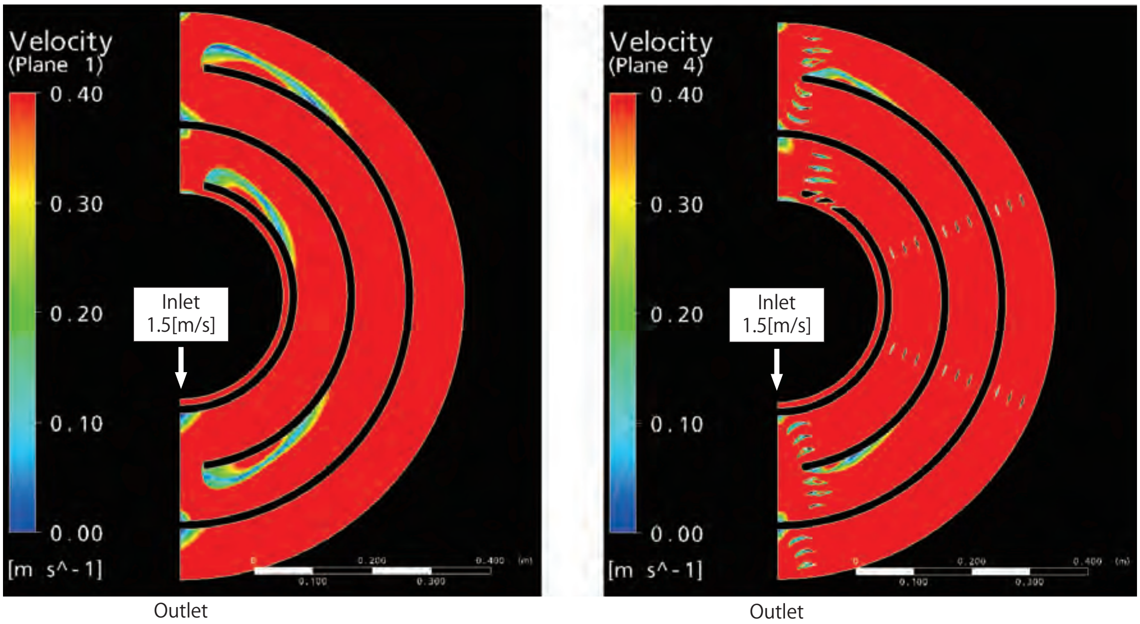

Figure 4.16: The upper limit of the contour in Figure **4.15** is changed to 0.4[m/s]. Fluorinert is turbulent over 0.33[m/s], so that red area represents turbulent flow.[58]

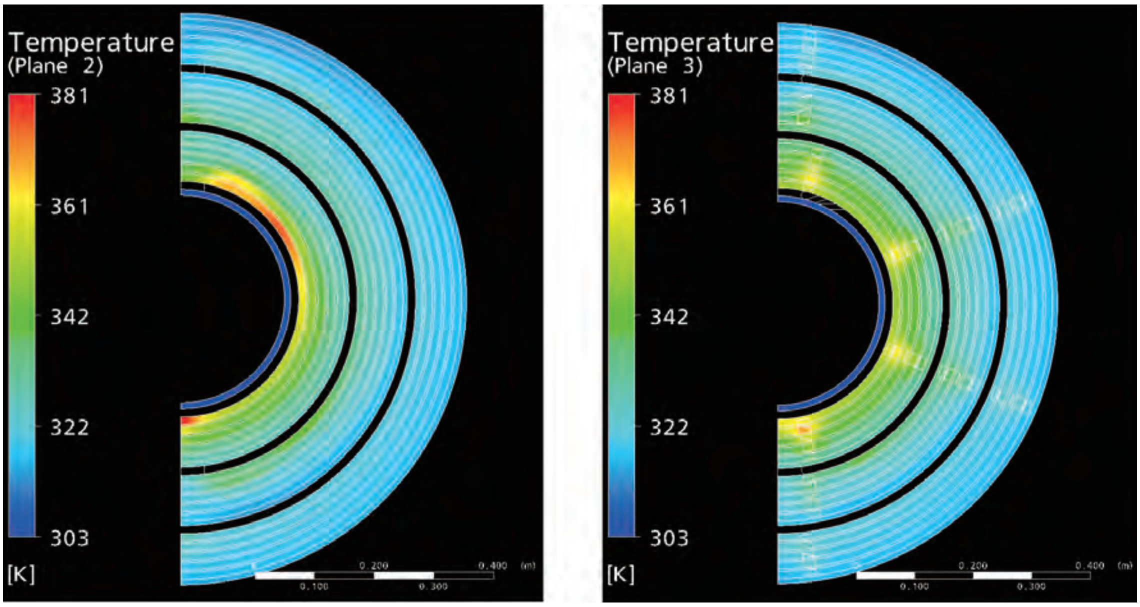

Figure 4.17: The distribution of the temperature at the center of the core. Left-hand-side is before the optimization of the flow channel. Right-hand-side is after optimization.[58]

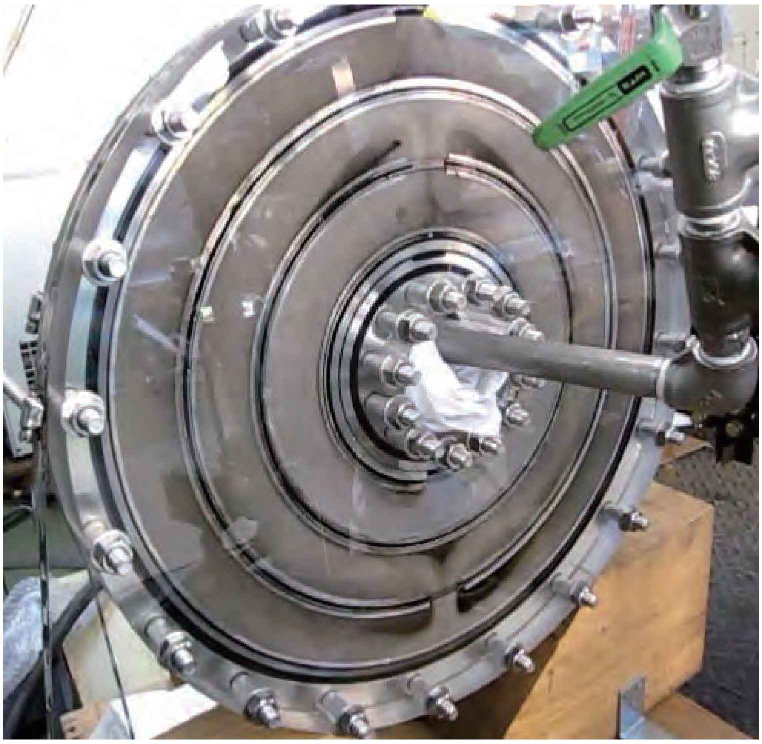

Figure 4.18: A half sized flow channel

Table 4.9: A result of the visualization test

Velocity [m/s]	Pressure [kgf/cm^2]	Laminar or Turbulence
0.73	0.2	Turbulence
1.0	0.3	Turbulence
1.4	0.5	Turbulence
1.8	0.9	Turbulence
2.2	1.4	Turbulence
2.6	1.8	Turbulence
2.9	2.6	Turbulence
3.3	3.2	Turbulence

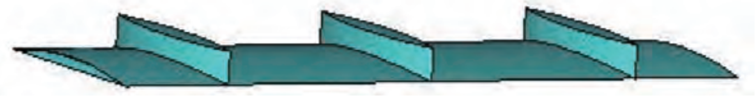

Figure 4.19: A schematic view of a rudder

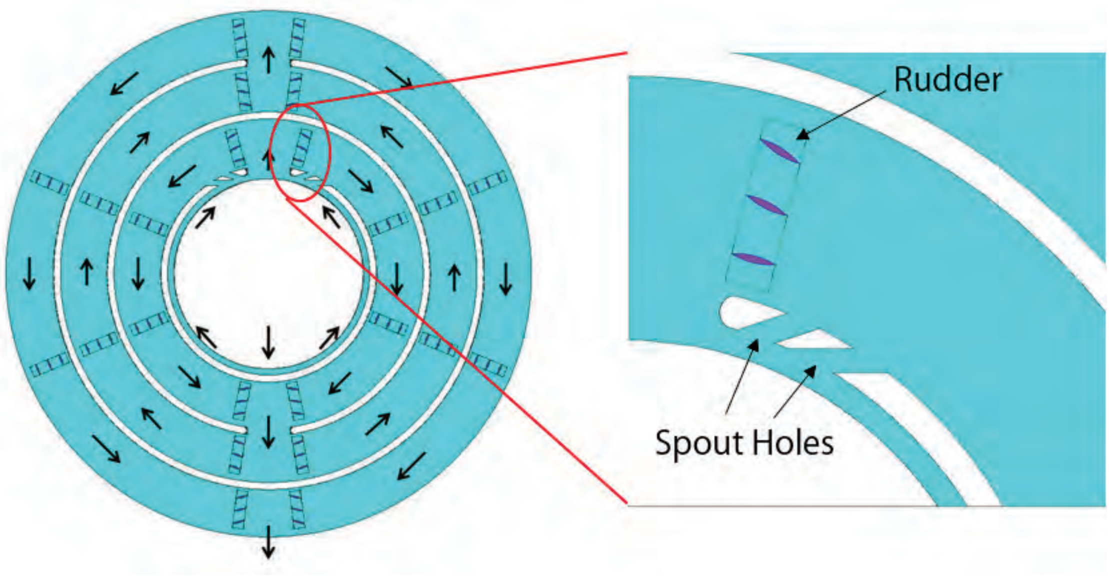

Figure 4.20: Positions of rudders and spout holes

4.8 Assembly of the prototype cavity

In this thesis, we introduce the development of the prototype cavity for the new cavity, which is loaded with one core module. The process of the assembly of the prototype cavity is given in this section.

4.8.1 Assembly of the core module

The core module was assembled by binding small, middle, large cores with two G-10 plates at a factory of Hitachi Metal, Inc. in Tottori. A picture of the assembly is shown in Figure **4.21**.

Results of the measurements for the shunt impedances of small, middle, large cores, and a core module are shown in Figure **4.22** and Table **4.10**. The shunt impedance of the core module is less than the sum of 3 different diameter cores by approximately 6% . We guess this is the systematic error which comes from the difference of the circumstances.

Screws are made of G-10. EPDM rubber is selected as a sealant. EPDM rubber is suited to Fluorinert and it has an excellent durability against radioactivity[61]. EPDM rubbers are attached on the surface of the rudders not to damage the cores by the direct contacts between the rudders and the cores. Because of this attachment, we modified the height of the flow channel from 3 [mm] to 5 [mm].

Figure 4.21: A core module under fabrication

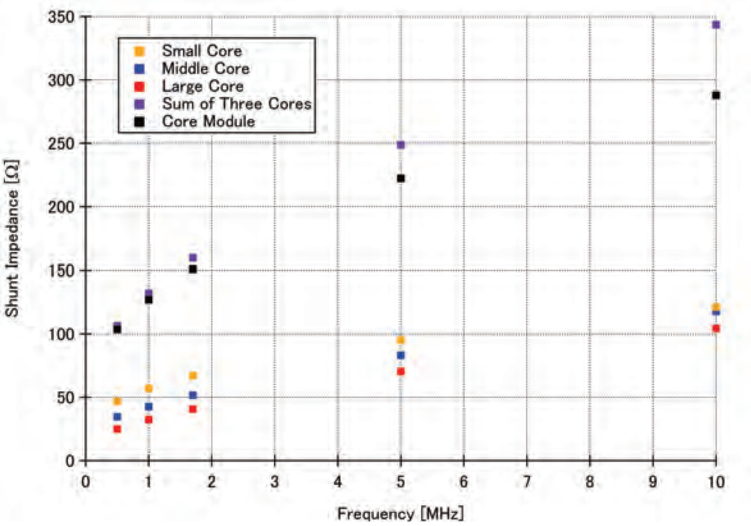

Figure 4.22: Shunt impedances of the three cores and the core module

Table 4.10: Shunt impedances of the three cores and the core module at 1.7 MHz

Large core	Middle core	Small core	Sum of three values	Core module
41Ω	52Ω	67Ω	160Ω	151Ω

4.8.2 Assembly of the prototype cavity

The prototype cavity was assembled in July, 2010. As shown in Figure **4.23**, the core module was assembled into a container made of stainless, then, we stood it up. Initially, we examine the airtightness of the container with nitrogen gas of 2 [atm], then, poured Fluorinert. This is because pouring expensive Fluorinert without an advance examination is risky. We selected a brass as the material for plugs and connectors. Use of a material which is different from container prevents plugs and connectors from being locked after assembly. Brass plugs and connectors are not corroded in Fluorinert and they are easily available.

Figure 4.23: An assembly of the prototype cavity

4.9 RF test facility

4.9.1 RF source

A semiconductor RF source shown in Figure **4.24** is used. Output power (continuous wave): 0-10 kW, output frequency: 800 kHz-3 MHz, output impedance: 50Ω (LC connector).

Figure 4.24: A semiconductor RF source

4.9.2 Cooling system

A schematic view of a cooling system is shown in Figure **4.25**. The magnetic pump is used. The pump often slipped in the early operation, because the density of Fluorinert is approximately twice as large as that of water, and the pump was designed for water. We solved this problem by attaching a weight on the shaft of the motor in order to perform a dynamic matching. The heat exchanger has the ability to cool 100 kW. Pure water of approximately 30°C flows in the secondary cooling system. The independent circulatory system is connected to the cooling system, which has filters for water, organic substances, and acid generated by radiations on Fluorinert.

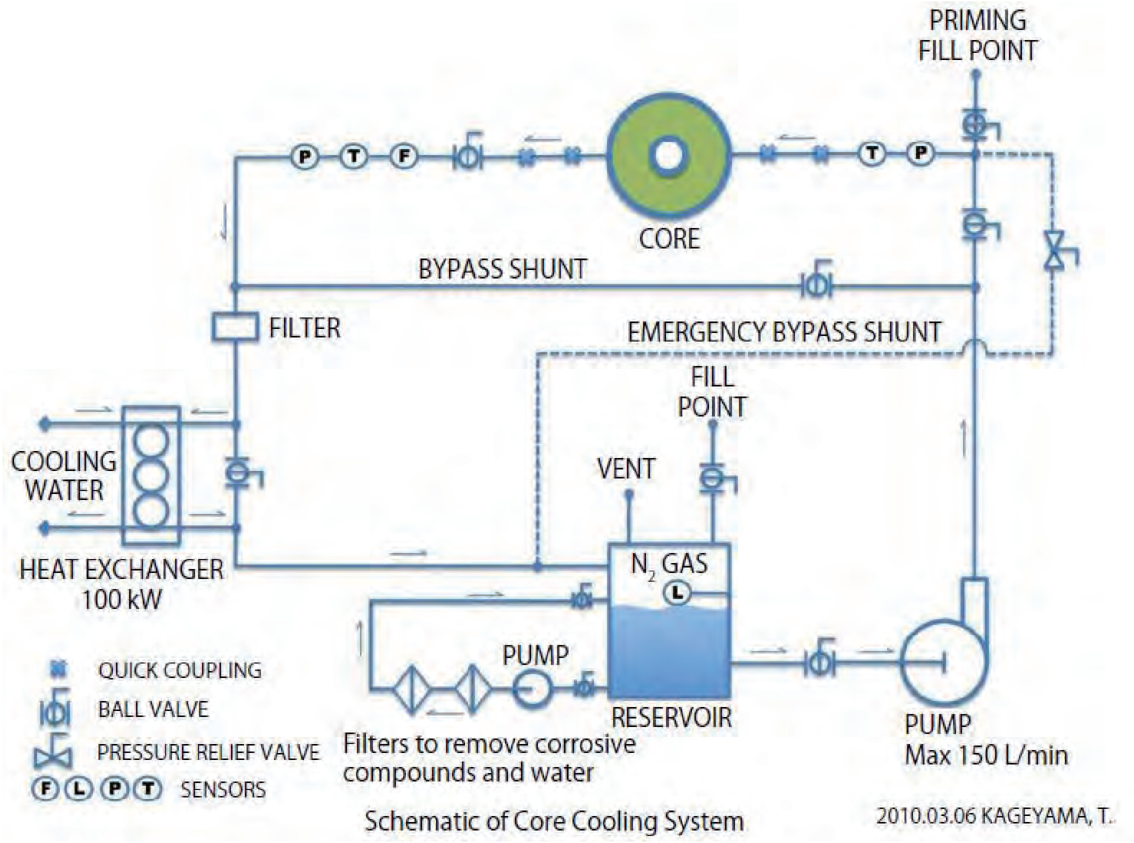

Figure 4.25: A conceptual diagram of the cooling system[67]

4.9.3 Matching box

On resonance, the impedance of the prototype cavity seen from the RF source is a pure resistance. The value was directly measured as 146 Ω. As shown in Figure **4.26**, the pure resistance of 146 Ω is on the horizontal axis of the immittance chart, so that two ways are available to match with the output impedance of the RF source (50 Ω). They are paths passing upper region and downer region on the immittance chart. Diagrams of them are shown in Figure **4.27** and **4.28**. The capacitor is connected in series in Figure **4.27**. The inductor is connected in series in Figure **4.28**. The connection in Figure **4.28** is accepted, because a large current of 20 A flows in the series wire and an inductor is stronger against a current than a capacitor. The capacitor has 890 pF and the inductor has 6.6 μH in Figure **4.28**. The circuit is shown in Figure **4.29**. After assembling the matching box, VSWR was improved from 2.7 to 1.1.

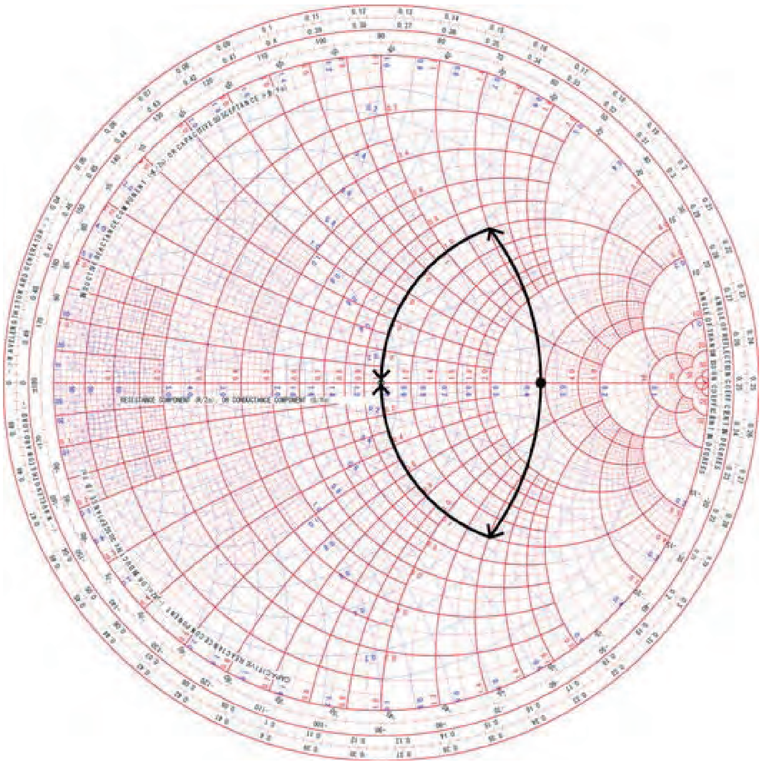

Figure 4.26: Impedance matching with the immittance chart

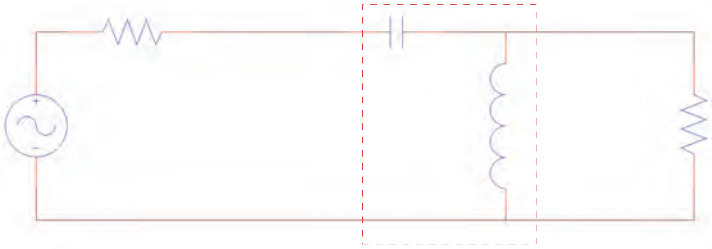

Figure 4.27: A circuit schematic of the matching box with the series capacitance

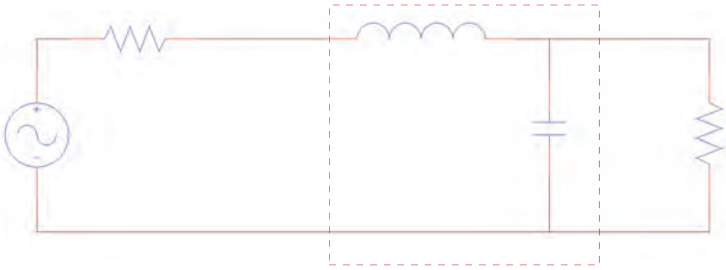

Figure 4.28: A circuit schematic of the matching box with the series inductance

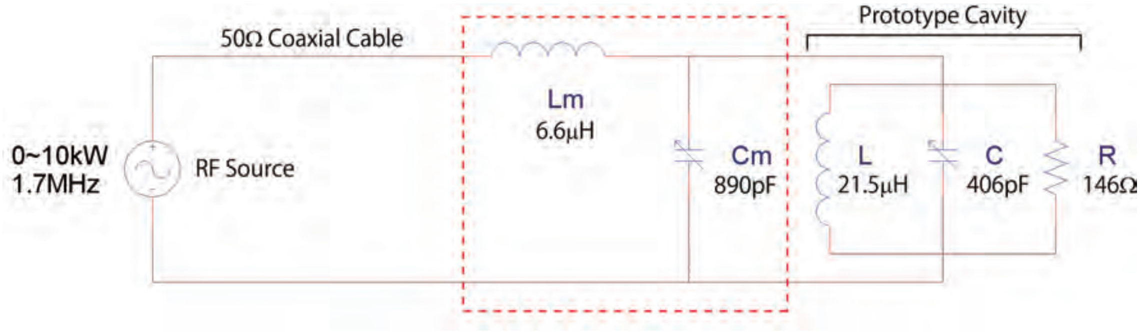

Figure 4.29: A circuit schematic of the matching box used in the RF test

4.9.4 Interlock system

We set up an interlock system for the test facility. We connected two outputs of DC currents on the control panel of the cooling system and the paperless-pen-recorder. Each output is for monitoring the flow rate and the Fluorinert temperature at the inlet. External relays of the paperless-pen-recorder is adjusted to be open under 34[L/min] for the flow rate or over 70[°C] for the inlet temperature. These relays are connected to the RF source. Therefore, the RF source is turned off on the condition of these states.

Chapter 5

RF test

This chapter reports the results of RF test. The temperature rise of Fluorinert, the resonance frequency, the shunt impedance, and Q value were measured. The cooling efficiency was evaluated.

5.1 Test stand

RF test was performed at D7 RF experimental hall in KEK. The completed prototype cavity with the matching box is shown in left of Figure **5.1**. We adjusted the capacitance of the variable capacitor over checking the impedance of the cavity with the LCR meter, and tuned the resonance frequency to 1.7 MHz. The capacitance was fixed as 406 pF. While the RF source is on, the prototype cavity and the matching box were covered with an aluminum shelter shown in right of Figure **5.1** to confine an electromagnetic wave.

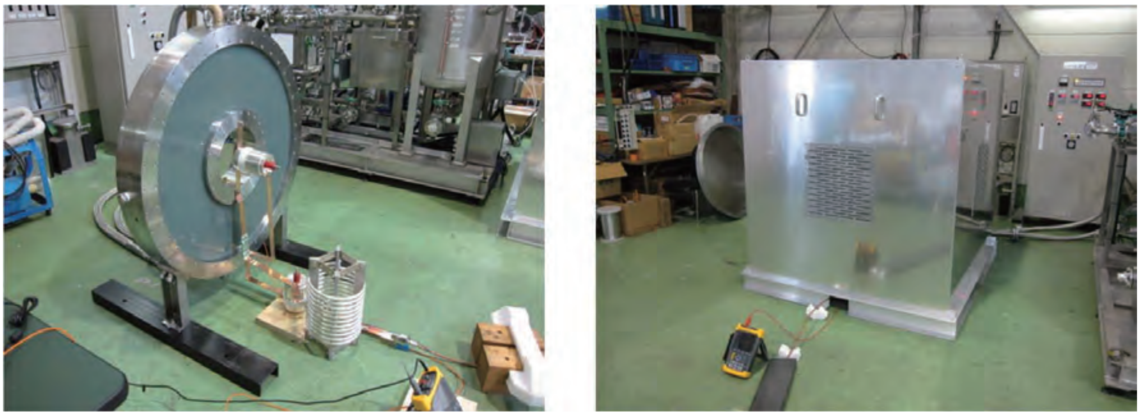

Figure 5.1: (Left) The completed prototype cavity with the matching box. (Right) The aluminum shelter to confine the electromagnetic wave

5.2 Measurement of temperature rise of Fluorinert

A temperature rise of Fluorinert (a flow rate: 80[L/min]) was measured on the condition that RF power of 0-10 kW (1.7 MHz) were provided to the prototype cavity. P, L, ρ, and C are defined as a dissipated power in the cores, a flow rate, a density of Fluorinert, and a specific heat of Fluorinert, respectively. Then, the temperature rise of Fluorinert can be written as

$$\Delta T[\mathrm{K}] = \frac{P[\mathrm{W}]}{L[\mathrm{m}^3/\mathrm{s}] \times \rho[\mathrm{kg/m}^3] \times C[\mathrm{J/kg/K}]}. \tag{5.1}$$

The comparison between the measurement and the calculation of the temperature rise is shown in Figure **5.2**. Red and blue circles represent the measurement and the calculation, respectively. The density of 1792[kg/m^3] and the specific heat of 1068[J/kg/K] which correspond to the values at 35°C were used for the calculation. They reflect the temperature of Fluorinert at inlet of 34°C. P includes the correction of the cable loss. The loss is 0.0054[dB/m]. The length of the cable is 7[m]. Hence, The loss for one way is derived as

$$0.0054[\mathrm{dB/m}] \times 7[\mathrm{m}] = 0.038[\mathrm{dB}]. \tag{5.2}$$

Namely, the loss for one way is 0.88% . The plot shows the measurement and the calculation have a good agreement, so that we are able to conclude the powers are supplied correctly.

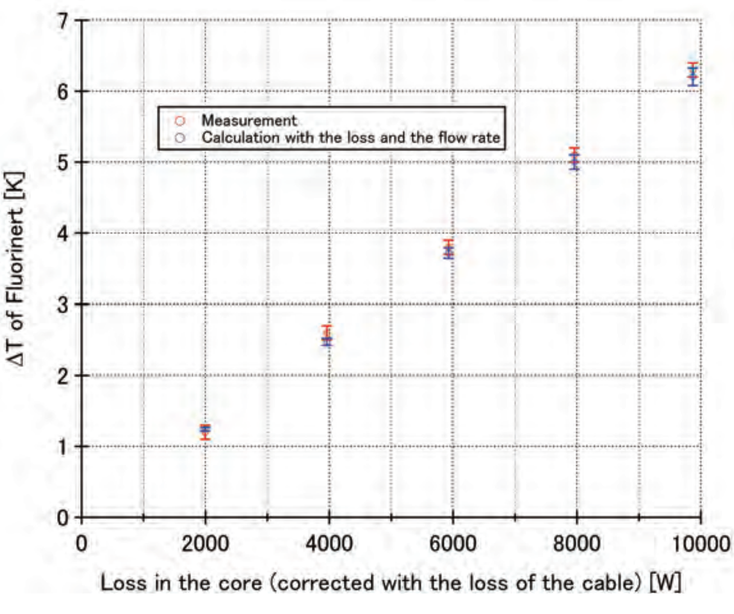

Figure 5.2: A relation between the temperature rise of Fluorinert and the dissipated power in the cavity. Red and blue circles represent the measurement and the calculation, respectively.

5.3 Measurement of the shunt impedance

Using values of voltages on the accelerating gap (the variable capacitor) and dissipated powers in the cores, shunt impedances were calculated and are shown in Figure **5.3**. The definition of the shunt impedance shown below was used.

$$R_p \equiv \frac{V^2}{2P} \tag{5.3}$$

Where, R_p is a shunt impedance, V is an accelerating voltage, and P is a dissipated power in the cores. The shunt impedances in Figure **5.3** are steady at any dissipated powers, so that we are able to conclude no unusual heating and no discharge appear.

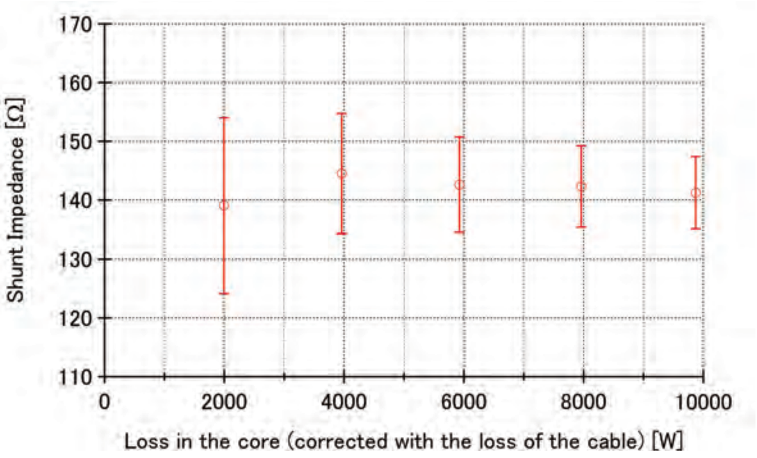

Figure 5.3: A relation between shunt impedances of the cavity and dissipated powers in the cores

5.4 Q factor of the prototype cavity

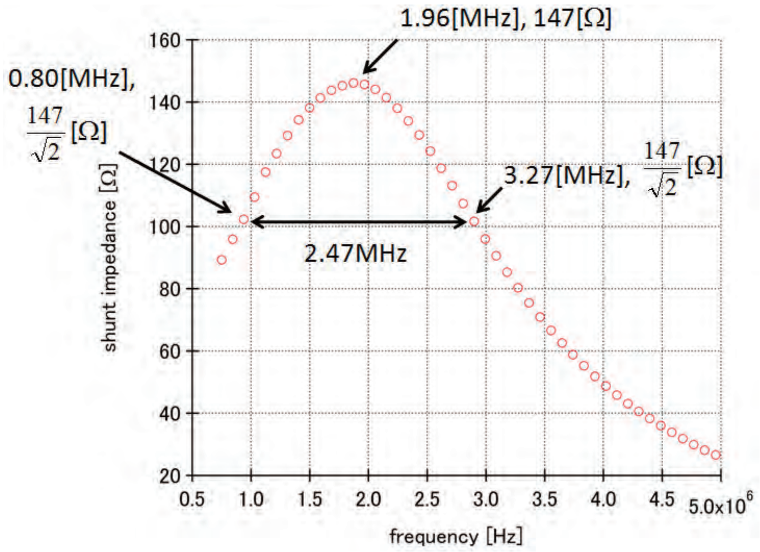

Figure 5.4: A shunt impedance of the prototype cavity which has a resonance at 1.7[MHz]

A result of measurement for the shunt impedance of the cavity around its resonance point is shown in Figure **5.4**. The Q factor of the cavity can be derived with the definition.

$$Q \equiv \frac{f_0}{\Delta f} \tag{5.4}$$

Where, f_0 is the frequency at the point where the shunt impedance is on the peak, and Δf is the band width between two points where the values of the shunt impedances are $1/\sqrt{2}$ of the peak. Hence, the Q factor is derived as

$$Q = \frac{1.96 \times 10^6}{2.47 \times 10^6} = 0.8. \tag{5.5}$$

The Q factor of the presently installed cavity is ∼2. This value is realized by connecting a parallel inductor to the cavity. The original Q of the presently installed cavity is 0.6. The Q of the prototype cavity is consistent to that of the presently installed cavity within 25% , and can be tuned to ∼2 by the same scheme.

5.5 Cooling efficiency of the prototype cavity

5.5.1 Measurement of temperatures on the surfaces of the cores with a thermo paint

We measured temperatures on the surfaces of the cores with a thermo paint. It is a product of Nichiyu Giken Kogyo Co., Ltd.. The product number is No.5. The range of the temperature where the color of the thermo paint changes was measured on a hotplate. The initial color of light pink began to change to blue at 47°C. Then, it gradually turned deeper blue as the temperature rises. The end of the change was at 55°C. We painted it on the surfaces of small, middle, and large cores. Positions where we painted are shown in Figure **5.5**. At these positions, sapphire view ports are assembled to observe the colors. The view ports are shown in Figure **5.6**.

We supplied powers to the cavity up to 8[kW] by 1[kW] step. In the equilibrium condition at each step, we turned off the RF source and removed the panel of the shelter, then, checked the colors by the bare eyes. The color was only changed on the small core. No change was observed on the middle and large cores. A result for the small core is shown in Figure **5.7**. The green area is the region where the color is supposed to vary. The color began to change in the observation at 4[kW], and ended at 7[kW]. These values are shown with red lines. The blue line represents the temperature of the surface of the small core, which were obtained from the simulation. The blue line is expected to diagonally cross two vertexes of the rectangular consisted with the green area and the two red lines, when the measurement and the simulation are consistent. The thermo paint have the error of approximately ±10°C, so that we are able to conclude they have a good agreement.

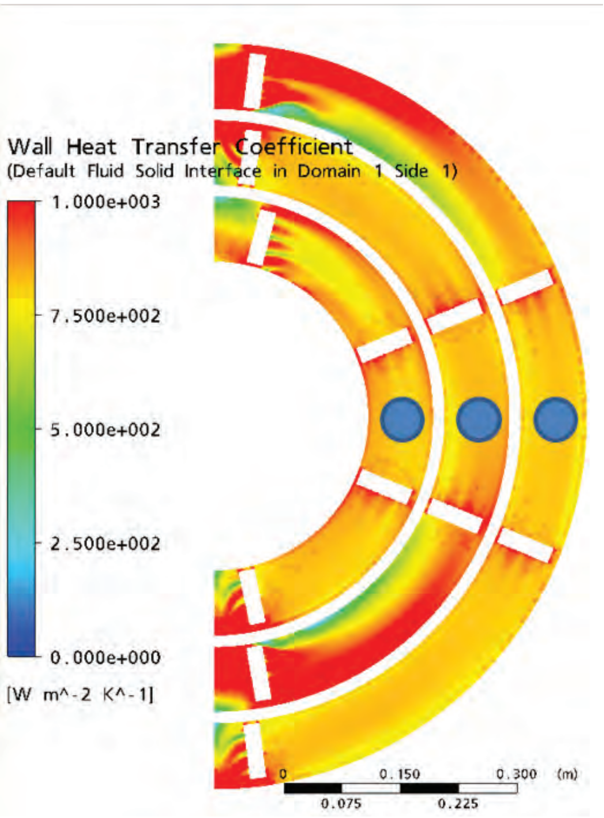

Figure 5.5: Blue circles are the positions where the thermo paint is painted.

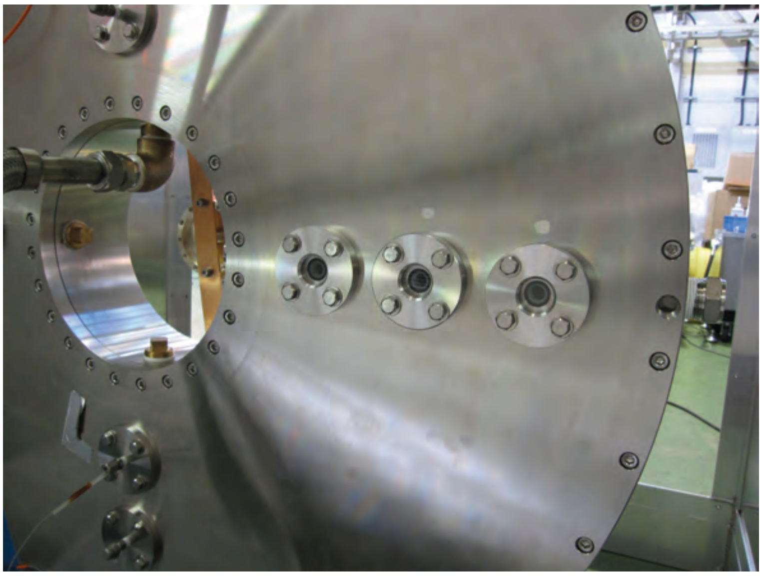

Figure 5.6: Sapphire view ports to observe the color of the thermo paint

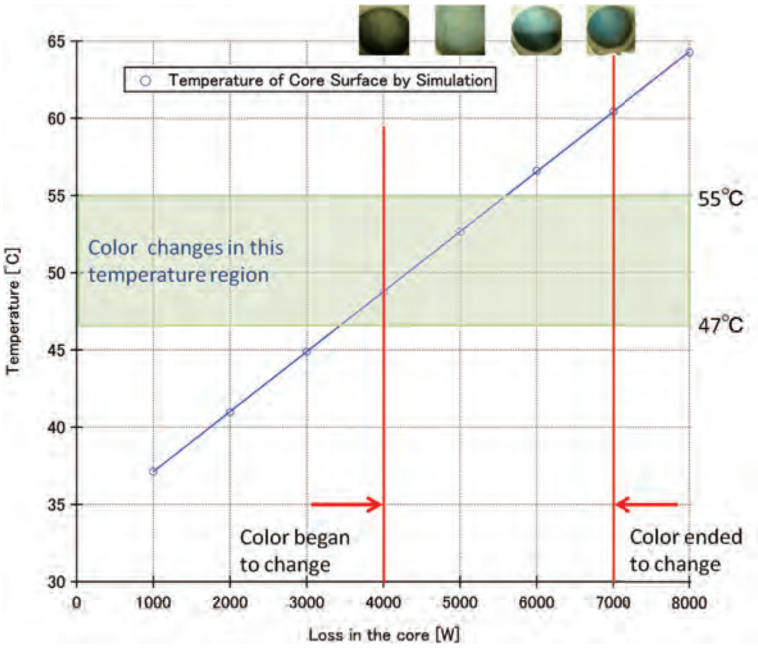

Figure 5.7: A result of the measurement for the temperature on the surface of the small core

5.5.2 Evaluation of a heat transfer coefficient on the surface of the core

A heat transfer coefficient is obtained by measuring the time constant of the temperature decrement of Fluorinert after sudden off of the RF source which is supplying a power in continuous operation. The heat transfer coefficient which is obtained with this method is expressed as the series connection of the heat transfer in the core and that on the surface of the core.

$$\frac{1}{h_{eff}} = \frac{1}{h_C} + \frac{1}{h} \tag{5.6}$$

Where, h_C is the heat transfer coefficient in the core, h is the heat transfer coefficient on the surface of the core, h_{eff} is the effective heat transfer coefficient. The heat transfer coefficient obtained with the time constant is h_{eff}. We measured time constants in various flow rates. On the other hand, time constants in the same conditions are figured out with simulations. Results are shown in Figure **5.8**. Then, heat transfer coefficients are calculated with these time constants and plotted in Figure **5.9**. The used formula is shown in Appendix H. The measurements and the simulations are consistent in 20% .

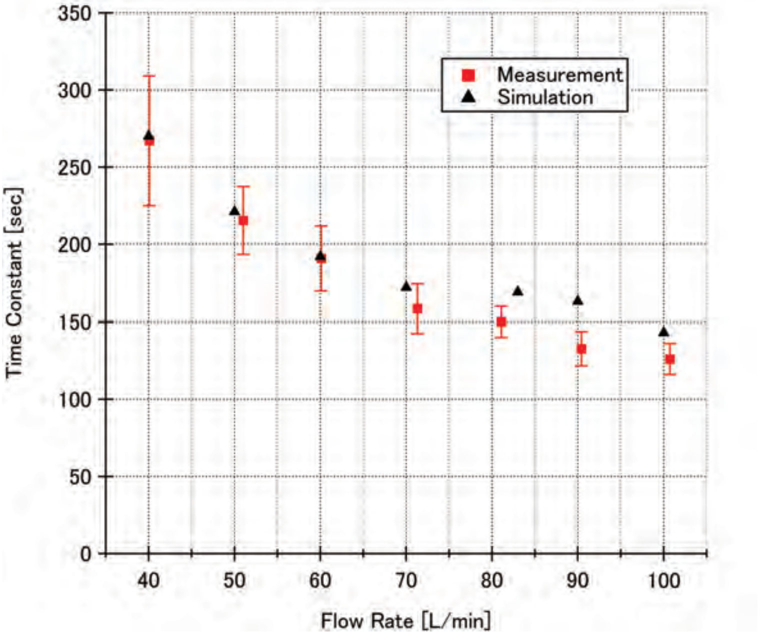

Figure 5.8: Results of the measurements for the time constants and results of the simulation

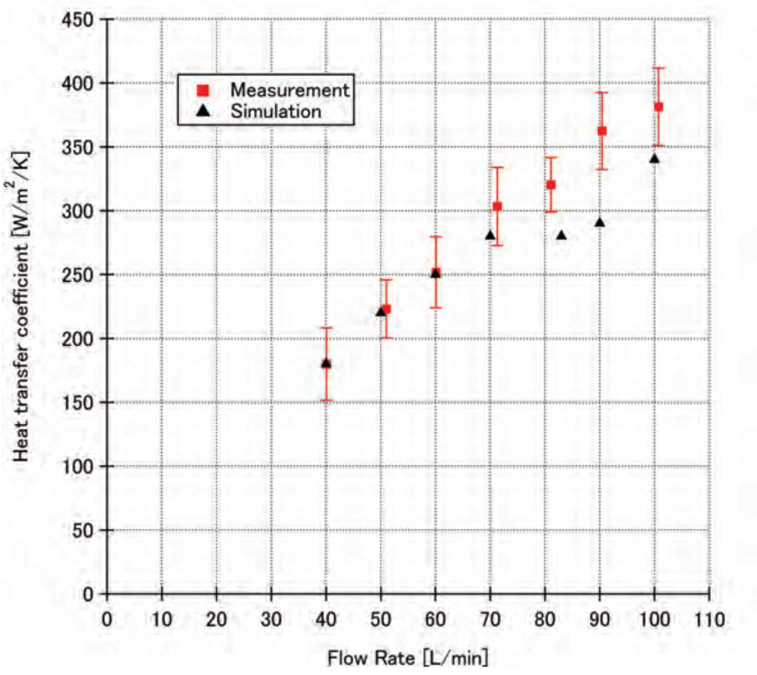

Figure 5.9: Heat transfer coefficients derived with the time constants

Above results support the reliability of the simulation. The essential heat transfer coefficient is h, because it characterizes the direct cooling efficiency of Fluorinert. h is directly obtained from the simulation. The values of h at the position of the blue circle on the small core in Figure **5.5** is shown in Figure **5.10**. h in the region over 60[L/min] surpass that of the presently installed RCS cavity (500[W/m^2/K]). Thus, we are able to conclude the prototype cavity has the enough cooling efficiency.

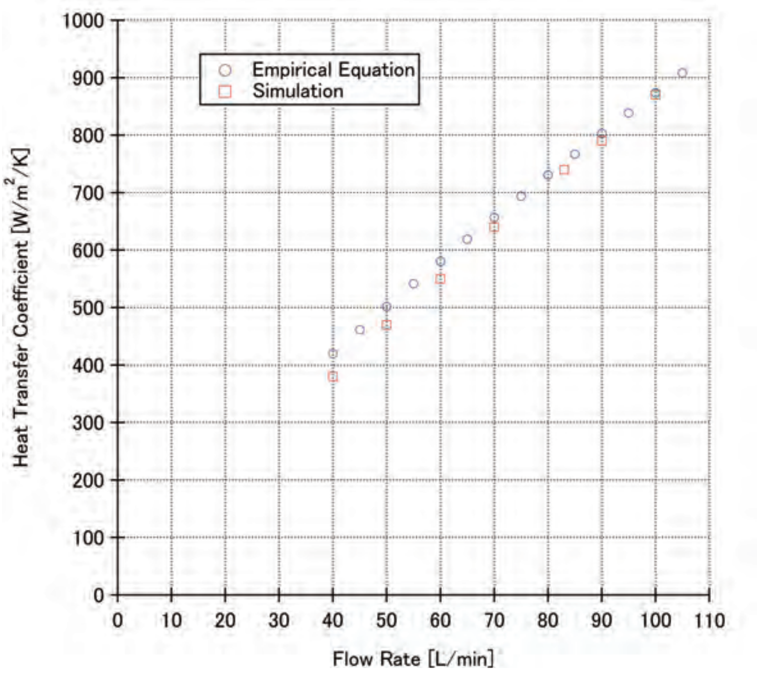

Figure 5.10: Results of the simulation for heat transfer coefficients

Chapter 6

Summary of performance of the prototype cavity and Discussion

J-PARC will produce the world's most intensive proton beam and provide it to advanced research facilities for variety of fields. However, a buckling problem of FINEMET cores in RCS appeared and a stable operation has not established yet. Despite this situation, we plan to enhance the present intensity of the beam. We are developing a new accelerating cavity which can be replaced with a presently installed RCS cavity to contribute to the stabilization and enhancement for the performance of J-PARC accelerator.

For this purpose, we carried out experiments listed below.

° **Calculation of the calorific value of the core which is assembled in the presently installed RCS cavity**

The result was consistent to the value which was obtained from a measurement of a temperature rise of water in the presently installed RCS cavity.

° **Measurements of a specific heat and a thermal conductivity of the core**

The specific heat was 0.500[J/kg/K]. The thermal conductivities were 0.6[W/m/K] for a radial direction and 7.1[W/m/K] for circumferential and beam directions.

° **Design for the core module**

The FINEMET core is not impregnated with a epoxy resin. The core is used as a functional material, so that no stress is applied on it in the core module.

° **Swelling test**

No swelling was observed.

° **Erosion test**

No erosion was observed.

° **Establishment of a macro model of the core for the electromagnetic calculation**

The FINEMET core was modeled as a bulk which had anisotropic relative permittivities (ϵ_r=15, ϵ_θ=1, ϵ_Z=1) and permeabilities (μ_r=4, μ_θ=3500, μ_Z=3500) in a cylindrical coordinate system.

- **RF designing**

Distributions of the electric field along the beam axis, the magnetic field in the cores, the electric field on the surfaces of the cores, and heat in the cores were derived.

- **Simulations for thermal stresses and contact simulation for the core, and a compression test to verify the simulation**

The results showed a raw core was favorable.

- **Optimization of the geometry of the flow channel with a simulation and a flow visualization test with a half sized flow channel**

The result of the visualization test showed a good agreement with the simulation. Rudders and spout holes were designed and assembled in the flow channel.

- **Interlock system**

The RF source is turned off on the condition of under 34[L/min] for the flow rate or over 70[°C] for the inlet temperature.

- **Fabrication of the prototype cavity**

- **RF test**

The resonance frequency of the prototype cavity is 1.7[MHz]. The shunt impedance is 146[Ω]. The Q factor is 0.8. The heat transfer coefficient is shown in Figure **5.10**.

As mentioned at the beginning of chapter 6, the cavity have to satisfy three parameters.

Resonance frequency

We adjusted the capacitance of the variable capacitor over checking the impedance of the cavity with an LCR meter, and tuned the resonance frequency to 1.7[MHz].

Shunt impedance

A shunt impedance of the cavity was measured when we tuned the resonance frequency. It was 146[Ω]. On the other hand, a shunt impedance was calculated in the RF test. The shunt impedance was derived as 146[Ω] and this value was consistent to the previous one. The value was steady at any dissipated power, so that it was concluded no unusual heating and no discharge appeared.

Q factor

A Q factor of the cavity was obtained with a definition of the equation 5.4. The value was 0.8. In this development, Q is not a practical value of ∼2, however, it will tuned by connecting a parallel inductor to the cavity in the next step.

Therefore, we are able to conclude we have established a method for the development of an accelerating cavity. Current statuses of other two parameters are mentioned below.

Cooling efficiency

A temperature on the surface of the small core was measured with a thermo paint. The temperature was 47°C at a dissipated power in the cores of 4[kW], and 55°C at 7[kW]. These values have a good agreement with the simulation. On the one hand, time constants of the decrements of the Fluorinert temperature were measured. They also have a good agreement with the simulation. The heat transfer coefficients which are obtained from this reliable simulation are shown in Figure **5.10**. Values over 60[L/min] surpass that of the presently installed cavity.

Breakdown voltage

We fabricated an apparatus shown in Figure **6.1** for the breakdown test. The test will be held promptly after preparing a power source and a pulse generator.

For a next stage, we will fabricate a one gap prototype cavity loaded with six core modules and carry out a performance test. The cross-section is shown in Figure **4.1**. A set of three one gap prototype cavities consists a complete accelerating cavity. The semiconductor RF source is not able to provide an enough power for the prototype cavity. A tube amplifier is necessary. An RF test with a large power which is expected after the beam enhancement will be also performed. In parallel with the development of the one gap prototype cavity, a test for a long term operation will be also performed with the prototype cavity which is introduced in this paper. To evaluate a breakdown voltage of the core soaked in Fluorinert, we fabricated a container shown in Figure **6.1** and perform a breakdown test. A small core will be put in the container and applied with pulsed voltages in flowing Fluorinert. Then, we will observe discharges of the core.

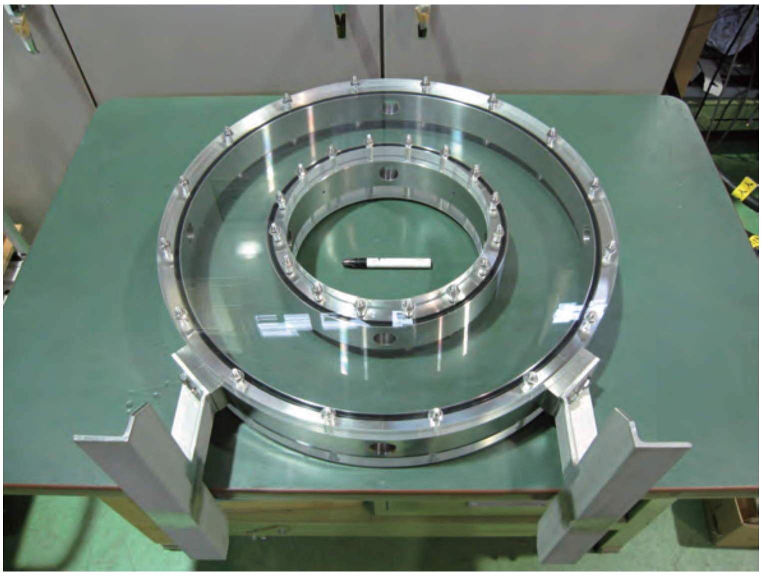

Figure 6.1: An apparatus for the breakdown test

A new cavity for MR is also planed to be developed. The new cavity will be loaded with the FINEMET cores which are radially separated into three and cooled by Fluorinert. Under the existing condition of MR, cut cores are assembled in presently installed accelerating cavities to tune Q factor to ∼25. In the case of the new figure cores, cut is also needed to tune Q. A diamond cutting machine at the machine shop bldg. in KEK will be used to cut cores. The cores of new figure are ”raw core”, so that they will fall apart to pieces with direct cuts. we have to solidify a part of the core before cutting. We are studying about the method for cutting in cooperation with institute of industrial science at the University of Tokyo. Development except cutting will be done with a same process as the new cavity for RCS.

In the future, we will develop an evaporative-cooling-system. Fluorinert suited for evaporation is supposed to be FC-72 which has a low boiling point (56°C). However, we should solve following problems to develop it.

- A FINEMET ribbon can be damaged by a shock wave which appears when a bubble is generated.
- Electric field will concentrates to a bubble remaining between FINEMET layers, and the breakdown voltage will decrease.
- A mechanism to stabilize a pressure inside the cavity, which cancel the variation of the pressure caused by an evaporation and condensation of FC-72, is necessary.

Chapter 7

Conclusions

J-PARC was designed to produce the world's most intensive proton beam and provide it to advanced research facilities for the wide range of field. T2K is one of the most important experiment. It requires 5×10^{21}POT in approximately 5 years which corresponds to 0.75[MW]. To produce proton beam of this intensity, the enhancement of beam is necessary.

There are three methods for the enhancement.

- ○ Increasing the energy of beam
- ○ Increasing the number of proton in the bunch
- ○ Increasing the repetition rate of the accelerator

The third method was accepted. This method requires the accelerating gradient to be enhanced, so that the accelerating cavity will be put in the hard environment to accelerate a large beam current in a long term. A powerful and stable accelerating cavity is indispensable.

The presently installed cavity is loaded with cores made of FINEMET. FINEMET is a magnetic alloy which has characteristics listed below.

- ○ The permeability is high.
- ○ The saturation magnetic-flux-density is high.
- ○ The Curie temperature is high.

These characteristics are suited for the cavity in J-PARC. The cavity is a $\lambda/4$-wave coaxial type. It has three accelerating gaps and each gap has three FINEMET cores on both sides. A stable operation of the presently installed cavities has not established yet, because they have a problem that the FINEMET cores are damaged while the cavities are in operation. We are developing a new accelerating cavity which can be replaced with the presently installed RCS cavity in order to contribute the stabilization and enhancement for the performance of J-PARC ring accelerators.

We simulated the stress in the core, and performed a test for compressing samples of the core. The cause was identified as the buckling which was caused by the thermal stress in the core. We showed the core without impregnation is favorable to prevent the buckling. The development of the new cavity is based on these results.

The new cavity has design concepts which have never been seen before.

- ∘ The cores have unique structure named core module.
    - · Each FINEMET core is radially separated into three. This structure helps to clearly differentiate between constructional materials and functional materials.
    - · These cores are not impregnated. The thermal stresses in the cores are relieved because the cores are soft.
- ∘ A turbulent fluid is used to cool the cores.
    - · Fluorinert is used as the coolant. Fluorinert is chemically inert, so that it is suited for cooling FINEMET cores which is subject to corrosion. Fluorinert flows in the flow channel which is formed on the surfaces of the radially separated cores. The flow channel makes Fluorinert turbulent, so that a high cooling efficiency is realized.

The development of the new cavity has significances below.

- ∘ It has a high degree of potential for solving the difficulty of the stabilization and the enhancement.
- ∘ It can be a prototype of next-generation cavities.

We designed RF structure of the cavity with HFSS and designed the flow channel with ANSYS CFX. We assembled a prototype of the new cavity, and prepared the test facility. This is the first case to use three dimensional FEM (Finite Element Method) simulators for developing a cavity loaded with magnetic alloy cores. The process of this development is scientifically meaningful. We carried out the performance test of the prototype cavity and measured several properties which are essential for an accelerating cavity.

- ∘ The resonance frequency is 1.7[MHz].
- ∘ The shunt impedance is 146[Ω].
- ∘ The Q factor is 0.8.

Results of the measurement for the cooling efficiency are shown below.

- ∘ The temperature on the surface of the small core was measured with the thermo paint. The value was consistent with that was obtained from the simulation.
- ∘ The effective heat transfer coefficient was obtained by measuring the time constant of the temperature decrement of Fluorinert, and the value was consistent with that was obtained from the simulation in 20% .

- The heat transfer coefficient on the surface of the small core was obtained with the simulation. The value is consistent with that was calculated with the empirical equation. The value surpassed that of presently installed cavity over 60[L/min].

We supplied the power to the prototype cavity up to 10[kW], and it worked stably. We accomplished following significant researches.

- We revealed the cause of the buckling of the cores was the thermal stress in the cores. We showed the cores without impregnation is effective to avoid the buckling.
- We assembled the prototype cavity and carried out the performance test. The results of the test satisfy the requirements of RCS so far.

The results of the researches support the feasibility of developing the new cavity. This is the first development of the cavity loaded with magnetic alloy cores, which is able to be operated stably with the large input power of 10[kW] per core. Adopting this new cavity is the most realistic way to stabilize and enhance the performance of the J-PARC ring accelerators.

Acknowledgements

In the first place, the author would like to express the sincere appreciation and gratitude to the supervisor, Prof. Satoru Yamashita, for his help and encouragement throughout six years. The author is thankful to Prof. Tatsuya Kageyama for many discussions and suggestions for the whole work.

Toru Suehiro and Takeshi Takahashi, who were master students in Yamashita laboratory, worked with the author. The author appreciates them for the discussions and the cooperations.

The author are thankful to Prof. Nobuhiro Yoshikawa at Institute of Industrial Science, the University of Tokyo for his help and expertise with the simulation for the thermal stress and the knowledge of the material science.

The author appreciates Dr. Jun Kameda and Dr. Katsushi Hasegawa for the discussions and the instructions of the simulation soft wares.

The author would like to thank Dr. Shiro Torizuka, Dr. Masatoshi Tsukamoto and Dr. Etsuko Tsuchiya at National Institute for Materials Science (NIMS). They strongly assisted the test for compressing the samples of the core.

The author would like to thank Dr. Megumi Akoshima at Advanced Industrial Science and Technology (AIST) for the help to measure the thermal conductivity of FINEMET.

Prof. Hiroo Yoshida at Kanagawa Institute of Technology and Dr. Takehiko Segawa, Dr. Norihiko Iki at AIST gave the suggestions about the development of the flow channel. The author would like to express sincere appreciation to them.

The author appreciates Mr. Yoshisato Funahashi at the machine shop building in KEK for cutting samples of the core.

The author appreciates Dr. Mitsuhiro Yoshida for the advices about the high voltage pulse generator.

The author would like to thank Mr. Katsuhiro Ogura at Hitachi Metals, Ltd. for the informations about FINEMET cores and the production of the core module.

The author appreciates SKILLWELL CO., LTD for the support at the every scene of the development of the prototype cavity.

The author appreciates Taiyo valve MFG. CO., LTD for the cooling system, THAMWAY CO., LTD for the RF source, Sumitomo 3M Limited for Fluorinert.

The author appreciates Dr. Tomohiko Tanabe for checking English of this thesis.

The author extend the appreciation to all staff members of J-PARC and ICEPP for their assistance and support.

This work was supported in part by Japan Society for the Promotion of Science (JSPS) and most part by KEK.

Appendix A

Simplification of the core model against electromagnetic fields

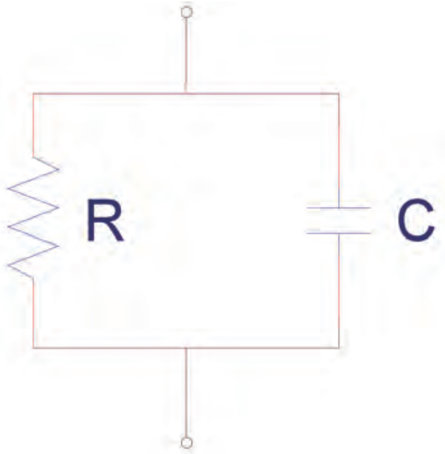

Figure 1.1: An equivalent circuit for a wound structure of a FINEMET core

An equivalent circuit for a wound structure of a FINEMET core can be shown as Figure **1.1**. An impedance of this circuit is written as

$$Z = \frac{1}{\frac{1}{R} + j\omega C} = \frac{R}{1 + j\frac{f}{f_{CR}}}. \tag{A.1}$$

Where, $f_{CR} = \frac{1}{2\pi CR}$. f_{CR} is a critical frequency which determine a path of a signal transmission. A capacitive component is dominant on the condition of $f > f_{CR}$, while, a resistive component is dominant on the condition of $f < f_{CR}$. We define a as an average radius of a core of 0.26[m], w as a width of a FINEMET ribbon of 0.035[m], d_1 as a thickness of the FINEMET ribbon of 18×10^{-6}[m], d_2 as a thickness of an insulating layer of 2×10^{-6}[m], ϵ_r as a relative permittivity of the insulating layer of 4, and ρ as a resistivity of a FINEMET ribbon of 1.2×10^{-6}[Ω·m]. Then, R and C are written as

$$R = \rho \times \frac{2\pi a}{w d_1} = 1.2 \times 10^{-6} \times \frac{2\pi \times 0.26}{0.035 \times 18 \times 10^{-6}} = 3.11, \tag{A.2}$$

$$C = \frac{\epsilon_0 \epsilon_r S}{d_2} = \frac{\epsilon_0 \times 4 \times 2\pi \times 0.26 \times 0.035}{3 \times 10^{-6}} = 6.75 \times 10^{-7}. \tag{A.3}$$

Hence, the critical frequency is derived as $f_{CR} = 76$[kHz]. It is concluded that capacitive component is extremely dominant at 1.7 MHz, so that we can model the core as a concentrically stacked FINEMET cylinders.

Appendix B

Transformation between LR series and parallel circuits

A series circuit with a resistance R$_s$ and an inductance L$_s$, and a parallel circuit with a resistance R$_p$ and an inductance L$_p$ are shown in Figure **2.1**. In the case of the series circuit, an impedance Z=R$_s$+jωL$_s$ is transformed as

$$\frac{1}{Z} = \frac{1}{\frac{\omega^2 L_s^2}{R_s}\left(1 + \frac{R_s^2}{\omega^2 L_s^2}\right)} + \frac{1}{j\omega L_s\left(1 + \frac{R_s^2}{\omega^2 L_s^2}\right)} \tag{B.1}$$

In the case of the parallel circuit, an impedance is written as

$$\frac{1}{Z} = \frac{1}{R_p} + \frac{1}{j\omega L_p}. \tag{B.2}$$

Equaling them, a following equation is deduced.

$$R_p = \frac{\omega^2 L_s^2}{R_s}\left(1 + \frac{R_s^2}{\omega^2 L_s^2}\right) \tag{B.3}$$

Thus, we are able to transform a series circuit to a parallel circuit. In the case of $\omega L_s \gg R_s$, the equation is approximated as

$$R_p \approx \frac{\omega^2 L_s^2}{R_s} \tag{B.4}$$

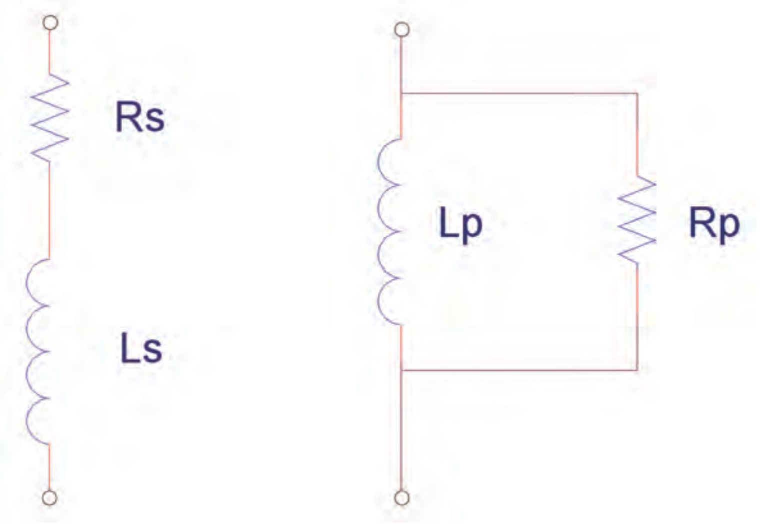

Figure 2.1: A series circuit and a parallel circuit

Appendix C

Measurement of a specific heat of a FINEMET core at KEK

A specific heat of the FINEMET core was measured at KEK, independently of the measurement at the Cryogenic Research Center. The sample which was heated up to 100° with a hotplate was dipped in water, then, its specific heat was calculated with temperature variations of the water and the sample. Their temperatures were monitored with thermocouples. C_w, M_w, and $\Delta\mathrm{T}_w$ are a specific heat, a mass, and a temperature variation of the water, respectively. C_c, M_c, and $\Delta\mathrm{T}_c$ are a specific heat, a mass, and a temperature variation of the sample, respectively. We assumed a calorific value which was radiated by the sample and that was absorbed by the water are equal, namely, the radiation to the out of system was small. Then, a following equation is deduced.

$$C_w M_w \Delta T_w = C_c M_c \Delta T_c \tag{C.1}$$

Hence, a specific heat of the sample is deduced as

$$C_c = \frac{C_w M_w \Delta T_w}{M_c \Delta T_c}. \tag{C.2}$$

The measurements were performed twice.

○ First trial
Mass of the water: 633.63[g], Mass of the sample: 372.45[g], Specific heat of the water: 4.2[J/g/K]

Table 3.1: Specific heat measurement (First trial)

	initial state	final state	difference of temperature
temperature of water [°C]	18.3	24.3	6
temperature of sample [°C]	108.1	24.3	83.8

Specific heat of sample: 0.511[J/kg/K]

◦ Second trial

Mass of the water: 681.86[g], Mass of the sample: 372.45[g], Specific heat of the water: 4.2[J/g/K]

Table 3.2: Specific heat measurement (Second trial)

	initial state	final state	difference of temperature
temperature of water [°C]	20.7	29.3	8.6
temperature of sample [°C]	152.9	29.3	123.6

Specific heat of sample: 0.535[J/kg/K]

Averaging the results of the measurements, we derived the specific heat of the sample of 0.523[J/kg/K]. This value was consistent with that was measured at the Cryogenic Research Center.

Appendix D

Calculations of heat transfer coefficients

A transfered calorific value per area, which is based on a difference between a temperature of certain substance of T[K] and that of a circumstance of T_∞[K] is represented as $h(T - T_\infty)$[W/m^2] using a coefficient h. h[W/m^2/K] is called a heat transfer coefficient. That is,

$$\frac{\rho V C}{A}\frac{dT}{dt} = h(T - T_\infty) \tag{D.1}$$

is deduced. Where, ρ[kg/m^3], V[m^3], A[m^2], and C[J/kg/K] are a density, volume, area, and specific heat of the substance. In the simulation by ANSYS CFX, a temperature of the core is calculated with Prandtl number first, then, h is determined. In the hand calculation, h is calculated by a following procedure. The heat transfer coefficient h is determined by introducing Nusselt number Nu.

$$h = \frac{\lambda \cdot Nu}{L} \tag{D.2}$$

Where, λ[W/m/K] is a heat transfer coefficient of the fluid, and L[m] is a characteristic linear dimension of the flow channel. Considering a rectangular flow channel with their sides of a[m] and b[m], the L can be written as

$$L = 4\frac{ab}{2(a+b)}. \tag{D.3}$$

The equation (D.2) shows Nu is needed for determining h. The procedures to obtain Nu are different between the cases of a laminar and a turbulence.

D.1 Laminar

Nu of laminar is a constant which is determined by the geometry of the flow channel and a heating condition.

$$Nu = 4.9 \tag{D.4}$$

Hence, h can be written as

$$h = \frac{4.9\lambda}{L}. \tag{D.5}$$

D.2 Turbulence

Using Reynolds number Re and Prandtl number Pr, Nu is written as[70]

$$Nu = 0.023Re^{0.8}Pr^{0.33}. \tag{D.6}$$

Reynolds number is a nondimensional parameter which is defined as

$$Re \equiv \frac{UL}{\nu}. \tag{D.7}$$

Where, U[m/s] is a mean velocity of the flow and ν[m^2/s] is a dynamic viscosity of the fluid. Prandtl number is a nondimensional parameter which is defined as

$$Pr \equiv \frac{\nu}{\alpha}. \tag{D.8}$$

Where, α[m^2/s] is a thermal diffusivity of the fluid and is defined as

$$\alpha \equiv \frac{\lambda}{\rho C}. \tag{D.9}$$

h is derived by substituting Nu of the equation D.6 to the equation D.2. Schematic view of the presently installed core in RCS (cooled by laminar water) is shown in Figure **4.1**. A characteristic linear dimension is written as

$$L = 4\frac{0.2395 \times 0.003}{2(0.2395 + 0.003)} = 5.926 \times 10^{-3}[\mathrm{m}]. \tag{D.10}$$

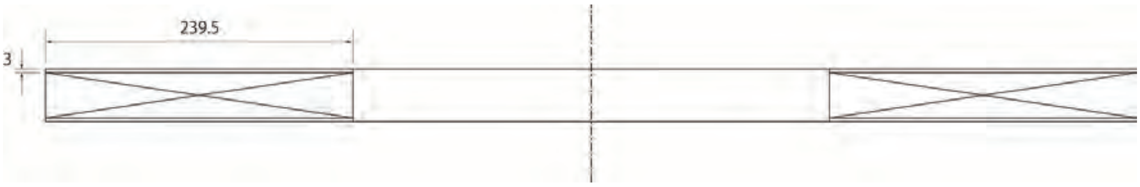

Figure 4.1: RCS flow channel

A thermal conductivity of water is $\lambda = 0.6151$ [W/m/K] (30°C), so that, h can be written as

$$h = \frac{4.9 \times 0.6151}{5.926 \times 10^{-3}} = 500[\mathrm{W/m^2/K}]. \tag{D.11}$$

A flow channel geometry of the new cavity (cooled by turbulent Fluorinert) is shown in Figure **4.2**. Therefore, the characteristic linear dimension is written as

$$L = 4\frac{0.081 \times 0.005}{2(0.081 + 0.005)} = 9.42 \times 10^{-3}[\mathrm{m}] \tag{D.12}$$

An inlet temperature of Fluorinert was approximately 40[°C] in the RF test. Properties of Fluorinert at 40[°C] are shown below.

density: 1780[kg/m^3]

specific heat: 1076[J/kg/K]

thermal conductivity: 0.0624[W/m/K]

dynamic viscosity: 5.9×10^{-7}[m^2/s]

Hence, Re, α, Pr of U=0.5[m/s] are written as

$$Re = \frac{0.5 \times 9.42 \times 10^{-3}}{5.9 \times 10^{-7}} = 7.98 \times 10^3, \tag{D.13}$$

$$\alpha = \frac{0.0624}{1780 \times 1076} = 3.26 \times 10^{-8}[\mathrm{m}^2/\mathrm{s}], \tag{D.14}$$

$$Pr = \frac{5.9 \times 10^{-7}}{3.26 \times 10^{-8}} = 18.1 \tag{D.15}$$

Therefore,

$$Nu = 0.023 \times (7.98 \times 10^3)^{0.8} \times (18.1)^{0.33} = 79.9. \tag{D.16}$$

Hence,

$$h = \frac{0.0624 \times 79.9}{9.42 \times 10^{-3}} = 530[\mathrm{W/m^2/K}]. \tag{D.17}$$

Figure 4.2: Prototype flow channel

Appendix E

Calculations for shunt impedances of a presently installed RCS core and a new configuration core

A complex relative permeability of a FINEMET core is written as

$$\mu' = \mu_s' - j\mu_s''. \tag{E.1}$$

Then, an impedance of a one turn coil with the FINEMET core whose circuit schematic is shown in Figure **5.1** can be written as

$$Z = j\omega\mu L_0 = j\omega(\mu_s' - j\mu_s'')L_0 = \omega\mu_s'' L_0 + j\omega\mu_s' L_0 = r + j\omega L. \tag{E.2}$$

Where, r and L are defined as

$$r \equiv \omega\mu_s'' L_0, \tag{E.3}$$

$$L \equiv \mu_s' L_0. \tag{E.4}$$

L_0 is an inductance of an air cored coil. An inductance per unit length is written as

$$L_{0u} = \frac{\mu_0}{2\pi}\int_{r1}^{r2} \frac{1}{r} dr. \tag{E.5}$$

Where, r_1 and r_2 are an inner diameter and outer diameter of the core, respectively.

Figure 5.1: A circuit of a one turn coil with a FINEMET core

Applying the result of Appendix B, we can write a shunt impedance R as

$$R = r + \frac{\omega^2 L^2}{r}. \tag{E.6}$$

The presently installed RCS core has an inner diameter of 187.5[mm], an outer diameter of 425[mm] and a thickness of 35[mm]. Hence,

$$L_{0u} = \frac{\mu_0}{2\pi} \int_{0.1875}^{0.425} \frac{1}{r} dr = 0.130\mu_0[\mathrm{H/m}]. \tag{E.7}$$

Therefore,

$$L_0 = 0.035 \times L_{0u} = 5.72 \times 10^{-9}[\mathrm{H}] \tag{E.8}$$

is derived. Average relative permeabilities of the core at 1.7 MHz are

$$\mu_s' = 1200, \tag{E.9}$$

$$\mu_s'' = 2100. \tag{E.10}$$

A shunt impedance of the presently installed RCS core can be written as

$$R = \omega\mu_s'' L_0 + \frac{\omega^2(\mu_s' L_0)^2}{\omega\mu_s'' L_0} = 170[\Omega]. \tag{E.11}$$

In the case of radially separated cores, a shunt impedance R of a core module is derived by summing shunt impedances of a small, medium, and large core.

small core: R_S=71.4[Ω]

medium core: R_M=50.3[Ω]

large core: R_L=39.0[Ω]

Hence, R is deduced as

$$R = R_S + R_M + R_L = 161[\Omega]. \tag{E.12}$$

The value is almost same as the shunt impedance of the presently installed RCS core (The difference is 5%) .

Appendix F

A characteristic of $\mu' Q$[72]

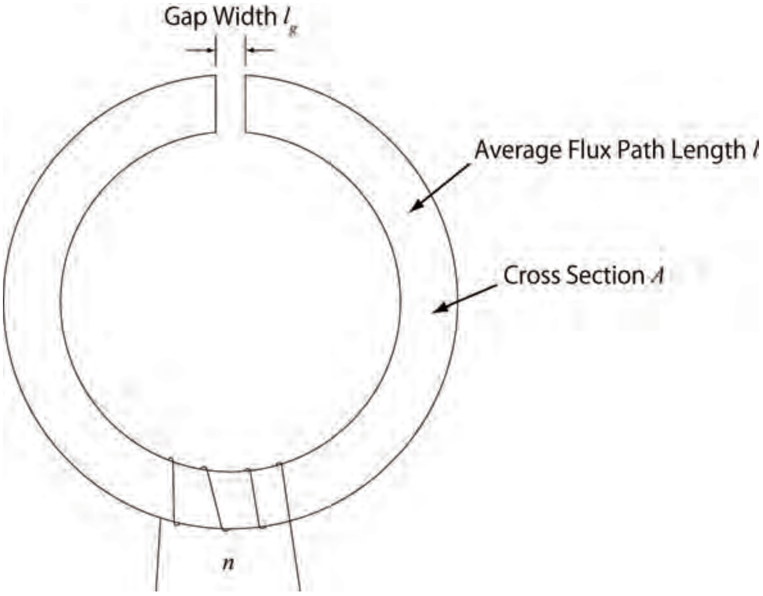

Figure 6.1: gap core

A magnetic resistance R_m in Figure **6.1** is written as

$$R_m = \frac{l}{\mu A} + \frac{l_g}{\mu_0 A}. \tag{F.1}$$

Where, μ is a permeability of the core. Introducing an effective permeability μ_{app}, R_m can be written as

$$R_m = \frac{l + l_g}{\mu_{app} A}. \tag{F.2}$$

The equation (F.1) and the equation (F.2) lead an following equation.

$$\frac{\mu_0}{\mu_{app}} = \frac{\mu_0}{\mu} \frac{l}{l + l_g} + \frac{l_g}{l + l_g} \tag{F.3}$$

Assuming $l \gg l_g$, approximations of $\frac{l}{l+l_g} \approx 1$, $\frac{l_g}{l+l_g} \approx \frac{l_g}{l} \equiv k$ are derived. Then, the equation F.3 can be written as

$$\frac{1}{\mu_e} = \frac{1}{\mu_r} + k. \tag{F.4}$$

Where, μ_e is an effective relative permeability, and μ_r is a relative permeability of the core. By using a complex representation of relative permeability, which is defined as

$$\mu_e = \mu_e' - j\mu_e'', \tag{F.5}$$

$$\mu_r = \mu_r' - j\mu_r'', \tag{F.6}$$

the equation F.4 can be written as

$$\frac{1}{\mu_e' - j\mu_e''} = \frac{1}{\mu_r' - j\mu_r''} + k. \tag{F.7}$$

After rationalization, the equation can be expressed as

$$\frac{\mu_e'}{\mu_e'^2 + \mu_e''^2} + j\frac{\mu_e''}{\mu_e'^2 + \mu_e''^2} = \frac{\mu_r'}{\mu_r'^2 + \mu_r''^2} + k + j\frac{\mu_r''}{\mu_r'^2 + \mu_r''^2}. \tag{F.8}$$

Equaling both real parts and both imaginary parts respectively, two equations are derived.

$$\text{Real part: } \frac{\mu_e'}{\mu_e'^2 + \mu_e''^2} = \frac{\mu_r'}{\mu_r'^2 + \mu_r''^2} + k \tag{F.9}$$

$$\text{Imaginary part: } \frac{\mu_e''}{\mu_e'^2 + \mu_e''^2} = \frac{\mu_r''}{\mu_r'^2 + \mu_r''^2} \tag{F.10}$$

We define tanδ_e and tanδ as below.

$$\tan\delta_e \equiv \frac{\mu_e''}{\mu_e'} \tag{F.11}$$

$$\tan\delta \equiv \frac{\mu_r''}{\mu_r'} \tag{F.12}$$

Then, the equation (F.10) can be written as

$$\frac{\mu_e'}{\mu_e'^2 + \mu_e''^2}\tan\delta_e = \frac{\mu_r'}{\mu_r'^2 + \mu_r''^2}\tan\delta. \tag{F.13}$$

Hence,

$$\mu_e'\left(Q_e + \frac{1}{Q_e}\right) = \mu_r'\left(Q + \frac{1}{Q}\right) \tag{F.14}$$

is derived with the definitions of

$$Q_e \equiv \frac{1}{\tan\delta_e}, \tag{F.15}$$

$$Q \equiv \frac{1}{\tan\delta}. \tag{F.16}$$

In most cases, $1 \ll Q_e$ and $1 \ll Q$ hold, so that the equation (F.14) can be written as

$$\mu_e' Q_e = \mu_r' Q. \tag{F.17}$$

After cutting a core, the relative permeability increase and Q decrease, however, the equation F.17 shows a product of them $\mu_r' Q$ does not vary. Thus, this product is a very important practice.

Appendix G

Selection of μ_s and μ_p for simulations of electromagnetic fields[73]

There are two expressions of a complex representation for a relative permeability.

$$\mu = \mu'_s + j\mu''_s \tag{G.1}$$

$$\frac{1}{\mu} = \frac{1}{\mu'_p} - j\frac{1}{\mu''_p} \tag{G.2}$$

In the case of a coil with a core of relative permeability μ, the loss of the inductor is able to be represented by a resistance which is connected in series in the equivalent circuit as shown in left of Figure **2.1**. An impedance of the inductor is written as

$$Z = j\omega L = j\omega\mu L_0 = j\omega L_0(\mu'_s - j\mu''_s) = \omega\mu''_s L_0 + j\omega\mu'_s L_0 \equiv L_s + j\omega R_s. \tag{G.3}$$

Where, L_0 is an inductance of an air-cored coil. On the other hand, if we assume the resistance is connected in parallel as shown in right of Figure **2.1**, the impedance of the inductor is expressed as

$$\frac{1}{Z} = \frac{1}{j\omega\mu L_0} = \frac{1}{j\omega L_0}\left(\frac{1}{\mu'_p} - \frac{1}{j\mu''_p}\right) = \frac{1}{\omega\mu''_p L_0} + \frac{1}{j\omega\mu'_p L_0} \equiv \frac{1}{L_p} + \frac{1}{j\omega R_p}. \tag{G.4}$$

Therefore, μ'_s and μ'_p have to be utilized for simulations of electromagnetic fields in the case of lossy calculation and no loss calculation, respectively.

Appendix H

A relation between a heat transfer coefficient and a time constant

The equation D.1 introduced in Appendix D is shown here, again.

$$\frac{\rho V C}{A}\frac{dT}{dt} = h(T - T_0) \tag{H.1}$$

Assuming $T = T_0$ at $t = 0$, a solution of the equation (H.1) is written as

$$T = T_\infty - (T_\infty - T_0)\exp\left(-\frac{hA}{\rho V C}t\right). \tag{H.2}$$

Therefore, a time constant for the variation of a temperature can be expressed as

$$\frac{1}{\tau} = \frac{hA}{\rho V C}. \tag{H.3}$$

Values of A, ρ, V, and C are known, so that h is obtained by a measurement of τ.

Appendix I

Physics

Many researches of wide range of fields are carried out at J-PARC. In this section, we introduce these researches focused on elementary particle physics experiments.

I.1 T2K experiment

J-PARC neutrino oscillation experiment (T2K: from Tokai to Kamioka) is a long baseline neutrino oscillation experiment to detect ν_μ neutrino beam which is emitted from the neutrino beam line in J-PARC. The detector is a Large Water Cherenkov detector called "Super Kamiokande" (SK) in Hida-shi, Gifu-ken which is 295 km away from J-PARC. The beam line for T2K experiment is shown in Figure **9.1**. It is allocated inside of 30 GeV proton synchrotron (MR). 8 bunches injected MR are accelerated up to 30 GeV, then they are kicked by a kicker and extracted to the beam line. This process is called "Fast Extraction" comparing with the "Slow Extraction" (the extraction to the Hadron Experimental Hall). After being bended right angle at the arc, the proton beam is focused by electromagnets, then collides with a target and produces pions. These pions decay while they are traveling in a decay pipe (93 m long), then, neutrinos which are produced by the decays of pions travel to SK. The direction of the carbon target is shifted 2.5° from the direction of SK on purpose[3]. This shift allows the neutrino beam to have a narrow energy band. This method is called an off-axis scheme.

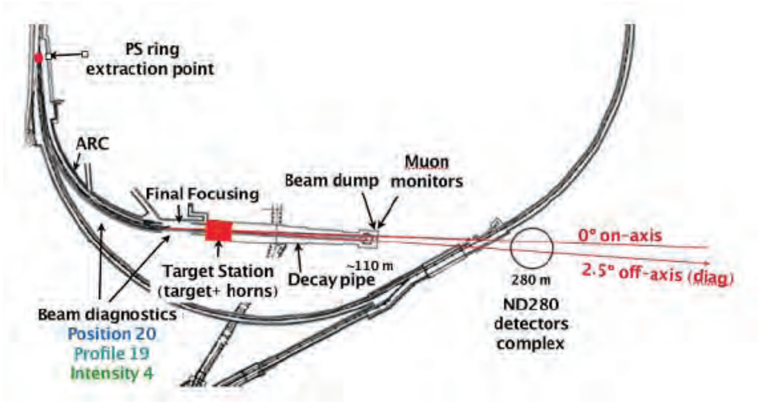

Figure 9.1: The beam line for T2K experiment[6]

After the beam enhancement, the peak energy of neutrino beam will be $E_{peak} = 0.7$ [GeV], the neutrino flux will be $\nu_\mu = 19.25 \times 10^6/\mathrm{cm}^2/\mathrm{yr}$ on the condition that the beam power of MR is 0.75 MW, the fiducial volume is 22.5 kton, and OA2° (shift the emitting neutrino beam direction 2° from SK). The neutrino flux was calculated by the Monte Carlo simulation using GEANT[7] based on Calor-Fluka model. The event rate measured at near detector of K2K shows this Monte Carlo is correct within 20% accuracy. This flux is 50 times larger than that of K2K experiment. The aim is 5×10^{21} POT in approximately 5 years operation. Main purposes of T2K are below.[3]

I.1.1 Accurate measurement of ν_μ disappearance parameter

An accurate measurement of the oscillation parameter of ν_μ disappearance ($\sin^2 2\theta_{\mu\tau}$, Δm^2_{23}) which is established by the measurement of atmospheric neutrino at SK and K2K experiment will be performed. A Charged Current Quasi-Elastic interaction (CC-QE interaction) of neutrino in SK is expressed as

$$\nu_l + n \to l + p. \tag{I.1}$$

Where, l is lepton and $l = e$ or μ. A neutrino energy of this interaction can be written as

$$E_\nu = \frac{m_N E_l - m_l^2/2}{m_N - E_l + p_l \cos\theta_l}. \tag{I.2}$$

Where, m_N is the mass of neutron, m_l is the mass of lepton, E_l is the energy of lepton, p_l is the momentum of lepton, θ_l is the scattering angle of lepton. Subtracting CC non-QE event and neutral current (NC) event that are backgrounds from the neutrino energy spectrum, a true neutrino energy spectrum is obtained. Numbers of each event on the condition of OA2.5°, 5×10^{21} POT are shown in Table **9.1**. A ratio between the spectrum expected to be measured at SK, which is calculated by sweeping the oscillation parameter on Monte Carlo, and that is calculated in the case of no oscillation is shown in Figure **9.2**. The spectrum simulation subtracted background events is used for the ratio. The oscillation peak is seen at $E_\nu \sim 0.65$ GeV. This results the statistical errors of $\sin^2 2\theta_{23}$ and Δm_{23} are 0.009 and 5×10^{-5} eV^2 respectively. 5×10^{21} POT used in the simulation is the value of 5 years operation on the condition of enhanced MR beam power of 0.75 MW (130 days per year for the operation of the accelerator is assumed). Therefore, enhancing accelerator performance is essential to achieve target values of $\delta(\sin^2 2\theta_{23}) = 0.01$, $\delta(\Delta m^2_{23}) = 10^{-4}$ eV^2.[3]

Table 9.1: Numbers of each event on the condition of OA2.5°, 5×10^{21} POT[3]

Δm^2_{23} (eV^2)	CC-QE	CC-nonQE	NC	all ν_μ
No oscillation	3,620	1,089	96	4,805
2.0×10^{-3}	933	607	96	1,636
2.3×10^{-3}	723	525	96	1,344
2.7×10^{-3}	681	446	96	1,223
3.0×10^{-3}	800	414	96	1,310

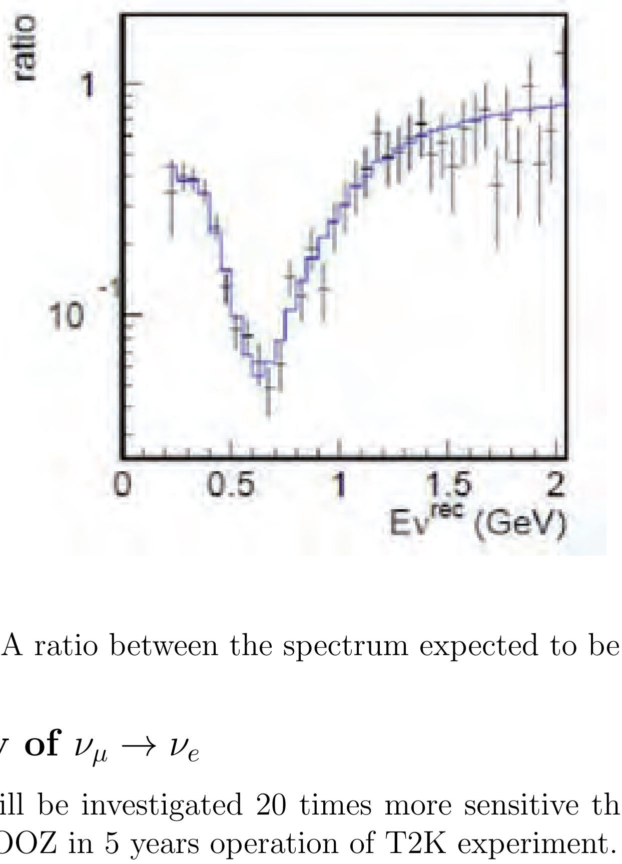

Figure 9.2: A ratio between the spectrum expected to be measured[5]

I.1.2 Discovery of $\nu_\mu \to \nu_e$

$\nu_\mu \to \nu_e$ oscillation will be investigated 20 times more sensitive than the present upper limit reported by CHOOZ in 5 years operation of T2K experiment. CHOOZ is a nuclear reactor experiment to examine the $\bar{\nu}_e \to \bar{\nu}_x$ $(x = \nu\ or\ \tau)$ oscillation. The aim is $\sin^2 2\theta_{13} \sim 2\sin^2 2\theta_{\mu e} > 0.006$. This oscillation is the unique mode which has not discovered yet, and is expected to show the notice of CP violation measurements in the future. Hence, it is the most important measurement of T2K. Because the momentum of protons in CC-QE interaction is lower than the Cherenkov threshold, only an e-like ring can be seen as a signal for discovery of ν_e. There are three expected backgrounds.

1. the misidentification between e and μ
2. the ν_e contamination in ν_μ beam
3. the photon generation from the pion decay

For 1, the μ background will be excluded by extracting single ring e-like event in SK. For 2, it is known that the contamination is $0.2 \sim 0.3\%$ at peak energy of ν_μ spectrum which is derived from the simulation. For 3, the cause is misidentifying the 2 photons generated by π_0 decays. These π_0 are generated in the NC interaction and CC non-QE interaction. To eliminate this background, cutting the interaction having a sharp peak which is unique to π_0 decay is applied. Numbers of events after each separation are shown in Table **9.2**.

Table 9.2: Numbers of events after each separation[9]

OAB 2°	ν_μC.C.	ν_μN.C.	Beam ν_e	Oscillated ν_e
Generated in F.V.	10713.6	4080.3	292.1	301.6
1R e-like	14.3	247.1	68.4	203.7
e/π^0 separation	3.5	23.0	21.9	152.2
0.4GeV<E_{rec} <1.2GeV	1.8	9.3	11.1	123.2

A reconstructed neutrino energy spectrum is shown in left of Figure **9.3**. Where, an operation time of 5 years and $\Delta m^2 = 3 \times 10^{-3}\text{eV}^2$, $\sin^2 2\theta_{\mu e} = 0.05$ are assumed. 90% C.L. parametrized with the operation time and 3σ restriction are derived by integrating the number of events in the region 0.4-1.2 GeV. They are shown in right of Figure **9.3**. Therefore, $\sin^2 2\theta_{\mu e} = 0.003$, 90% C.L. is obtained on the condition of 5×10^{21} POT after beam enhancement. The variation of $\sin^2 2\theta_{\mu e}$ on the condition of sweeping Δm^2 is shown in Figure **9.4**. Focusing on the expected region $1.6 \times 10^{-3}\text{eV}^2 < \Delta m^2 < 4 \times 10^{-3}\text{eV}^2$, the statistics error is better than at least $\sin^2 2\theta_{\mu e} = 0.005$ namely $\sin^2 2\theta_{13} = 0.01$, 90% C.L. . The aim is $\sin^2 2\theta_{13} \sim 2\sin^2 2\theta_{\mu e} > 0.008$[10]. Hence, the beam enhancement is dispensable.

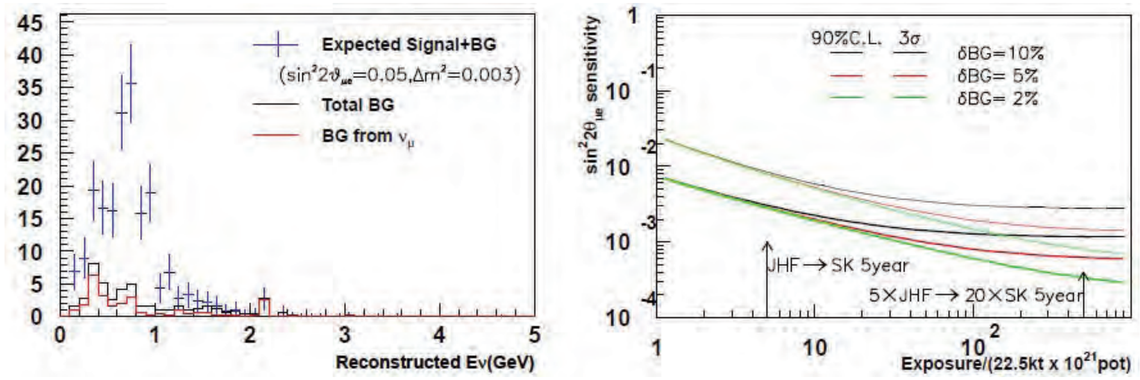

Figure 9.3: A reconstructed neutrino energy spectrum in the left. 90% C.L. parametrized with the operation time and 3σ restriction are in the right. [3]

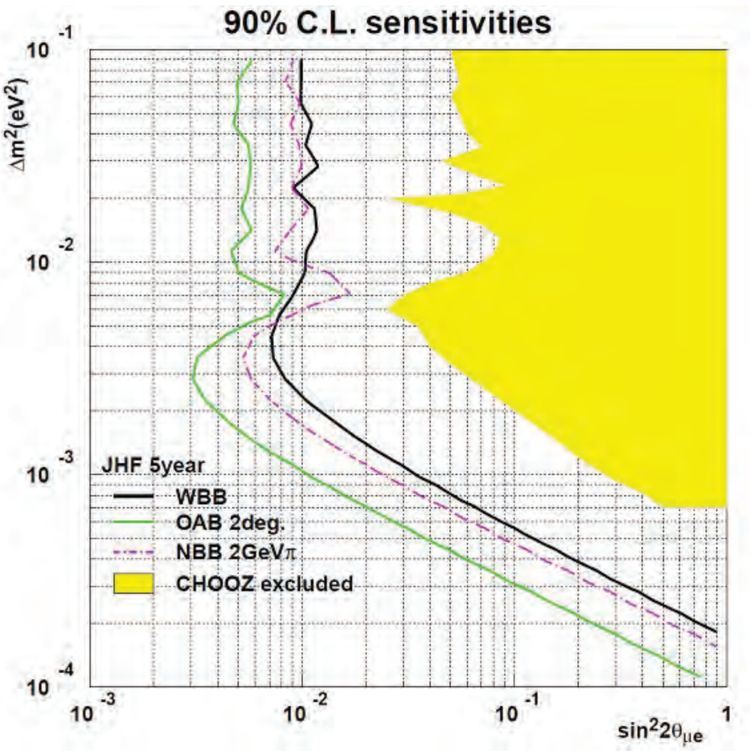

Figure 9.4: The variation of $\sin^2 2\theta_{\mu e}$ on the condition of sweeping Δm^2 [3]

I.2 Search for $\mu^- - e^-$ conversion

PRIME (PRISM Mu E conversion) is an experiment to search LFV $\mu^- - e^-$ conversion (μ^-+Ti→ e$^-$+Ti) in μ atom with the sensitivity of 10^{-18} by means of an intensive μ source called PRISM (Phase Rotated Intense Slow Muon source). PRISM aims the μ

rate of $10^{11} - 10^{12}$ μ/sec on the condition of an injection rate of 10^{14} [protons/sec] (after the beam enhancement). The experimental hall is in MLF (Materials and Life Science Experimental Facility) shown in Figure **1.2**. Single event sensitivity in 5 years will reach B(μ^-+Ti→e$^-$+Ti)$\sim 3 \times 10^{-18}$ on the condition of $3.0 \times 10^{10} \mu^-$/sec.

Particles which fly backward with an angle over 55° are reflected by a solenoidal magnetic field at target section. As a result, approximately 80% of $\mu - e$ conversion electrons are injected into the spectrometer at downstream. The spectrometer is shown in Figure **9.5**. It has a curve and magnetic field is applied on. This configuration lets only the particles having the momentum of 105 MeV/c pass. Other particles are excluded by a blocker installed in the spectrometer. The transmissivities through this structure are 53.0% for vertical direction and 100% for horizontal direction. If the angle of electrons from the target is small, the radius of solenoidal orbits of the electrons become too small to measure the momentum of them with enough accuracy. Therefore, the limitation of $\sin\theta > 0.33$ is imposed. This limitation corresponds to $p_t > 86$ MeV/c. The acceptance for this limitation is 82.3% . The product of these values leads to a detector geometrical acceptance of 34.6% . Acceptances at each part are shown in Table **9.3**. Assuming the analysis efficiency is 80% , detection efficiency which is derived by multiplying all values is 22%[11]. Then, to achieve the branching ratio of

$$\mathrm{B}(\mu^- + \mathrm{Ti} \to \mathrm{e}^- + \mathrm{Ti}) \sim \frac{1}{N_\mu \dot{A}_\mu} < 10^{18} \tag{I.3}$$

, number of μ $N_\mu > 10^{19}$ is needed. That means the proton beam enhancement is essential.

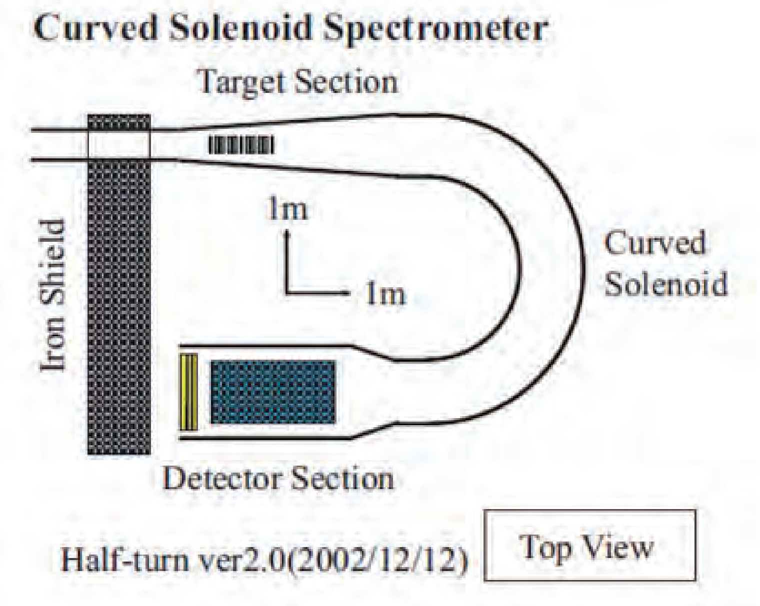

Figure 9.5: A schematic view of the curved solenoid spectrometer[11]

Table 9.3: Acceptances at each part of the curved solenoid spectrometer[11]

Condition	Section	Fraction	Net acceptance
Forward direction	Target	79.3%	79.3%
Blocker cut (vertical)	Curved solenoid	53.0%	42.0%
Blocker cut (horizontal)	Curved solenoid	100%	42.0%
sinθ >0.33	Detector	82.3%	34.6%

As stated above, the beam enhancement is required by each experiment.

Appendix J

An RF accelerating cavity loaded with magnetic cores for a proton and ion synchrotron

J.1 A cavity loaded with ferrite cores

Toroidal ferrite cores are widely used for RF accelerating cavities in proton and ion synchrotrons. The core has a function of increasing the inductance of the cavity. It allows the resonance frequency of the cavity to be in the order of MHz. An accelerating cavity loaded with FINEMET cores has almost same structure, however it does not have a feedback system for tuning its resonance frequency. Details are shown in a following section. An accelerating gradient of the cavity is expected to be approximately twice as high as that of the cavity loaded with ferrite cores, because FINEMET has relative magnetic permeability, saturation magnetic-flux-density and Curie temperature which are higher than those of ferrite. In this section, we will review cavities loaded with ferrite cores, which have been used for a long time and classify them based on their characteristics. A list of proton and ion accelerating cavities loaded with ferrite cores is shown in Table **10.1**.

Table 10.1: A chronology of accelerating cavities loaded with ferrite cores

Year	Accelerator	Laboratory	Type
1958	SATURNE	SACLAY	Coaxial B[54]
1959	PS	CERN	Coaxial A
1960[28]	AGS	BROOKHAVEN	Coaxial A[29]
1967	U70	IHEP	Coaxial B[30]
1971[31]	BOOSTER	FNAL	Drift Tube
1972[32]	PSB	CERN	Coaxial B[33]
1972[34]	LAMPF	Los Alamos	Coaxial D[35]
1974	PSB	KEK	Coaxial B[36]
1976	PS	KEK	Coaxial B[37]
1982	LEAR	CERN	Coaxial C
1982	IPNS	ARGONNE	Coaxial B[38]
1984	ISIS	RAL	Coaxial A
1987[39]	MIMAS	SACLAY	Coaxial C[40]
1988[41]	CELSIUS[42]	CELSIUS	Coaxial C[43]
shelved	The Kaon Factory	TRIUMF	Coaxial D[44]
1990[45]	SIS	GSI	Coaxial B*[46]
1991[47]	BOOSTER	BROOKHAVEN	Coaxial B[48]
1993[49]	COSY	IKP	Coaxial B[77]
1999[50]	MI	FNAL	Drift Tube[51]
2006	SNS	ORNL	Coaxial C[52]

*Not push-pull arrangement

J.1.1 Ferrites for accelerating cavites

Mn-Zn type and Ni-Zn type ferrites are generally used for producing cores. Mn-Zn ferrite has electrical resistivity from 10 to a few hundreds [Ωcm]. A few hundreds kHz is an upper limit as a low loss core because of the presence of an eddy current. The relative magnetic permeability is a few thousand. On the other hand, the electrical resistivity of Ni-Zn ferrite is over 10^5[Ωcm]. It can be used up to a few MHz. However the limit of the relative permeability is approximately 1000[56]. Ni-Zn ferrite is widely used for an accelerating cavity[53].

J.1.2 Classification of cavities loaded with ferrite cores

There are two types of a accelerating cavities loaded with ferrite cores. One is a coaxial type, the other is a drift tube type[37].

J.1.3 Coaxial type cavity

A structure of a coaxial type cavity is the $\lambda/4$-wave coaxial resonator loaded with toroidal ferrite cores. The cores increase the inductance of the cavity and its resonance frequency decreases to the value which is suited to the acceleration of protons and ion beams. This type cavity is used on the condition of the frequency from a few hundreds kHz to approximately 10 MHz. The coaxial cavity is classified to four groups[37].

Type A

A Schematic view of an ISIS cavity is shown in Figure **10.1**. Black parts represent ferrite cores. Ferrite is used as a medium in the coaxial tube. Electromagnetic field existing in the coaxial tube can penetrates an accelerating gap made of alumina. The penetrated field accelerates beams. The resonance frequency is tuned in order to follow the increase of the beam velocity. A tuning method is to control the relative magnetic permeability of ferrite cores. The way of the control is to apply bias magnetic fields on the cores. The resonance frequency is tuned in order to follow the increase of the beam velocity. Wires are wound on cores, which are shown in Figure **10.1**, carry DC current and induce bias magnetic fields.

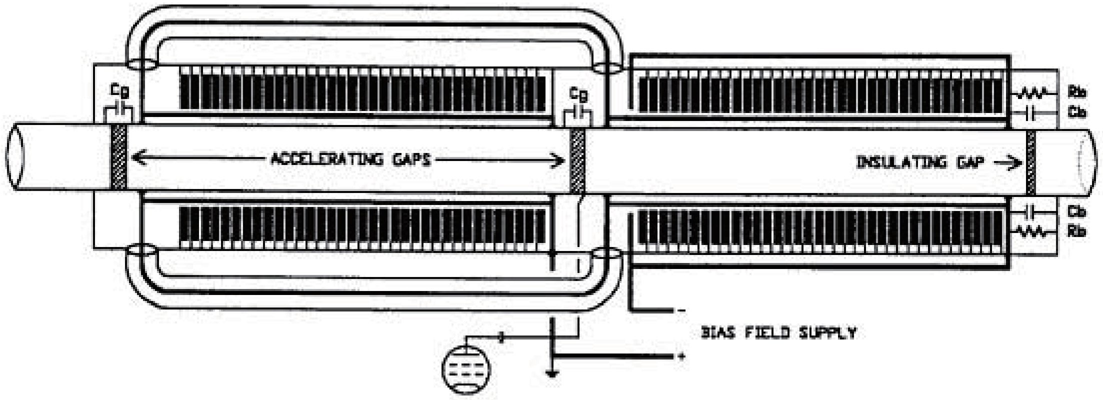

Figure 10.1: A schematic view of a type A cavity[54]

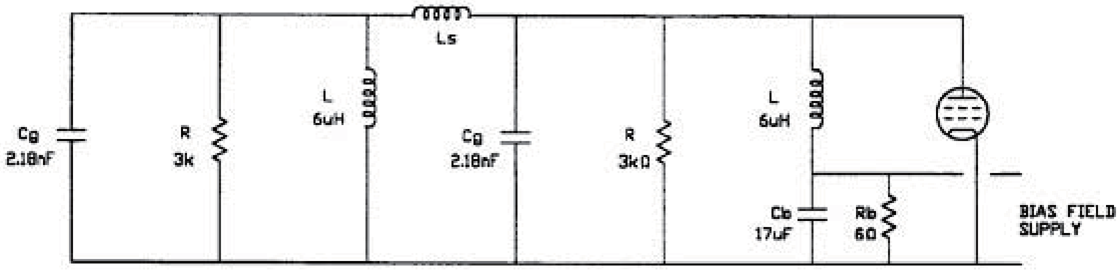

Ls = Coupling transmission line inductance

Figure 10.2: An equivalent circuit of a type A cavity[54]

Type B

A push-pull voltage is impressed on the accelerating gap. Wires are wound like a figure of eight which is able to cancel out induced RF voltages.

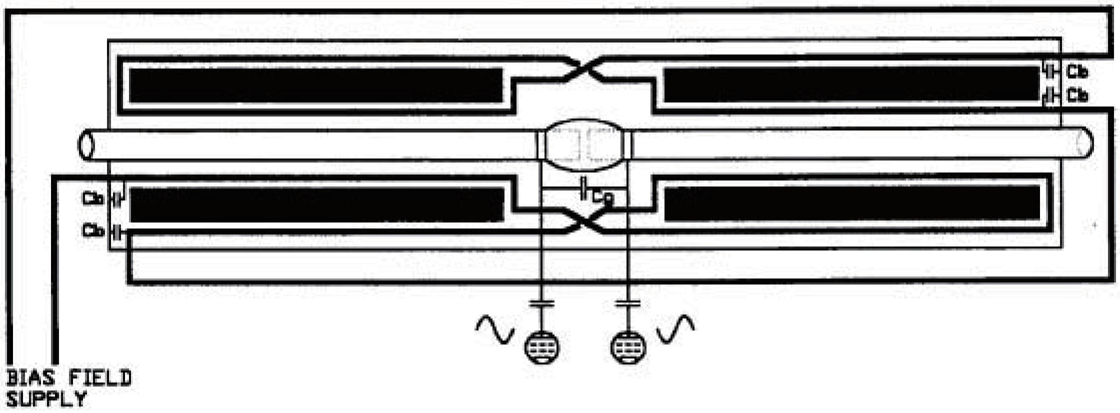

Figure 10.3: A schematic view of a type B cavity[54]

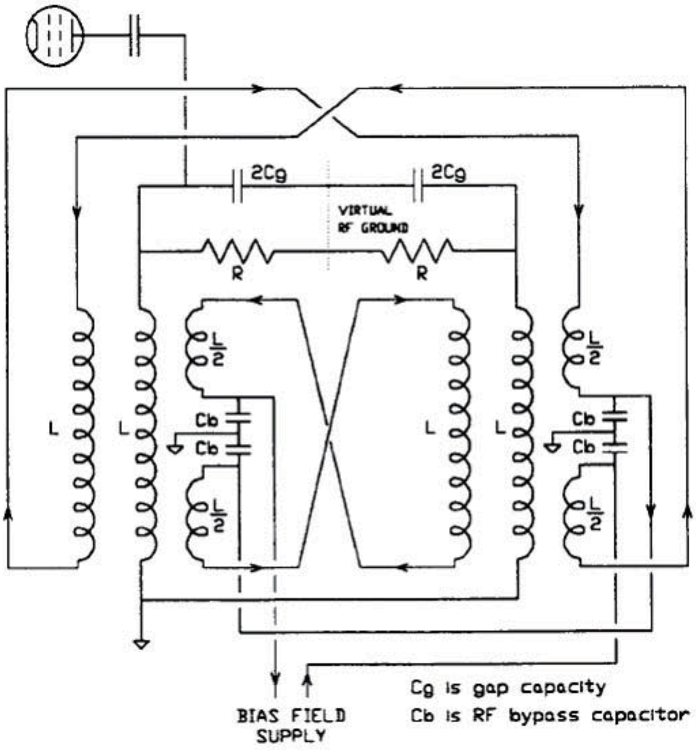

Figure 10.4: An equivalent circuit of a type B cavity[54]

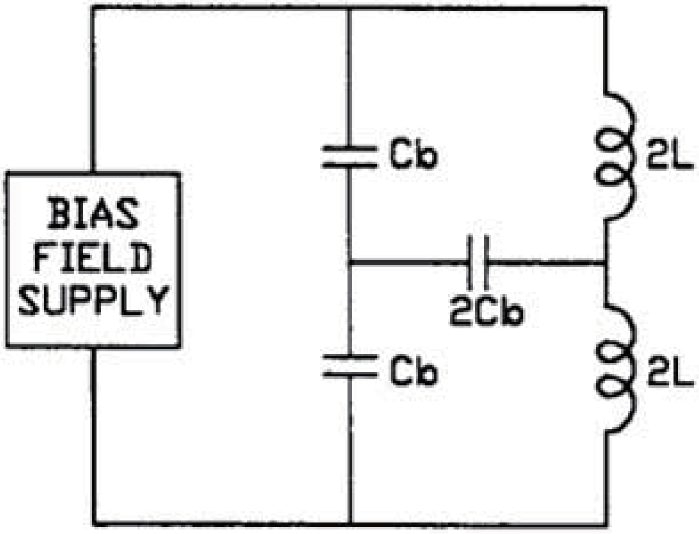

Figure 10.5: A DC circuit to apply a bias field on cores of type B cavity[54]

Type C

This type of coaxial cavity has only one accelerating gap. Wires for inducing bias magnetic field are connected to points where RF voltages are zero, which balances out the RF voltage induced on the wires. And the wires are wound to have a shape of figure of eight in a same way of type B.

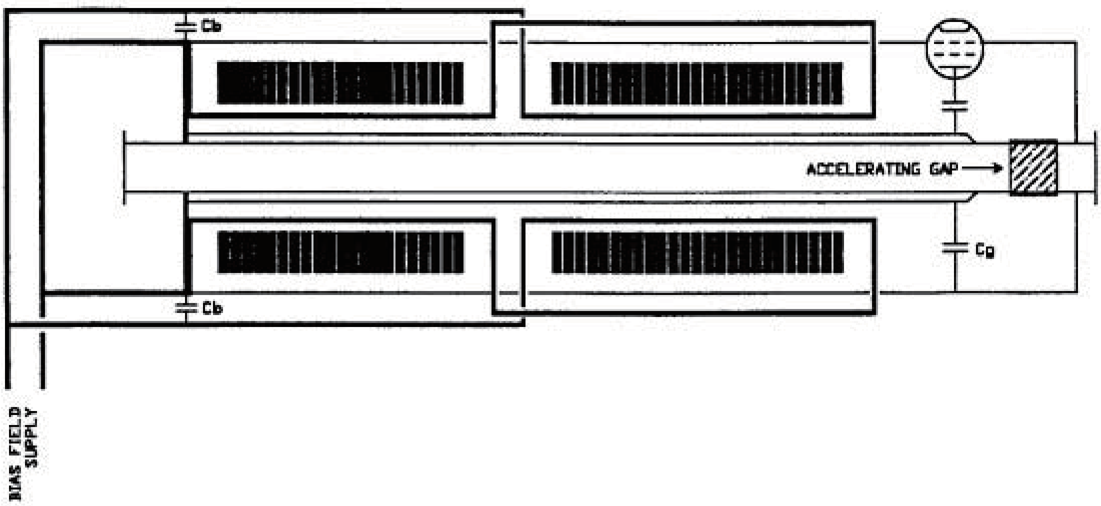

Figure 10.6: A schematic view of a type C cavity[54]

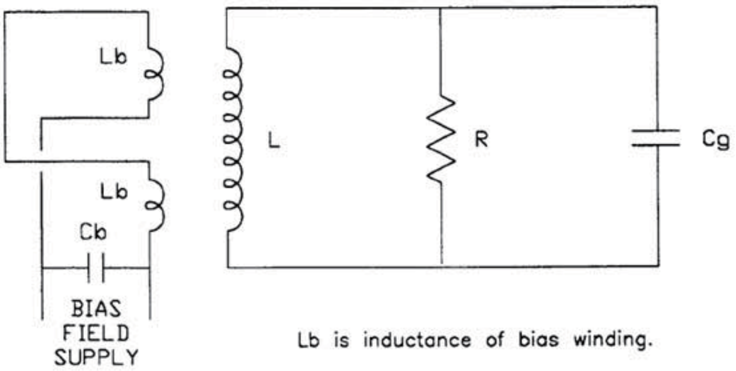

Figure 10.7: An equivalent circuit of a type C cavity[54]

Type D

As shown in Figure **10.8**, a loss of ferrite (hysteresis loss) is small in a high magnetic field. A DC magnetic field is applied on a ferrite core and Q factor of a cavity increases. A control of a permeability of the core is shown in Figure **10.9**. When a bias magnetic field is applied parallel to an RF magnetic field, a slope of the tangent of B-H curve corresponds to the permeability. When the bias magnetic field is applied perpendicular to the RF magnetic field, a slope of the straight line passing through origin and a point on the B-H curve corresponds to the permeability. Considering to tune the permeability of the core, the parallel bias field is better at low magnetization, while perpendicular bias field is better at high magnetization. Therefore, a solenoidal magnetic field is applied perpendicular to the core in the cavity of Type D.

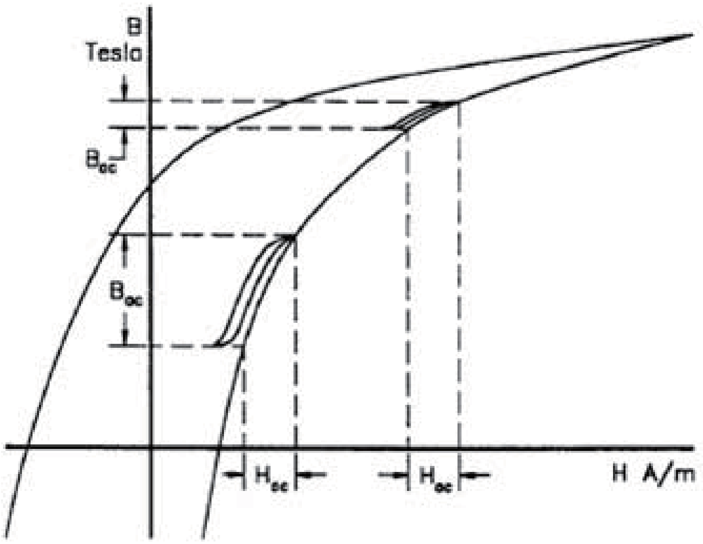

Figure 10.8: A hysteresis loop of a ferrite[54]

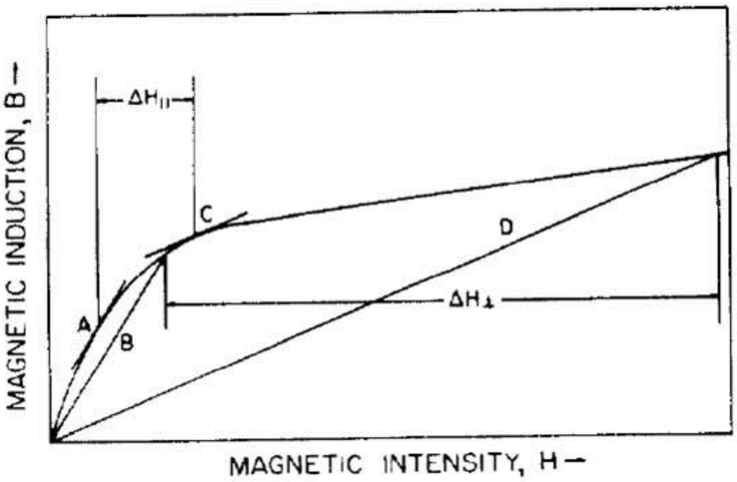

Figure 10.9: A control of a permeability of a ferrite core with a bias magnetic field. In the case that the bias field is applied parallel to an RF field, a slope of a tangent of the B-H curve, such as A and C, corresponds to a permeability. In the case that the bias field is applied perpendicular to the RF field, a tangent of a line which is drawn from the origin to a point on the curve, such as B and D, corresponds to a permeability. In the region of small magnetization, the parallel bias field which is able to vary the permeability strongly is favorable. In the region of large magnetization, the perpendicular field is of advantage, because the slope of the curve almost stays constant[78].

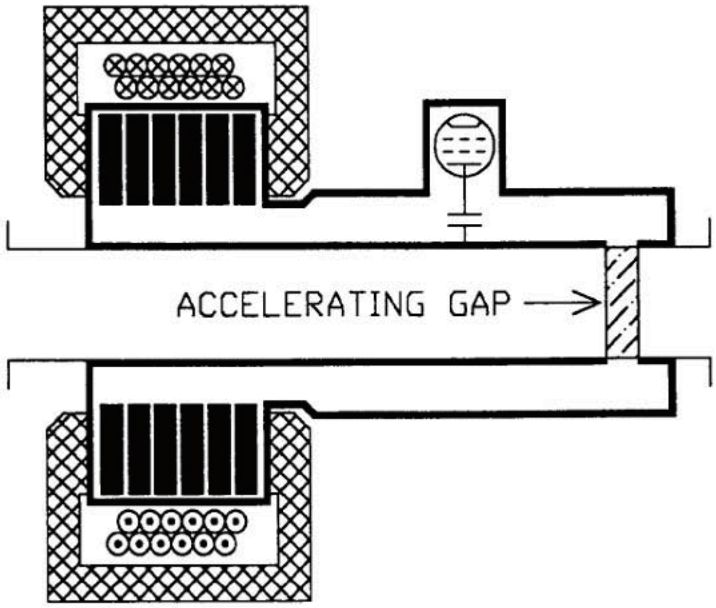

Figure 10.10: A schematic view of a type D cavity[54]

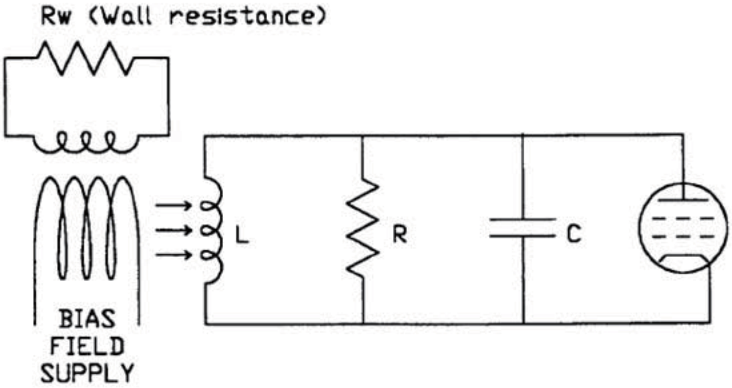

Figure 10.11: An equivalent circuit of a type D cavity[54]

J.1.4 Drift tube type cavity

Cavities loaded with ferrite cores are mounted on a drift tube. Directions of RF voltages in each half coaxial tube are opposite, so that RF voltages are canceled to be zero on the bias wires. Only one ferrite coaxial tube is shown in Figure **10.12**, however, three tubes are mounted in actual configuration. A length of the drift tube is long at low frequency, so that a phase is changed while a beam is passing in the drift tube. Therefore, the usable frequency is over a few tens MHz.

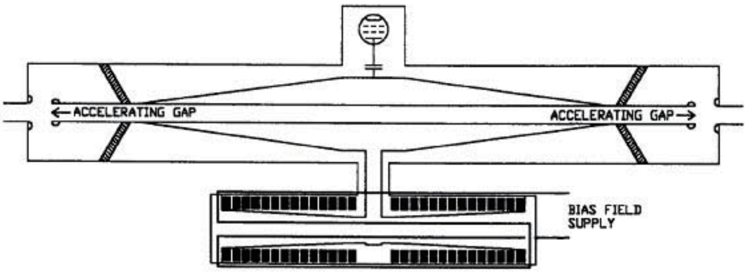

Figure 10.12: A schematic view of a drift tube[54]

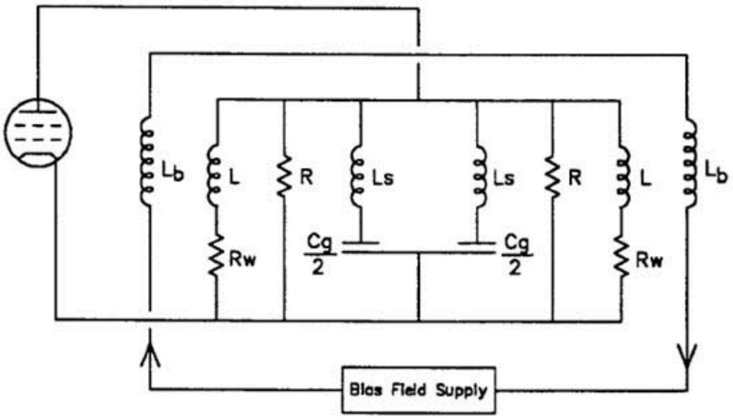

Figure 10.13: An equivalent circuit of a drift tube[54]

J.2 A cavity loaded with magnetic alloy cores

As mentioned above, a bias magnetic field is applied on the ferrite cores in the accelerating cavity and the resonance frequency is tuned. On the contrary, a cavity which is excited by forced oscillation without tuning exists. Magnetic alloys are installed in this type of cavity. The cavity loaded with magnetic alloys has a small Q-factor because of the large loss of eddy current, so that a reflection is small even slightly off resonance. A feedback system for bias field is not needed. Therefore, we are able to simplify the accelerating system.

J.2.1 An RF cavity in National Institute of Radiological Science

National Institute of Radiological Science (NIRS) simplified an accelerator system and reduced costs by introducing untuned accelerating system into the synchrotron named HIMAC. Magnetic cores which has low Q are installed in an accelerating cavity for untuned acceleration in order to be oscillated in wide range of frequency. Adopted cores for HIMAC are Co-based amorphous cores which have Q$\sim$0.5. A cavity loaded with these cores are operated between 0.4 MHz and 8 MHz. An accelerating voltage is 4 kV with an input power of 8 kW. One cavity has two accelerating gaps and each gap has six cores. Sizes of the core and a cross-section of the cavity are shown in Table **10.2** and Figure **10.14**, respectively. Magnetic alloys are conductive, so that large heat appears. Indirect cooling was selected to cool the heat. Cooling plates made of copper are attached on the surfaces of the cores. Current paths appear as shown in Figure **10.15** when cooling plates are attached on both surfaces. Therefore, the plates are attached on only one surface. An epoxy resin which is mixed with alumina in order to increase the tharmal conductivity is used as an adhesive. A semiconductor amplifier is used for excitation. A transformer of 1:9 is connected between the cavity and the amplifier to match their impedance.

Table 10.2: Sizes of the Co-based amorphous core of a cavity in HIMAC[74]

Inner diameter [mm]	Outer diameter [mm]	Thickness [mm]
310	550	30

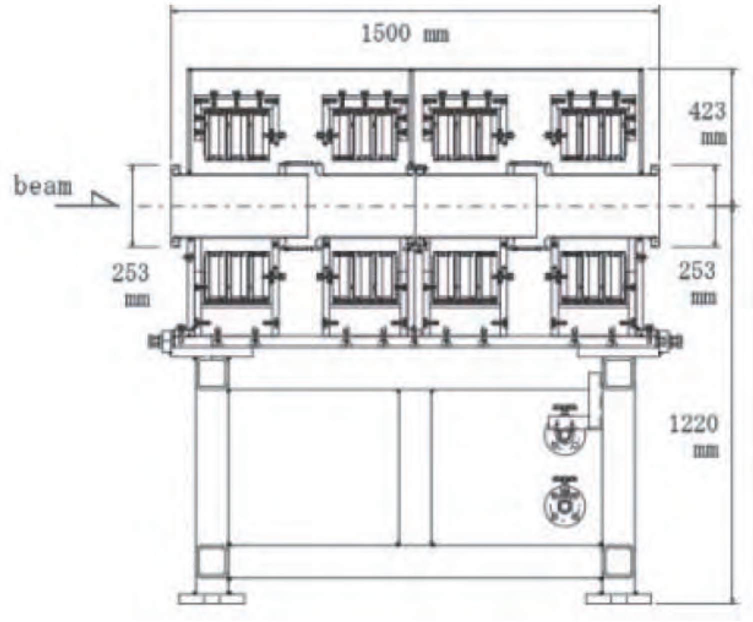

Figure 10.14: A cross-section of the cavity in HIMAC[74]

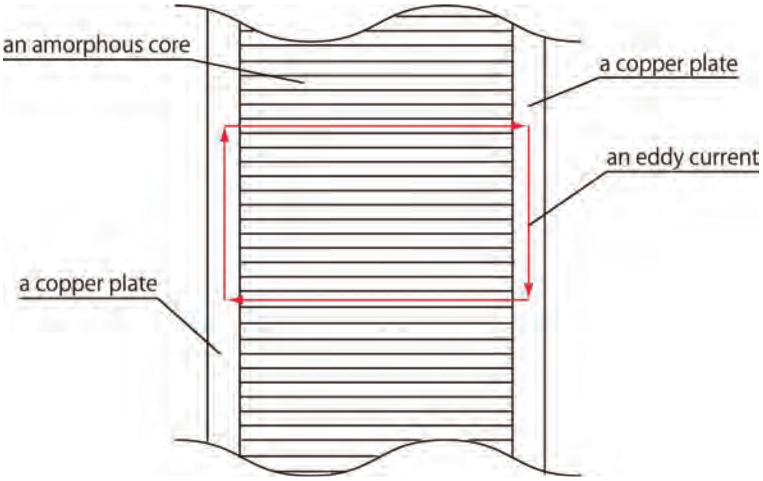

Figure 10.15: A path of an eddy current in the Co-based amorphous core. It emerges when cooling plates made of copper are attached on both surfaces of the core.

J.2.2 An RF cavity in Heidelberg Ion Beam Therapy

A synchrotron for heavy particle radiotherapy was constructed in a hospital of Heidelberg University. The synchrotron accelerates heavy ions, like C^{6+}, up to 430 MeV/u. Two RF cavities of multi feed scheme, which is developed by Hitachi, Ltd., are installed in the synchrotron. A schematic view of the cavity and parameters are shown in Figure **10.16**, Table **10.3**, respectively. Eight FINEMET cores are installed in each cavity. One turn loops for excitation are crossed each core, and input powers are provided by a semiconductor amplifier. Matching boxes are not necessary because an impedance of the core is designed as 50 Ω which is same as that of coaxial cable for power supply. A power combiner of kW order is not needed to be set after the output of the amplifier because powers are superposed in the cavity, so that we can simplify the system.

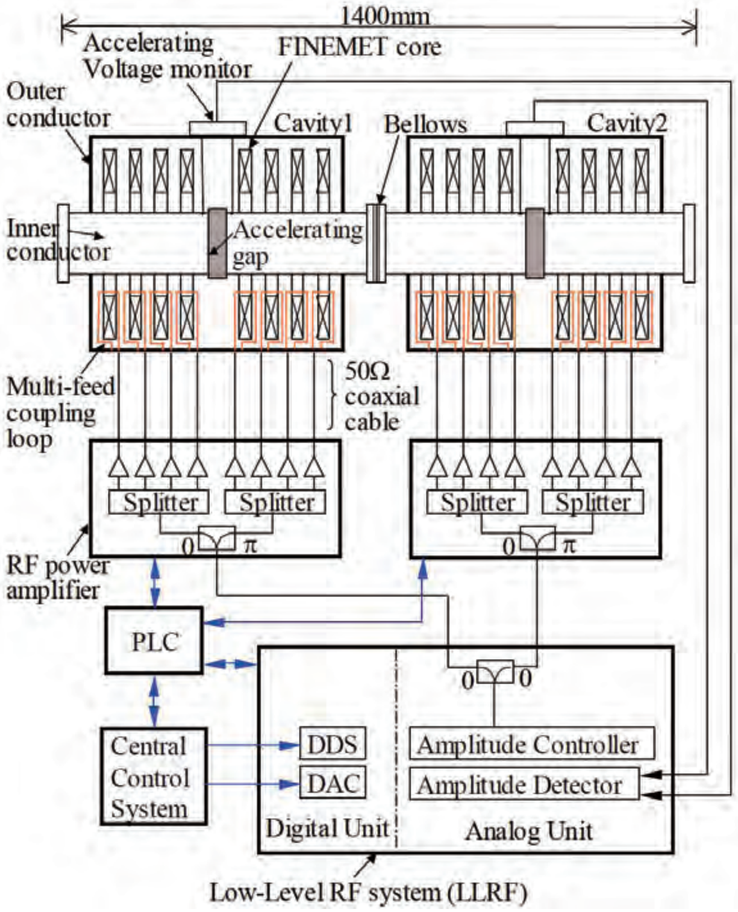

Figure 10.16: A schematic view of an RF cavity in Heidelberg Ion Beam Therapy[75]

Table 10.3: Parameters of an RF cavity in Heidelberg Ion Beam Therapy[75]

Frequency range	1-7[MHz]
Accelerating voltage	2.5[kV$_p$] for a fundamental wave with higher order modes Over 3.3[kV$_p$] without higher order modes
VSWR	below 2
Sizes of the cavity	Outer diameter: 750[mm] Inner diameter: 200[mm]
Material of core	FT-3M
Sizes and number of the cores	Outer diameter: 675[mm] Inner diameter: 300[mm] Thickness: 25[mm] 8 cores
Impedance	100-140[Ω]/core
Dissipated power	7.0[kW] (880[W]/core, 440[W]/ch)
Cooling system	Forced air cooling

Bibliography

[1] T. Kobayashi, *"Current status of T2K"*, the 1st meeting for the beam enhancement of MR, Tokai-mura, Japan (2010)

[2] The web site of J-PARC, http://j-parc.jp/

[3] K. Nishikawa et al., *"Tokai-to-Kamioka (T2K) Long Baseline Neutrino Oscillation Experiment Proposal"*, the 1st PAC meeting, p11 (2006)

[4] T. Nakaya, *"New results and future plan of the long baseline neutrino experiment - from K2K to T2K -"*, COE seminar, Tokyo Institute of Technology

[5] K. Matsuoka, *"Development of Muon Monitor for T2K Long Baseline Neutrino Oscillation Experiment"*, Master's thesis (2007)

[6] A. Vacheret, *"The T2K beam line and near detectors"*, http://www.imperial.ac.uk/research/hep/preprints/07-22.pdf

[7] The web site of GEANT, http://wwwasd.web.cern.ch/wwwasd/geant/index.html

[8] J. Kubota, *"Research and development of a neutrino beam monitor for T2K long baseline neutrino oscillation experiment"*, Master's thesis (2005)

[9] Y. Itow et al., *"The JHF-Kamioka neutrino project"*, arXiv:hep-ex/0106019 (2001)

[10] K. Nishikawa et al., *"Neutrino Oscillation Experiment at JHF"*, Letters of Intent for Nuclear and Particle Physics Experiments at the J-PARC, L12

[11] Y. Mori et al., *"An Experimental Search for the* μ^-*-*e^- *Conversion Process at an Ultimate Sensitivity of the Order of* 10^{-18} *with PRISM"*, Letters of Intent for Nuclear and Particle Physics Experiments at the J-PARC, L25

[12] Y. Yamazaki et al., *"J-PARC Accelerator"*, Kou-Enerugi news Vol.24 No.1 (2005)

[13] H. Harada, *"Injection of minus ion beams"*, OHO'10, KEK, Japan (2010)

[14] H. Oguri et al., *"OPERATION STATUS OF THE J-PARC* H^- *ION SOURCE"*, Proceedings of Particle Accelerator Society Meeting 2009, JAEA, Tokai, Naka-gun, Ibaraki, Japan (2009)

[15] T. Inoue, *"Atom-molecule process and space distribution of minus ions in a discharge of an arc for minus ion source"*, Atom Molecule Data Society Meeting, Koku-Kaikan, Shimbashi (2007)

[16] M. Ikegami, *"Achievement of 181 MeV acceleration at Liniac in J-PARC"*, Kou-Enerugi news Vol.25 No.4 (2007)

[17] M. Ikegami, *"Linear accelerator (II)"*, OHO'01, KEK, Japan (2001)

[18] P. Tom, *"J-PARC RFQ Design"*, Proton Driver Meeting (2005)

[19] N. Tokuda, *"RFQ Linear Accelerator"*, OHO'96, KEK, Japan (1996)

[20] S. Fu et al., *"324-MHz RF DEFLECTOR DESIGN AND TEST"*, International Linac Conference (LINAC98), Chicago, IL, United States (1998)

[21] M. Ikegami, *"Overview of Injection Facility"*, OHO'01, KEK, Japan (2001)

[22] R. Muto, *"Current status of the construction of the devices for the slow extraction from J-PARC 50GeV Main Ring"*, The J-PARC Hadron Hall Users' Association report

[23] S. Sawada, *"Introduction to the slow extraction system at the J-PARC 50-GeV accelerator"*, The J-PARC Hadron Hall Users' Association report

[24] M. Yoshii et al., *"J-PARC RING RF SYSTEMS"*, Proceedings of the 1st Annual Meeting of Particle Accelerator Society of Japan and the 29th Linear Accelerator Meeting in Japan (August 4 - 6, 2004, Funabashi Japan)

[25] M. Yoshii et al., *"The status of J-PARC Ring RF systems"*, Proceedings of the 5th Annual Meeting of Particle Accelerator Society of Japan and the 33rd Linear Accelerator Meeting in Japan (August 6-8, 2008, Higashihiroshima, Japan)

[26] S. Chikazumi, *"Physics of Ferromagnetism, Vol. I - Magnetic Properties of Matter -"*, Shokabo (1978)

[27] C. Ohmori et al., *"UPGRADE SCENARIO OF J-PARC RING"*, Proceedings of the 5th Annual Meeting of Particle Accelerator Society of Japan and the 33rd Linear Accelerator Meeting in Japan (August 6-8, 2008, Higashihiroshima, Japan)

[28] BNL Web site, http://www.bnl.gov/bnlweb/history/AGS_history.asp

[29] G. Rakowski, *"RF ACCELERATING CAVITIES FOR AGS CONVERSION"*, PAC 1967, Washington, D.C., United States (1967)

[30] P.V. Belov et al., *"A SECOND HARMONIC IN FERRITE DOMINATED CAVITY OF U-70"*, EPAC '96, Meliá Gran Sitges Hotel, Sitges, Barcelona, Spain (1996)

[31] J.R. Sanford, *"THE FERMI NATIONAL ACCELERATOR LABORATORY"*, Annu. Rev. Nucl. Sci. 1976.26:151-198.

[32] Hub Pages, http://hubpages.com/hub/CERN-Time-Line-With-Major-Events–History-And-Particle-Physics

[33] U. Bigliani et al., *"THE RF ACCELERATING SYSTEM FOR THE CERN PS BOOSTER"*, PAC 1971, Chicago, IL, United States (1971)

[34] L. Rosen, *"LAMPF-Its Origins, History, and Accomplishments"*, Progress of Theoretical Physics Supplement No.85 (1985)

[35] R.L. Poirier et al., *"PARALLEL BIAS VS PERPENDICULAR BIAS OF A FERRITE TUNED CAVITY FOR THE TRIUMF KAON FACTORY BOOSTER RING"*, EPAC '88, Rome, Italy (1988)

[36] E. Ezura, *"THE HIGH POWER RF SYSTEM FOR THE KEK BOOSTER SYNCHROTRON"*, KEK-77-29, KEK Preprint (1977)

[37] M. Yoshii, *"RF Accelerating Cavity"*, OHO'96, KEK, Japan (1996)

[38] M.E. Middendorf *"THE IPNS RCS RF SYSTEM THIRD CAVITY UPGRADE"*, Proceedings of the 2001 Particle Accelerator Conference, Chicago, United States (2001)

[39] PA. Chamouard *"DESCRIPTION AND COMMISSIONING OF MIMAS, BOOSTER STORAGE RING FOR HEAVY AND POLARIZED IONS"* EPAC '88, Rome, Italy (1988)

[40] C. FOUGERON *"RF SYSTEM FOR "MIMAS""*, PAC 1981, Washington, D.C., United States (1981)

[41] S. Kullander, http://cerncourier.com/cws/article/cern/28223

[42] C. Ekström et al., *"The CELSIUS Project"*, Physica Scripta. Vol.T22, 256-268 (1988)

[43] T. Lofnes, *"RF and Beam control system for Celsius"*, EPAC '90, Nice, France (1990)

[44] R.L. Poirier, *"Perpendicular Biased Ferrite-Tuned Cavities"*, PAC 1993, Washington, D.C., United States (1993)

[45] M. Šumbera, *"High energy nuclear physics and multiparticle dynamics"*, Doctor's thesis

[46] K. Kaspar, *"DEVELOPMENT OF THE FAST FEEDBACK SYSTEM FOR THE GSI SIS CAVITIES"*, EPAC '00, Austria Center, Vienna, Austria (2000)

[47] W.T. Weng, *"OPERATION OF THE BROOKHAVEN AGS WITH THE BOOSTER"*, PAC 1993, Washington, D.C., United States (1993)

[48] R.T. Sanders et al., *"The AGS Booster low frequency RF system"*, PAC 1991, San Francisco, California, United States (1991)

[49] The web page of IKP, http://www.fz-juelich.de/ikp/en/accelerators.shtml

[50] The web page of MI of FNAL, http://www-fmi.fnal.gov/History/history.html

[51] V. Wu et al., *"DESIGN OF A NEW MAIN INJECTOR CAVITY FOR THE FERMILAB PROTON DRIVER ERA"*, Proceedings of 2005 Particle Accelerator Conference, Knoxville, Tennessee (2005)

[52] M. Blaskiewicz et al., *"RF System for the SNS Accumulator Ring"*, Proceedings of the 2001 Particle Accelerator Conference, Chicago (2001)

[53] Y. Mori et al., *"A NEW TYPE OF RF CAVITY FOR HIGH INTENSITY PROTON SYNCHROTRON USING HIGH PERMEABILITY MAGNETIC ALLOY"*, EPAC '98, Stockholm City Conference Centre, Stockholm, Sweden (1998)

[54] I.S.K. Gardner, *"FERRITE DOMINATED CAVITIES"*, CERN accelerator school CERN-92-03-V-2, p.349 (1992)

[55] M. Nomura et al., *"CONDITION OF MA CORES IN THE RF CAVITIES OF J-PARC SYNCHROTRONS AFTER SEVERAL YEARS OF OPERATION"*, Proceedings of IPAC 10, Kyoto, Japan (2010)

[56] H. Yamamura, *"Toroidaru·Koa Katsuyo Hyakka (Encyclopedia for the application of a toroidal core)"*, CQ Publishing Co., Ltd. (2006)

[57] F. Tamura et al., *"Longitudinal painting with large amplitude second harmonic rf voltages in the rapid cycling synchrotron of the Japan Proton Accelerator Research Complex"*, PHYSICAL REVIEW SPECIAL TOPICS - ACCELERATORS AND BEAMS 12, 041001 (2009)

[58] T. Takahashi, *"Study of an Accelerating Cavity Loaded with Magnetic Alloy Cores for Stabilizing the High Intensity Beam in J-PARC"*, Master's thesis

[59] T. Suehiro, *"Fundamental Study of a New Cooling System for the Accelerating Cavity for Enhancing Main Ring in J-PARC"*, Master's thesis

[60] G. Ben eds., *"Plastic Ki Fukugo Zairyo wo Shiru Jiten (A dictionary for plastic based composite materials)"*, Agune (1986)

[61] H. Ino et al., *"Research on radiation resistant rubber O-ring for accelerators"*, Proceedings of the 10th Ultra High Vacuum Technology for Accelerator Science and Storage Ring, KEK, Japan (2004)

[62] The web page on thermophysical properties section at NMIJ in AIST, http://www.nmij.jp/ mprop-stats/thermophys/homepage/index_j.htm

[63] H.S. Carslaw and J.C. Jaeger, *"Conduction of Heat in Solids"*, Oxford University Press, New York, 2nd ed., p.76 (1959)

[64] W.J. Parker et al., *"Flash Method of Determining Thermal Diffusivity, Heat Capacity, and Thermal Conductivity"*, J. Appl. Phys. **32**, 1679 (1961)

[65] M. Yoshii, *"RF acceleration 1"*, OHO'09, KEK, Japan (2009)

[66] Private communication with Sumitomo 3M, Inc.

[67] T. Kageyama et al., *"Alternative Solutions for the Ring RF Cavity Structures"*, ATAC'09, JAEA Tokai, Japan (2009)

[68] High-intensity Proton Accelerator Project Team, *"ACCELERATOR TECHNICAL DESIGN REPORT FOR HIGH-INTENSITY PROTON ACCELERATOR FACILITY PROJECT, J-PARC"* (2003)

[69] Hitachi Metals, *"Nanocrystalline soft magnetic material, FINEMET"*, http://www.hitachi-metals.co.jp/prod/prod02/pdf/hl-fm9-e.pdf

[70] The Japan Society of Mechanical Engineers, *"JSME Mechanical Engineers' Handbook"*, Maruzen Co., Ltd. (1987)

[71] *"ANSYS CFX-Solver Theory Guide -ANSYS CFX Release 11.0-"*, p.112 (2006)

[72] K. Ota, *"Jiki Kogaku no Kiso II -Jiki no Oyo- (Foundation of Magnetic Engineering II -Application of Magnetism-)"*, p.391, Kyoritsu Shuppan Co., Ltd. (1973)

[73] H. Nakayama, *"Summary of the measurement of magnetic materials for JHF RF cavity (2) -FINEMET-"*, KEK Report 98-13 (1999)

[74] M. Kanazawa et al., *"RF CAVITY WITH CO-BASED AMORPHOUS CORE"*, Proceedings of EPAC 2006, Edinburgh, Scotland (2006)

[75] T. Hae et al., *"DEVELOPMENT OF RF ACCELERATING SYSTEM FOR ION THERAPY SYNCHROTRON"*, Proceedings of the 2nd Annual Meeting of Particle Accelerator Society of Japan and the 30th Linear Accelerator Meeting in Japan, Tosu, Japan (2005)

[76] K. Saito et al., *"FINEMET-core loaded untuned RF cavity"*

[77] A. Schnase, *"CAVITIES WITH A SWING"*, CERN accelerator school CERN-2005-003, p.236 (2005)

[78] W.R. Smythe, *"Reducing Ferrite Tuner Power Loss by Bias Field Rotation"*, IEEE Transactions on Nuclear Science, Vol. NS-30, No. 4 (1983)